2003-10-07

Joule heat effects on reliability of RF MEMS switches

Malgorzata S. Machate
Worcester Polytechnic Institute

Joule heat effects on reliability of RF MEMS switches

A Thesis
Submitted to the faculty
of the

Worcester Polytechnic Institute

in partial fulfillment of the requirements for the
Degree of Master of Science
in
Mechanical Engineering

by

Malgorzata S. Machate

29 May 2003

Approved:

Prof. Ryszard J. Pryputniewicz, Major Advisor

Prof. Cosme Furlong, Member, Thesis Committee

Prof. Raymond R. Hagglund, Member, Thesis Committee

Mr. David A. Rosato, President, Harvard Thermal, Inc.
Member, Thesis Committee

Prof. Gretar Tryggvason, Member, Thesis Committee

Prof. John M. Sullivan, Jr., Graduate Committee Representative

by

NEST – NanoEngineering, Science, and Technology
CHSLT- Center for Holographic Studies and Laser micro-mechaTronics
Mechanical Engineering Department
Worcester Polytechnic Institute
Worcester, MA 01609-2280

SUMMARY

Microelectromechanical system (MEMS) technology has been evolving for about two decades. It has been integrated in many existing designs, including radio frequency (RF) microswitches. Since as early as 1971, when the first RF switches were built using commercial technologies, the designs have developed and improved dramatically. The newest switches that are manufactured and tested today, using MEMS technology, operate at radio, even microwave frequencies. Designers are approaching the optimal MEMS switch, yet electro-thermo-mechanical (ETM) effects still limit the design possibilities and adversely affect reliability of the microswitches. An optimal RF MEMS switch is one with low insertion loss, high isolation, short switching time, and operational life of millions of cycles. The ETM effects are a result of Joule heat generated at the microswitch contact areas. This heat is due to the current passing through the microswitch, characteristics of the contact interfaces, and other parameters characterizing a particular design. It significantly raises temperature of the microswitch, thus affecting the mechanical and electrical properties of the contacts, which may lead to welding, causing a major reliability issue. In this thesis, a study of ETM effects was performed to minimize the Joule heat effects on the contact areas, thus improving performance of the microswitch. By optimizing mechanical, thermal, and electrical characteristics of the microswitch, its resistance can be minimized assuring lower operational temperatures. Thermal analyses done computationally, using Thermal Analysis System (TAS) software, on a cantilever-type RF MEMS switch indicate heat-affected zones and the influence that various design parameters have on these zones. Uncertainty analyses were also

performed to determine how good the results are. Based on the results obtained, for the cases of the baseline design of the microswitch, considered in this thesis, contact temperatures on the order of 700ºC were obtained. Although these temperatures are well below the melting temperatures of the materials used, new designs of the microswitches will have to be developed, in order to lower their maximum operating temperatures and reduce temporal effects they cause, to increase reliability of the RF MEMS switches. Results obtained in this thesis also showed that a microswitch with contact resistance equal to 50% of that in the baseline design achieves maximum temperatures of 409ºC leading to a higher operational reliability than that of the baseline design of the microswitch.

ACKNOWLEDGEMENTS

This thesis was completed thanks to help of Prof. Ryszard J. Pryputniewicz. His inspiration, advice, and support were endless. Special thanks also go to Prof. Cosme Furlong and Prof. Joseph J. Rencis, the faculty of Mechanical Engineering Department, for their assistance in completing this thesis; James R. Reid and Lavern A. Starman for being a sea of RF MEMS knowledge; and David A. Rosato of Harvard Thermal for his never ending aid with TAS modeling.

TABLE OF CONTENTS

LIST OF FIGURES

LIST OF TABLES

NOMENCLATURE

a	average contact asperity radius
b	width of cantilever
b_e	width of electrode
b_s	width of shorting bar
b_t	width of trace
c_p	specific heat
d	distance, damping coefficient
d_c	average center to center distance between asperities
d_e	distance between electrodes
d_g	contact gap
d_o	height of the cantilever post
f_o	fundamental natural frequency
g	gravitational acceleration
h	cantilever thickness, convective heat transfer coefficient
h_c	contact coefficient
h_s	shorting bar thickness
h_t	trace thickness
$i_{1,2}$	current in the circuit
j	$\sqrt{-1}$
k	constant, spring constant, thermal conductivity
k_A	thermal conductivity of material A
k_B	thermal conductivity of material B
m	dynamic mass
n	number of asperities per unit area
p_m	maximum contact pressure
w	geometric constant
x	distance
x_1	axial position along section-1 of the cantilever
x_2	axial position along section-2 of the cantilever
A	area
A_A	cross-sectional area of material A
A_B	cross-sectional area of material B
A_c	contact area, area through which heat convection occurs
A_k	area through which heat conduction occurs
A_r	radiation area
B	bias limit
C	electrical capacitance, integration constant
D	depth, diameter
E	modulus of elasticity
F	force
F_{ES}	electrostatic force

F_k spring force
F_n normal force
F_s geometric view factor, sliding force
F_S slip force
Gr Grashof number
H material hardness
I current, second moment of area
$\boldsymbol{K}$ vector
L length, electrical inductance
$\boldsymbol{L}$ vector
L_1 length of section-1 of the cantilever
L_2 length of section-2 of the cantilever
L_c length of contact
L_e length of electrodes
L_o horizontal distance from the cantilever post to the electrode
L_r Lorenz number
L_s length of shorting bar
L_t length of traces
L_{to} discontinuity in trace under shorting bar
M bending moment
N isoparametric element
N_i shape function
Nu Nusselt number
P_j Legendre polynomial
P_X precision limit
Pr Prandtl number
Q electric charge
Q_c heat transfer due to convection
Q_i electric charge
Q_J Joule heat
Q_k heat transfer due to conduction
Q_r heat transfer due to radiation
R radius, electrical resistance
R_A reaction force
R_c thermal resistance due to convection, thermal contact resistance
R_C electrical contact resistance
R_E electrical resistance of a conductor
R_k thermal resistance due to conduction
R_r thermal resistance due to radiation
S_X precision index
T temperature
T_1 beginning temperature, temperature of node 1
T_2 end temperature, temperature of node 2
T_e temperature of enclosure

T_s	temperature of surface
T_∞	ambient temperature
U_X	uncertainty value
V	voltage, volume
$V_{1,2}$	voltage present in a circuit
V_G	voltage supplied to the RF circuit
V_Z	voltage in the RF circuit
X	single value parameter
$\overline{X}$	mean value of a variable
Y	yield coefficient
Z	electrical impedance
Z_o	electrical impedance of the circuit
Z_{open}	electrical impedance of open microswitch
Z_{closed}	electrical impedance of closed microswitch

α	Holm radius
α_T	coefficient of thermal expansion
β	volume coefficient of expansion
δ_X	RSS uncertainty
ε_o	dielectric constant of air
ε_r	relative permittivity
ε_s	emissivity of surface
μ	friction coefficient
μ_o	permeability of free space
ν	kinematic viscosity
ρ	material density
ρ_e	electrical resistivity
$\rho c_p V$	thermal capacitance
σ	Stefan-Boltzmann constant, standard deviation
σ_y	yield strength
ω	electrical current frequency
ξ	local position along the element studied
ζ	asperity deformation
ζ_c	critical asperity deformation

Δ	distance between nodes
Δt	time increment
ΔT	temperature change
Ω	fringe-locus function

OBJECTIVES

The objectives of this thesis were to study Joule heat effects on operation of RF MEMS switches, in order to identify factors which may increase their overall operational reliability, using analytical, computational, and experimental solutions (ACES) methodology.

1. INTRODUCTION

Microelectromechanical systems (MEMS) have been developing with time, following the trends in technology and assimilating to the market demands. Petersen (1979) was a pioneer of frequency switches, although his switch was not a part of what we now refer to as MEMS. His research for IBM Corporation was a foundation for work of researchers like Yao and Chang (1995), or Brown (1998), who brought down the size of the original switch to microscale. As the technology evolved, so did the MEMS designs. The first Petersen cantilever-type switch working at low frequencies has now advanced to tunable microswitches working at radio, even microwave frequencies (Li, et al., 1999; Zou, et al., 2000).

MEMS devices are currently used in telecommunications, wireless networking, global positioning systems, cellular, auto, and even toy industry (De Los Santos and Richards, 2001). Microcomponents greatly reduce size and weight of many products, while reducing their cost and improving performance (Pryputniewicz and Furlong, 2002). Although, at this time, MEMS bring large number of advantages to a range of industries much can still be done to improve their reliability.

Microswitches are an important part of all MEMS devices. These microswitches fit two major design groups: capacitive and resistive (Pryputniewicz, et al., 2002a, 2002b). The capacitive design of a microswitch refers to membrane type microswitches that use difference in capacitance between two electrodes as means of actuation. Resistive, or contact, cantilever type microswitches use electrostatic force as means of actuating the switch and consequently making a metal-to-metal contact.

Contact MEMS switches present a major reliability concern. The Joule heat generated when the current is passed through the microswitch causes its temperature to reach hundreds of degrees Celsius which, in turn, makes the contacts to wear at an increased rate or, at the extreme, weld. Changing certain design parameters, e.g., materials, dimensions, and/or surface finish of contacts, can enhance the life of the microswitch. Modifying the integrated circuits (ICs) featuring the microswitches has been proven as a successful technique for decreasing the current passing through the microswitch, thus may be used as another promising method of improving the microswitch reliability (Tyco 2000a).

1.1. Microswitch classification

The radio frequency (RF) MEMS switches can be categorized based on the contact type, actuation method, and configuration. The two types of contacts present in RF MEMS switch designs are the metal to metal contacts and metal-insulator-metal contacts. The metal to metal contacts, also referred to as ohmic or direct contacts, can be found in cantilever-type MEMS switches. The signal in this microswitch is propagated when the two metal contacts come together and electrical current passes through the established interface, Fig. 1.1. A sample cantilever-type microswitch manufactured by Cronos (2002) is shown in Fig. 1.2.

The metal-insulator-metal contacts, sometimes referred to as capacitive or indirect contacts, are found in membrane microswitches. The capacitance built up between the

metal on a membrane and metal on the substrate, via applied voltage, is used as means of actuating the microswitch, Fig. 1.3. Figure 1.4 illustrates a sample capacitive microswitch manufactured by Cronos (2002).

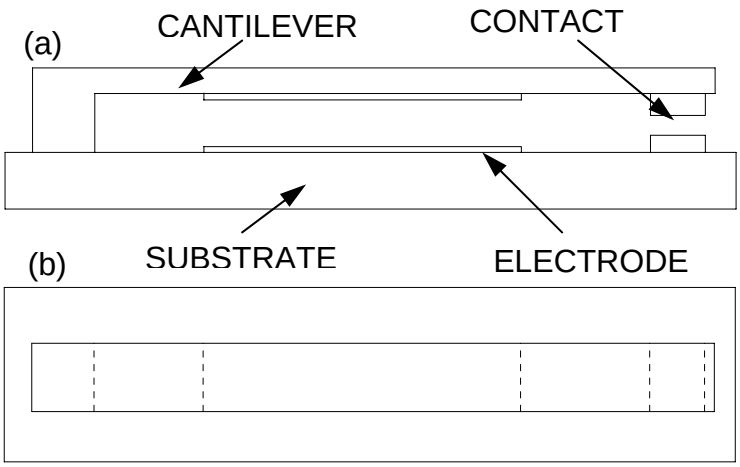

Fig. 1.1. A direct contact RF microswitch: (a) longitudinal cross section, (b) top view.

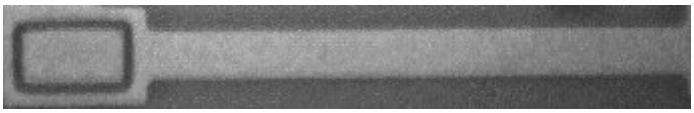

Fig. 1.2. Top view of a sample contact RF microswitch.

The RF MEMS switches also vary according to their actuation method. The three most frequently used actuation methods for RF microswitches are based on electrostatic, magnetic, and thermal techniques. The electrostatic actuation is based on the Coulomb's law, which states that two bodies of opposite charge separated by a known distance attract each other, Fig. 1.5, with a force, *F*, that can be expressed as

$$F = k\frac{Q_1 Q_2}{x^2} \quad , \tag{1.1}$$

where k is a constant, Q_1 and Q_2 are electric charges, and x is the distance separating the charges.

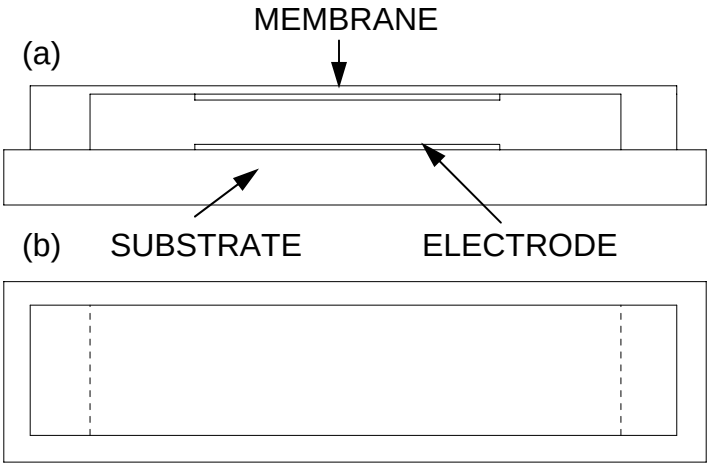

Fig. 1.3. A capacitive RF microswitch: (a) longitudinal cross section, (b) top view.

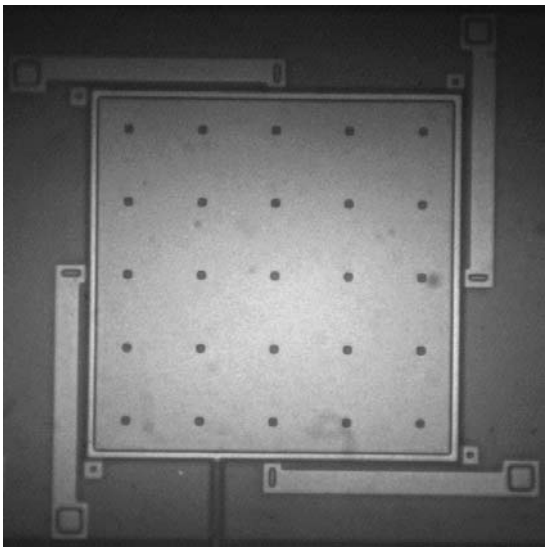

Fig. 1.4. Sample capacitive RF microswitch.

In RF MEMS switch designs, however, the two rigid bodies are really two parallel "metal" plates. The fundamental equation then changes to (Pryputniewicz, 2002)

$$F = -\frac{\varepsilon_o \varepsilon_r A V^2}{2d^2} \quad , \tag{1.2}$$

where ε_o is the dielectric constant of air, ε_r is the relative permittivity of the material between the plates, A is the overlap area between the plates, V is the voltage difference between the plates, and d is the distance between the parallel plates.

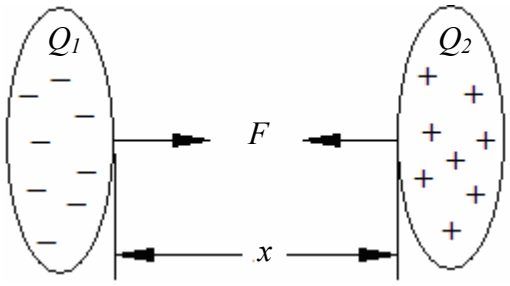

Fig. 1.5. Graphical representation of the Coulomb's law.

Second method of RF MEMS switch actuation is via magnetic field. The Lorentz force law is used in deriving an equation that expresses magnetically induced force between two parallel wires, Fig. 1.6, i. e.,

$$F = -\frac{\mu_o I_1 I_2 L}{2\pi d} \quad , \tag{1.3}$$

where μ_o is the permeability of the free space, I_1 and I_2 are currents in carriers 1 and 2, respectively, L is the overlapping length of the current carriers, and d is the distance separating the current carriers. As apparent from Eq. 1.3, the force induced by a

magnetic field due to the current flow is independent of the cross section of the current carriers.

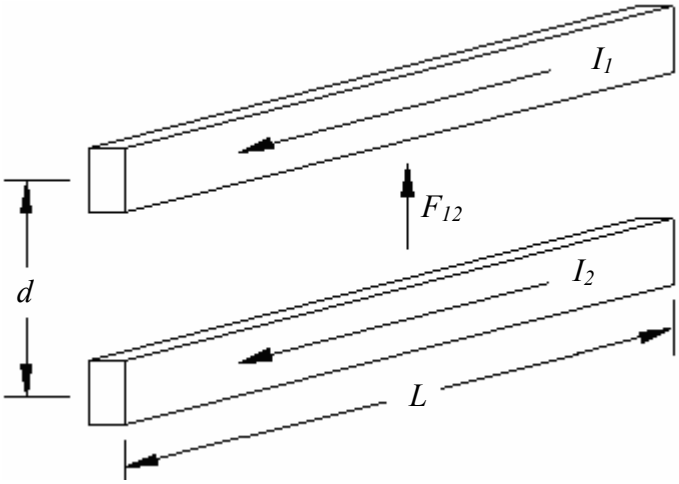

Fig. 1.6. Magnetically induced force between two parallel wires.

Finally, the third actuation method used in the RF MEMS designs is thermal actuation. This actuation takes advantage of the behavior of solids as they undergo temperature changes, Fig. 1.7. Change in a linear dimension due to thermal expansion of any solid can be written as (Pryputniewicz, 2001)

$$\delta L = L\alpha_T \Delta T \quad , \tag{1.4}$$

where L is the original length of the component, α_T is a material specific coefficient of thermal expansion, and ΔT is the change in temperature the solid is experiencing. These linear changes in length actuate the microswitch.

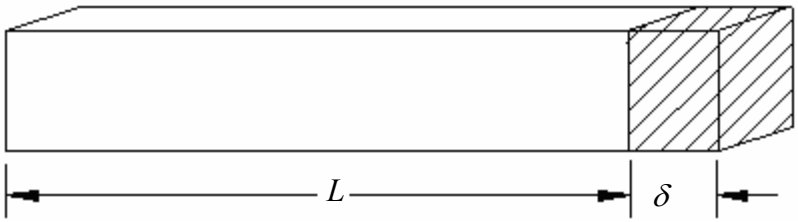

Fig. 1.7. Linear thermal expansion of a solid.

The RF MEMS switches can also be categorized according to the configuration of the circuit they are in (Reid and Starman, 2003). The configuration depends on the microswitch design. The simplest is the series configuration, Fig. 1.8, where the electrical signal enters the microswitch, passes through it, and leaves the microswitch continuing on through the rest of the circuit.

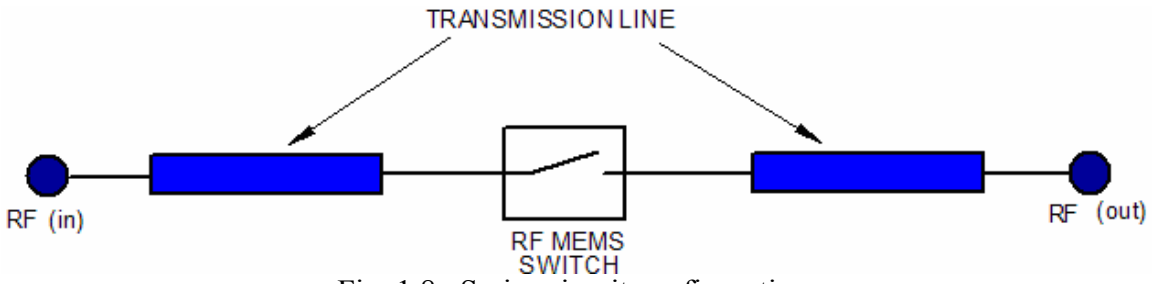

Fig. 1.8. Series circuit configuration.

Also popular is the shunt configuration, Fig. 1.9, in which the microswitch is connected to both, the transmission line and the ground. In this configuration the microswitch is used as a drain for the signal in the transmission line.

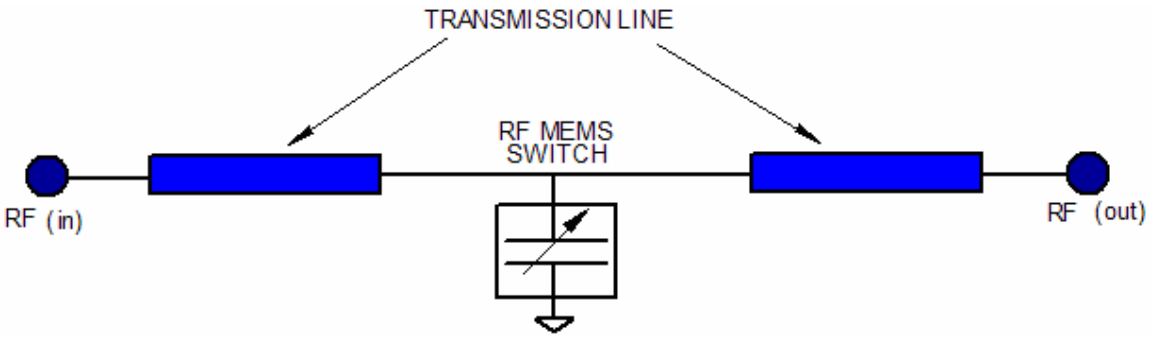

Fig. 1.9. Shunt circuit configuration.

Also known is single pole *n*, or multiple, throw configuration. Figure 1.10 shows a sample single pole three throw configuration. In this configuration the microswitch is used to always complete a circuit. The signal propagation, however, occurs when only one specific circuit is closed.

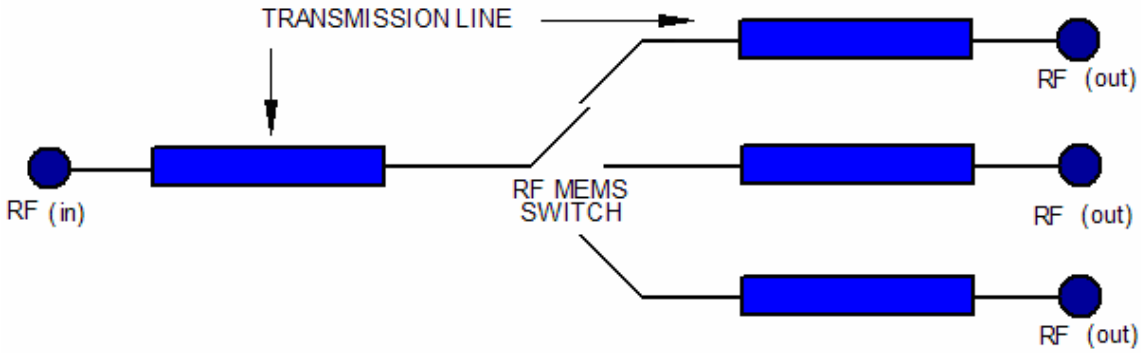

Fig. 1.10. Single pole three throw circuit configuration.

1.2. Manufacturing process

The RF microswitches are manufactured using the techniques available in MEMS fabrication (Pryputniewicz and Furlong, 2002). Because of the scale of manufactured

devises only limited number of methods is used. These methods include bulk micromachining, surface micromachining, LIGA, microforming, and laser machining (Pryputniewicz and Furlong, 2002).

The simplest and very commonly used fabrication technique is bulk micromachining (BMM). It was developed in 1960s and even now remains the least expensive, yet the most ordinary of all manufacturing techniques. The technique usually uses anisotropic etching with KOH that can easily form V shaped grooves, or cut pits with tapered walls of a substrate, Fig. 1.11. The KOH etching can also be used to produce plateau structures, however to achieve that a photoresist mask has to be used. Silicon is most commonly used as substrate in this fabrication method. BMM produces MEMS devices with one functional (i.e., moveable and deformable) structural layer.

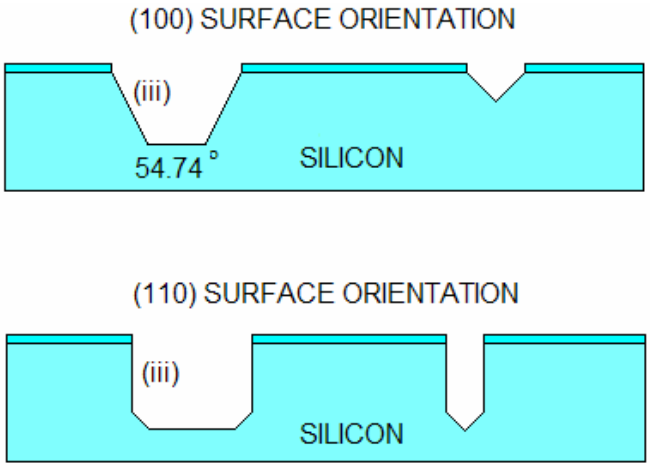

Fig. 1.11. Anisotropic wet etching of bulk micromachining.

The second most commonly used technique in MEMS fabrication is surface micromachining (SMM). The SMM typically employs films of two different materials, a

structural material (e.g., polysilicon) and a sacrificial material (e.g., silicon dioxide, commonly referred to as oxide), Table 1.1. The layers are deposited, patterned, and removed by wet etching to release the structure (Pryputniewicz, 2002). An example of surface micromachining is presented in Fig. 1.12. The SMM holds a key advantage over the BMM in that the SMM components can be one or two orders of magnitude smaller than their BMM counterparts. Currently, the most advanced surface micromachining that is successfully used involves five structural layers and was developed at Sandia National Laboratories. This fabrication is known as Sandia's Ultraplanar MEMS Multi-level Technology (SUMMiT™V) (Pryputniewicz, 2002). This SUMMiT™V process is capable of producing gears, hinges, and combdrives.

Table 1.1. Common surface micromachining materials.

Structural layers	Sacrificial layers
Polysilicon	SiO_2
Al	Polysilicon
Al / Au	Polyimide / PMGI
Au / Ni	Copper
Si_3N_4 / Al / SiO_2	Polysilicon

Another fabrication method for MEMS devices is LIGA. The acronym LIGA comes from the German name for the process (Lithographie, Galvanoformung, Abformung). LIGA uses lithography, electroplating, and molding processes to produce millimeter sized devices, Fig. 1.13. In this technique X-ray lithography is used to

produce molds that serve as forms for high-aspect ratio electroplated 3D structures. Even though LIGA is a popular process for fabrication of MEMS with large features, it still remains the most expensive of them all. LIGA process is rather limited in its implementation because it requires very intense X-ray source provided only by synchrotrons; there are only a handful of synchrotrons available worldwide (Pryputniewicz and Furlong, 2002).

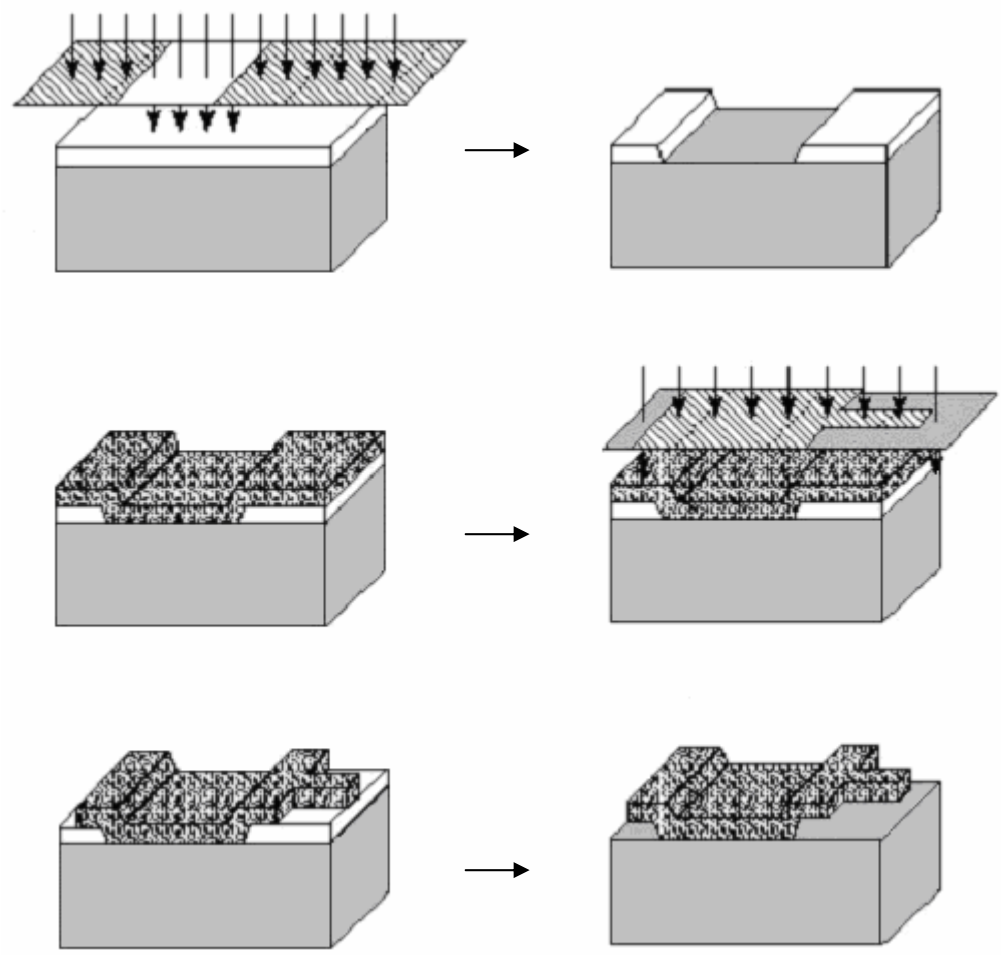

Fig. 1.12. Surface micromachining process overview.

Also, MEMS devices with relatively large aspect ratios can be manufactured by microforming. It is an extension of surface micromachining, however, unlike micromachining it produces a high aspect ratio structures. Microforming uses electroplating to form metal structures and the Multi-User MEMS Process (MUMPS) for metals (Koester, el at., 2001).

In the University of Colorado project, laser machining was used to manufacture a moveable microswitch membrane (Wang, et al., 2001). In this project the AVIA laser with a wavelength of 355 nm and an excimer laser with a wavelength of 248 nm were used to cut slots in Krypton-E copper cladding film. This laser technique, however, causes thermal damages, unless appropriate materials and laser wavelengths are chosen.

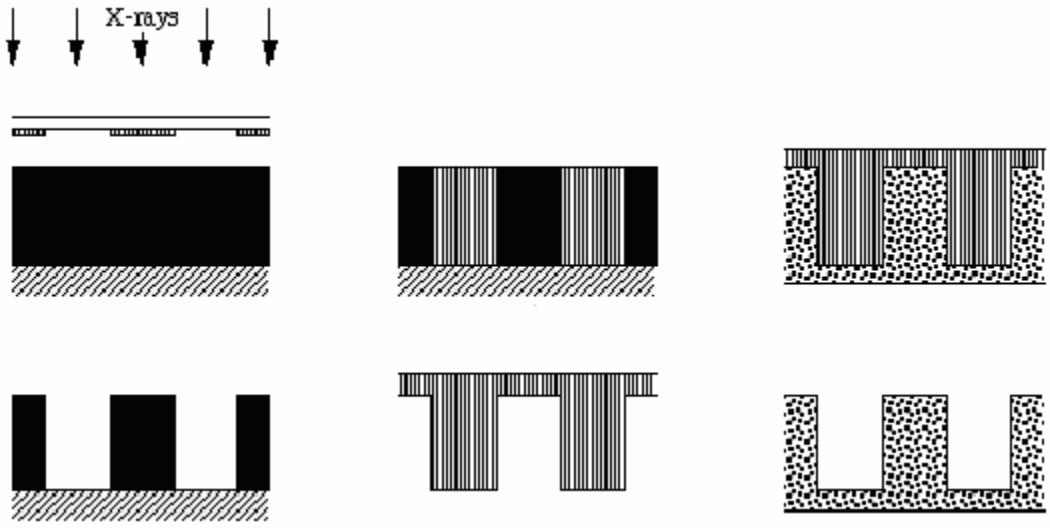

Fig. 1.13. LIGA process overview.

1.3. Manufacturing challenges

Surface micromachining is the most commonly used manufacturing process in RF MEMS fabrication. The latest advancement in the field of surface micromachining led to a development of SUMMiT^{TM}V technology (Pryputniewicz and Furlong, 2002). This five structural layers process was developed by Sandia National Laboratories in New Mexico.

The final stage of the surface micromachining process is releasing the device, which requires removal of the sacrificial layers. Usually this involves a liquid releasing agent. As the liquid evaporates from under the suspended structures attractive forces due to surface tension of liquids cause the suspended structure to collapse onto the structural layer below. Both layers are then held together by atomic bonds. This phenomenon is referred to as stiction. Use of a supercritical point dryer minimizes the effects of stiction. The dryer uses thermodynamic properties of liquid carbon dioxide to prevent liquid evaporation, Fig. 1.14.

The stress gradients in micromachined components present another manufacturing challenge. As the structural material is deposited onto the substrate, crystal lattice impurities may be inadvertently formed, Fig. 1.15. The interstitials present in a crystal lattice induce high compressive stresses while vacancies absorb these stresses. Deposition of two or more dissimilar materials may cause curling of the structures as they are released. The differences in thermal expansion coefficients of materials cause stress gradients, affecting the shape of the final product. Deposition of materials with similar thermal expansion coefficients, but of various thicknesses, causes curling as well.

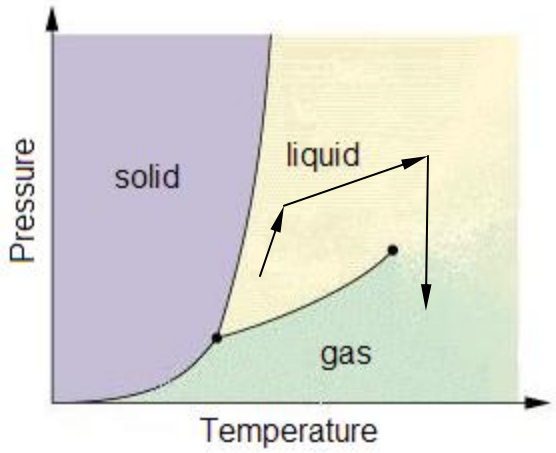

Fig. 1.14. Phase diagram for supercritical drying.

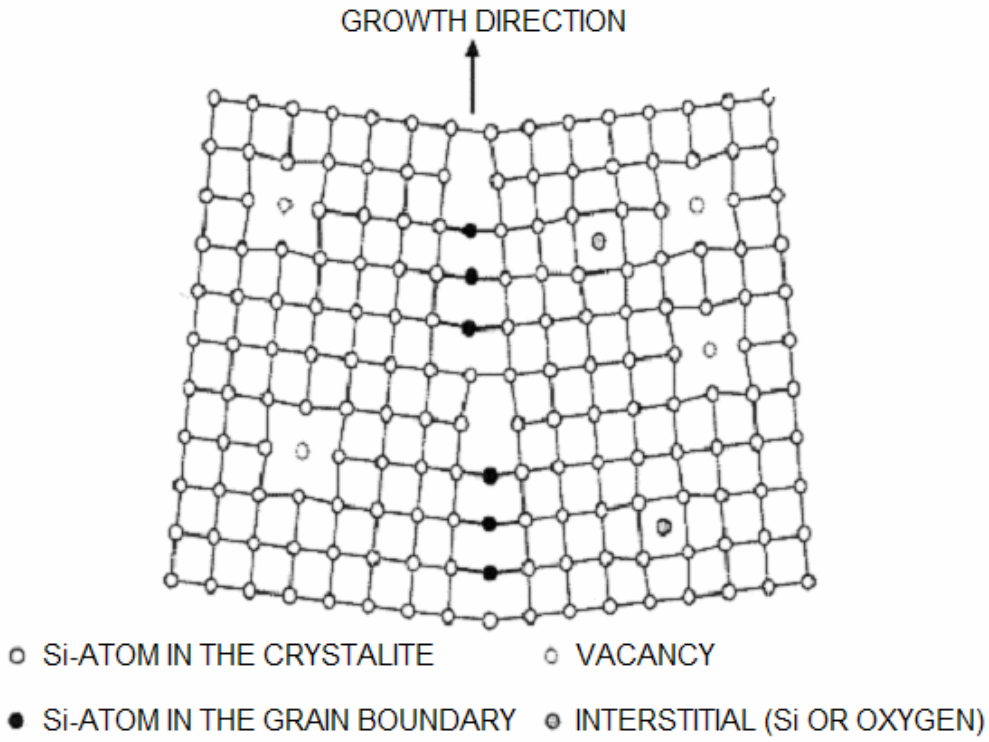

Fig. 1.15. Crystal lattice impurities.

1.4. Contact characteristics

In order to improve the microswitch reliability, certain design parameters may have to be changed or varied. The most important of those parameters is the actual interface contact area of the microswitch, contact materials, and the interface resistance between the contacts.

1.4.1. Contact interface

According to Tyco (2000b) and Mroczkowski (1998) when two switch contacts are overlapped, or in contact, only a portion of their area is truly allowing electric current flow. On a microscale, the surface of the contact material, which conducts electricity across the interface, is not perfectly flat, but has many peaks and valleys, as shown in Fig. 1.16. For this reason, the electric current flows across the switch contact interface only where the high points, or asperities, meet. The actual contact area may be substantially smaller in comparison with the apparent contact area of the microswitch which was intended by the designer.

The actual contact area, however, depends not only on the surface roughness of the two contacting surfaces, but also on the contact force which is normal to the interface. If this normal force is large enough, it can cause plastic deformations of the asperities, thus increasing the actual contact area. The relationship between the actual contact area and the contact force can be expressed as (Mroczkowski, 1998)

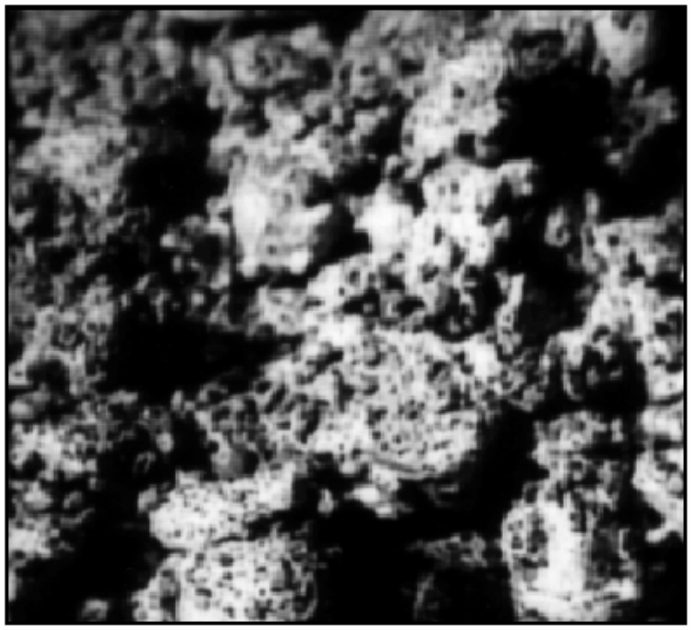

Fig. 1.16. Representative magnified contact surface.

$$A_c = k\frac{F_n}{H} \quad , \tag{1.5}$$

where A_c is the actual contact area, H is the hardness of contact material, F_n is the normal force, and k is the proportionality constant. This constant depends on a number of parameters including the effects of film, lubrication, surface roughness, contact force, and the mode of deformation, among others.

Finally as the two contacts come together, only the highest peaks are subject to a full current load. This causes a sudden raise in temperature and a "melt down" of those peaks increasing the actual contact interface. This melting of the contact metal causes superheating of the surrounding air and its ionization. With high enough voltage an arc may generate. The melting of the contact material may also cause material transfer

between contacts, Fig. 1.17, which in return may cause permanent damage of the contacts.

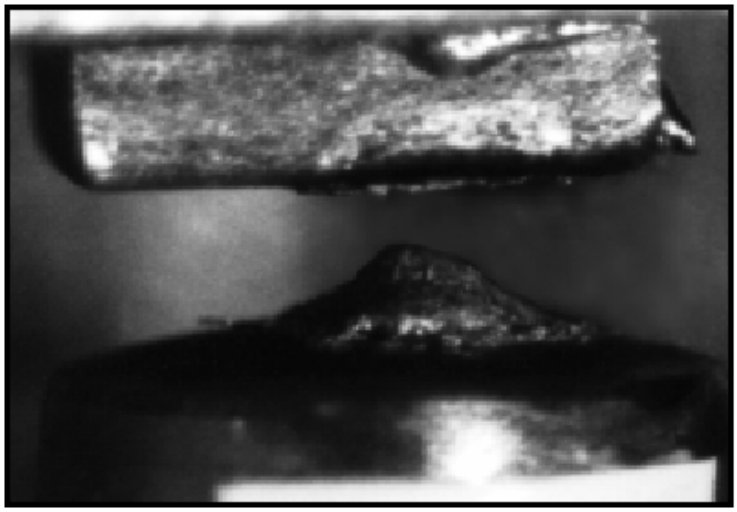

Fig. 1.17. Material transfer at a contact.

Permanent damage, e.g., weld, of the contacts may be a consequence of a sudden raise in temperature at the interface. However, the spring constant of the microswitch arm, in this case the cantilever, can prevent formation of the weld. The force with which the arm comes back to its "open" position has to be sufficient to break the weld.

Even if permanent welding does not take place while operating the microswitch, material wear can still occur. According to Bowen and Tabor's adhesion theory (Kalpakjian and Schmid, 2001), welding can also occur when two not perfectly smooth bodies are in contact, while subjected to a normal force, without any current passing through them. The concentrated contact force causes plastic deformations and as a result

the contact forms an adhesive bond, i.e., microweld. A sufficient tangential force, or friction force, is required to shear the junctions and break the bonds.

As a result, the contact interface wears out. This wear can be classified as (a) adhesive, or galling, wear, or (b) burnishing wear, Fig. 1.18. The adhesive wear is characterized by transfer of material and high coefficients of friction. However, the burnishing wear involves relatively low coefficients of friction and negligible transfer of material.

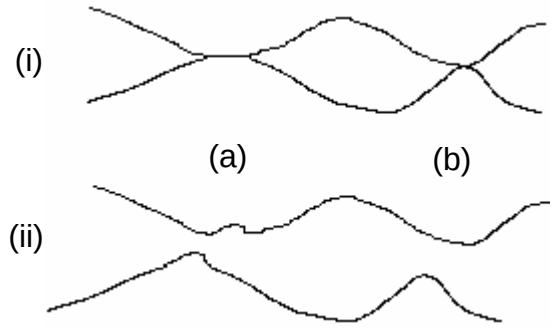

Fig. 1.18. Illustration of (i) adhesively bonded contacts and (ii) material wear after application of tangential force: (a) adhesive wear, (b) burnishing wear.

In order to minimize the wear in the contacts an appropriate surface finish technique must be used in the RF microswitch manufacturing process. There is a wide range of thin metal film deposition techniques available in MEMS fabrication (Pryputniewicz and Furlong, 2002). These techniques include ion implantation, evaporation, sputtering, chemical vapor deposition (CVD), Fig. 1.19, and electroplating, Fig. 1.20. Most commercially available materials can be deposited on RF MEMS switch contacts using one of the above listed techniques.

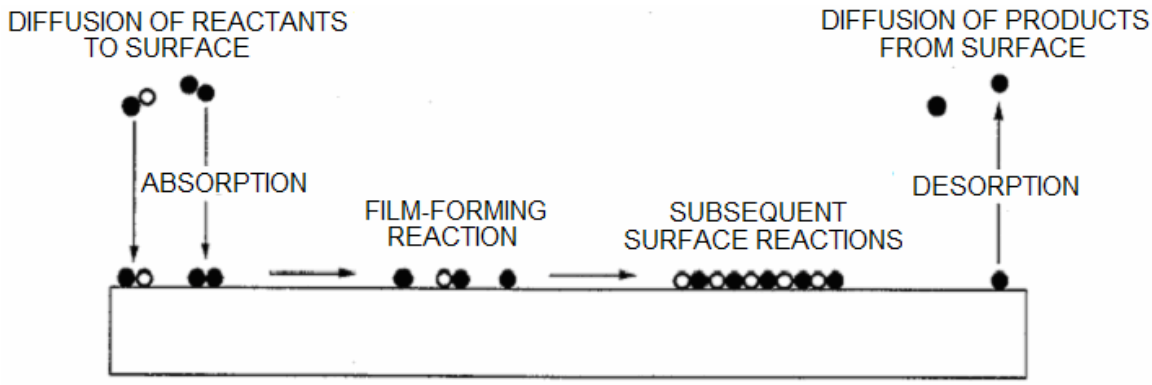

Fig. 1.19. Sequence of reaction steps in the CVD process.

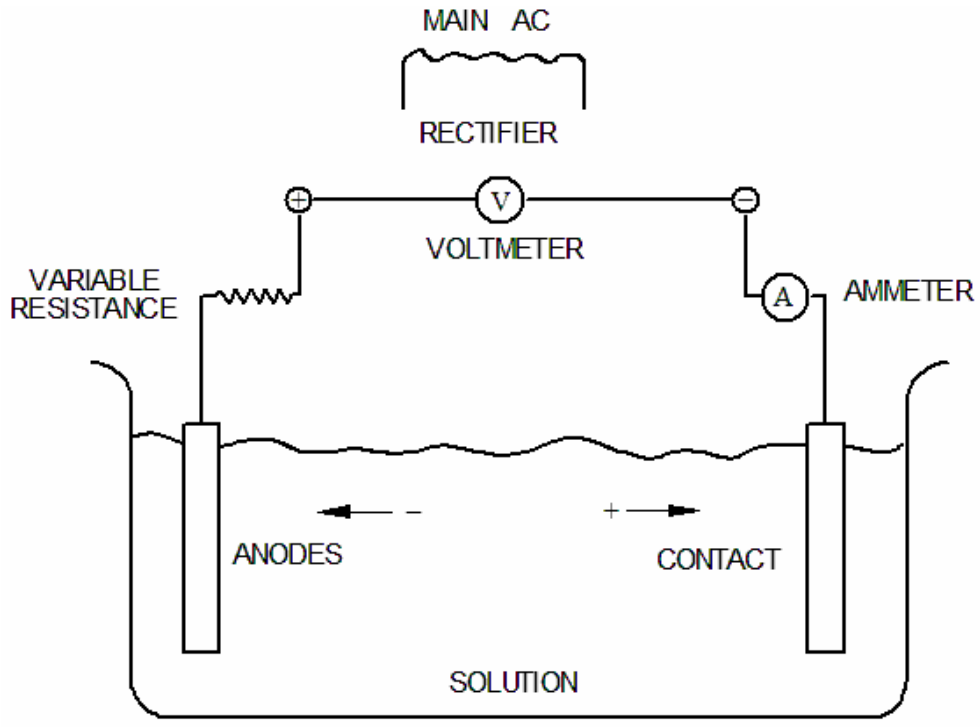

Fig. 1.20. Schematic illustration of an electroplating cell.

1.4.2. Contact material

Contact material is another important parameter which has to be carefully chosen in the design process of any MEMS in order to increase the overall life of the finished

device. Most often metals are chosen as the contact material, each metal however, with its unique properties can greatly affect the microswitch reliability. Table 1.2 (Tyco, 2000a) summarizes some contact metal characteristics, which are also described in detail in Sections 1.4.2.1 and 1.4.2.2.

Table 1.2. Characteristics of various contact materials.

Material	Electrical conductivity %IACS	Arc voltage	Arc current
Cadmium	24	10	0.5
Silver	105	12	0.4
Gold	77	15	0.38
Copper	100	13	0.43
Nickel	25	14	0.5
Palladium	16	15	0.5
Tungsten	31	15	1.0

1.4.2.1. Pure metals

Fine silver has the best electrical and thermal properties of all metals. Unfortunately, silver is affected by sulfidation of about 70 micrograms per square centimeter per day (Tyco 2000a). Sulfidation forms a film on the contact surface which increases the interface resistance. The sulfidation film has also been known to capture airborne dirt particles. The wiping, or contact, force of the closing microswitch has to be large enough to break through the formed film in order to create a good electrical contact (Pryputniewicz, et al., 2001a).

Gold flashing on each of the contacts results in almost no sulfidation at all and provides good electrical conductivity. Gold also does not oxidize, assuring always

conducting contact area. However, due to low melting temperature, gold has tendency of coming off the contact if it is in an environment at temperatures above 350˚C.

Palladium contacts do not oxidize or sulfidate, but have a very low electrical conductivity. The palladium life is ten times that of fine silver, which makes it a good choice for a contact from the reliability stand point.

1.4.2.2. Alloys

Silver alloyed with 0.15% nickel gives the contact a fine grain structure. As a result the material transfer from one contact to another is more evenly distributed, thus delaying contact failure.

Silver cadmium oxide is much more resistant to material transfer and material loss due to arcing than fine silver, but is much less electrically conductive. This alloy also has a higher interface resistance and a greater contact assembly heat rise. Like fine silver it will both oxidize and sulfidate with time.

Although it is very rare, silver tin indium oxide exhibits better resistance to arc erosion and welding than silver cadmium alloy. Silver tin indium is less electrically conductive, even though it is harder than silver cadmium. It also has a greater interface resistance, thus greater voltage drop and a heat rise.

1.4.3. Anti-stiction coating

Stiction presents a major problem in microswitch design. The in-use-stiction, one that occurs when parts come into contact, causes permanent collapse of the designed structure. The capillary, electrostatic, and van der Waals forces are primarily responsible for this stiction. Capillary and electrostatic forces can be eliminated by treating the surfaces and making them hydrophobic. The Self-Assembly Monolayer (SAM) coating dramatically reduces stiction due to the capillary and electrostatic forces, while reducing friction and wear (Maboudian, el al., 2000). The van der Waals forces, however, can only be reduced by roughening the surfaces. Unfortunately this further reduces the contact area between the electrodes increasing the Joule heat effect.

1.4.4. Contact resistance

Much work has been done to model contact areas and their interface. Works of Greenwood (1966), Greenwood and Williamson (1966), Chang, el al. (1987), and Bhushan (1996, 1998) show much attempt in finding methods to describe mathematically the actual areas that come in contact when two surfaces make an intimate interface. The interface conductance and resistance depend on the actual contact area.

A thorough investigation done by University of California at Berkeley (Chang, et al., 1987) incorporated both elastic and plastic deformations of contacting asperities. Asperity deformation, ζ, Fig. 1.21, due to applied pressure can be calculated as

$$\zeta = \left(\frac{\pi p_m}{2E} \right)^2 R \quad , \tag{1.6}$$

where p_m is the maximum contact pressure, E is the modulus of elasticity, and R is the original asperity radius. The change ζ in the asperity radius is less then or equal to critical radius deformation, ζ_c, which is defined as

$$\zeta_c = \left(\frac{\pi Y \sigma_y}{2E} \right)^2 R \quad , \tag{1.7}$$

where Y is the yield coefficient and σ_y is the yield strength of the material. Material below the distance d, Fig. 1.21, is not affected by the deformation.

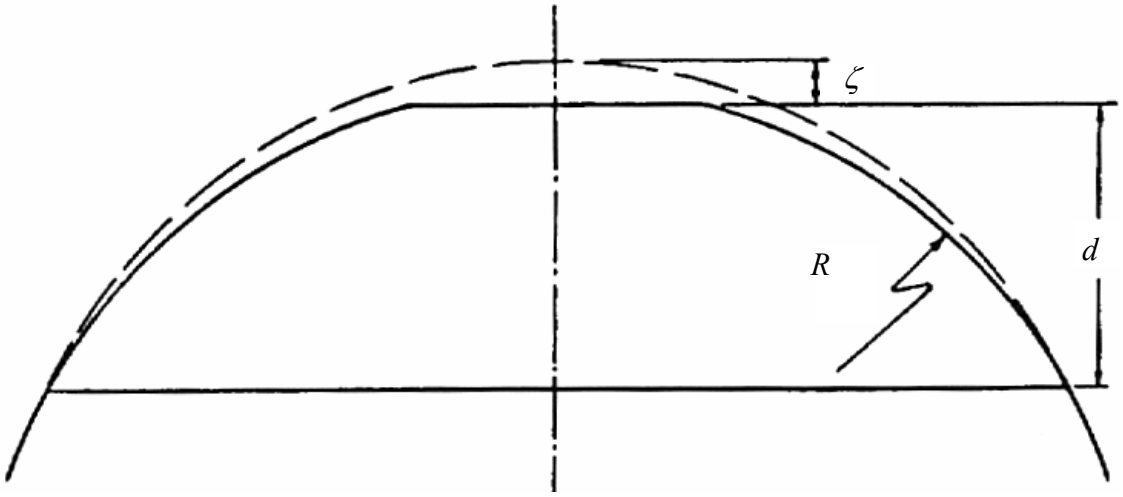

Fig. 1.21. Deformed asperity.

Reid and Starman (2003) show that Holm radius can be used as means of determining the actual area of a contact. As the area of contact is assumed to be within the Holm radius, Fig. 1.22, the contact resistance, R_C, can be written as

$$R_C = \rho_e \left(\frac{1}{2na} + \frac{1}{2\alpha} \right) \quad , \tag{1.8}$$

where ρ_e is the electrical resistivity, a is the average contact asperity radius, n is the number of asperities per unit area, and α is the Holm radius.

Greenwood and Williamson (1966) model for contacts involved both single and multiple asperities, however, their studies were based solely on elastic contact modeling. What this means is that the modeling was considering only small contact loads that were not large enough to plastically deform the asperities in contact. The modeling was based on the Hertz theory for elastic deformation (Greenwood and Williamson, 1966), originally developed for contact interfaces in meshed gears. The equation developed for calculating the interface contact resistance as proposed by Greenwood and Williamson (1966) is

$$R_C = 2\rho_e \left(\frac{1}{4na} + \frac{3\pi}{32nd_c} \right) \quad , \tag{1.9}$$

where d_c is the average center to center distance between contacting asperities.

Another equation proposed for calculating the contact resistance at the interface is given by Mroczkowski (1998) as

$$R_C = \frac{\rho_e}{na} + \frac{\rho_e}{D} \quad , \tag{1.10}$$

where D is the diameter of the area over which the contacts are distributed, while other parameters are as defined previously.

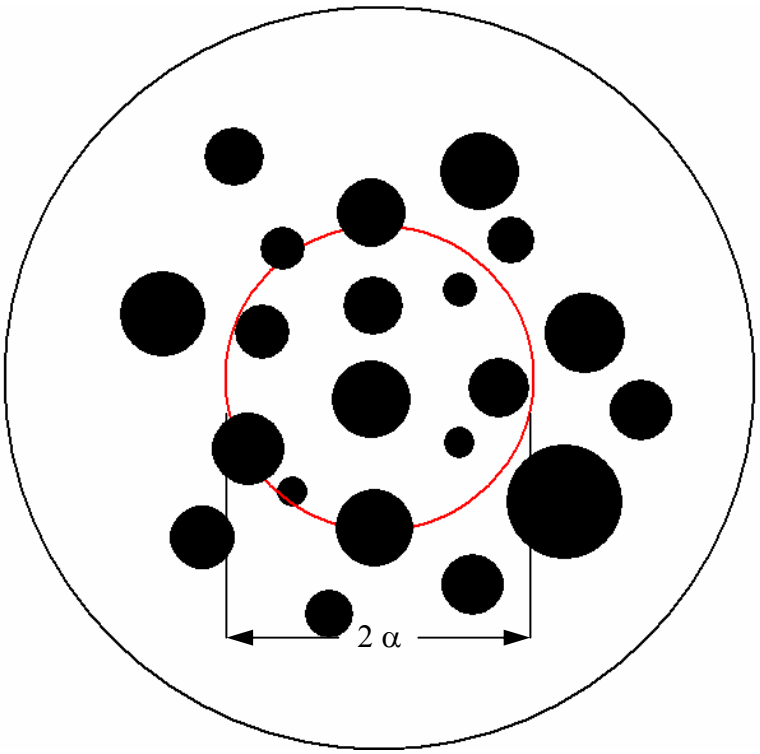

Fig. 1.22. Holm radius representation.

1.5. Integrated circuits

One of the ways to reduce Joule heat is by lowering the current passing through the microswitch. In order to do so, the design of the integrated circuit (IC), that incorporates the RF MEMS switch, should be optimized. According to Tyco (2000a), in order to minimize current passing through the contact interface, to consequently lower the heat energy, a resistor-capacitor (RC) network can be placed in parallel with the microswitch, as shown in Fig. 1.23. The current would then be shunted into the capacitor and the capacitor-discharge-limiting resistor. The resistor isolates the capacitor from the microswitch contacts and so for the best results it should be kept at a minimum value.

In order to prevent the microswitch from receiving the counter-voltage, diodes can be put into the system. The diode does not let any current back into the microswitch. It does, however, increase hold-up time of the inductive load. An additional resistor can be placed in series with the diode to reduce the hold-up time. Nonetheless, the resistor does reduce the effectiveness of the diode.

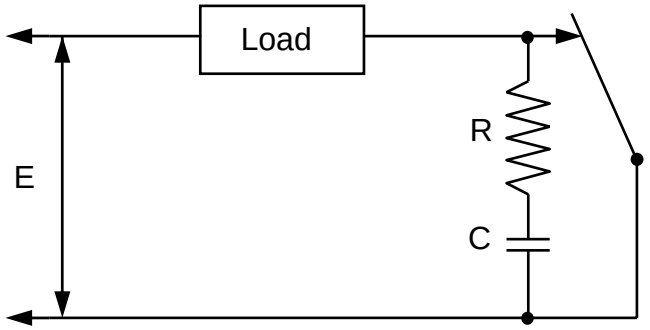

Fig. 1.23. Sample RC circuit.

2. RF MEMS SWITCH CONSIDERED

The RF MEMS switch considered in this thesis is a cantilever-type contact microswitch. This microswitch was manufactured by Cronos (2002) using the MUMPs technology. A photograph of the microswitch is shown in Fig. 2.1. The microswitch geometry used in calculations included in this thesis is illustrated in Fig. 2.2, while the numerical values of all the dimensions included in the figure are listed in Table 2.1.

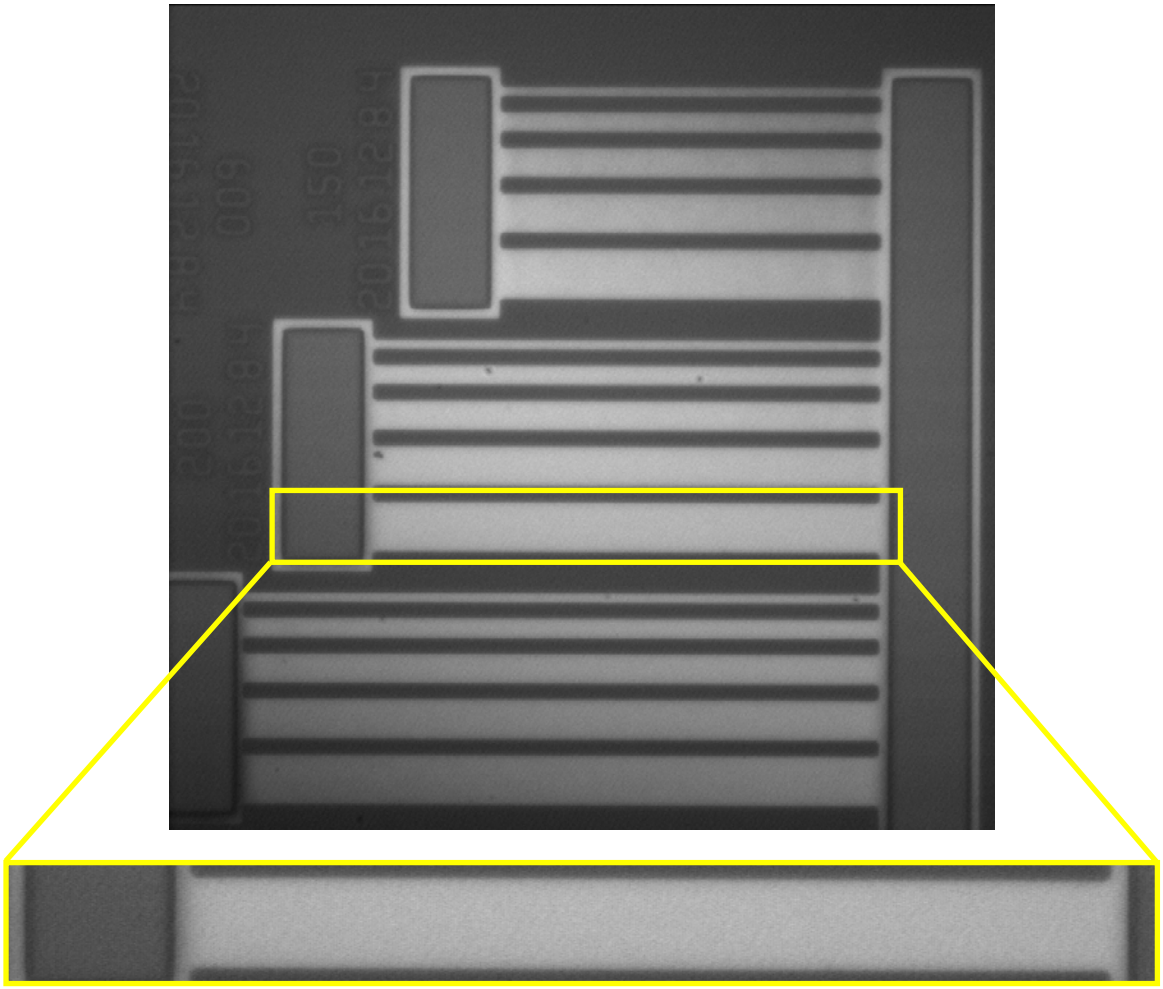

Fig. 2.1. Cronos cantilever-type contact RF MEMS switch.

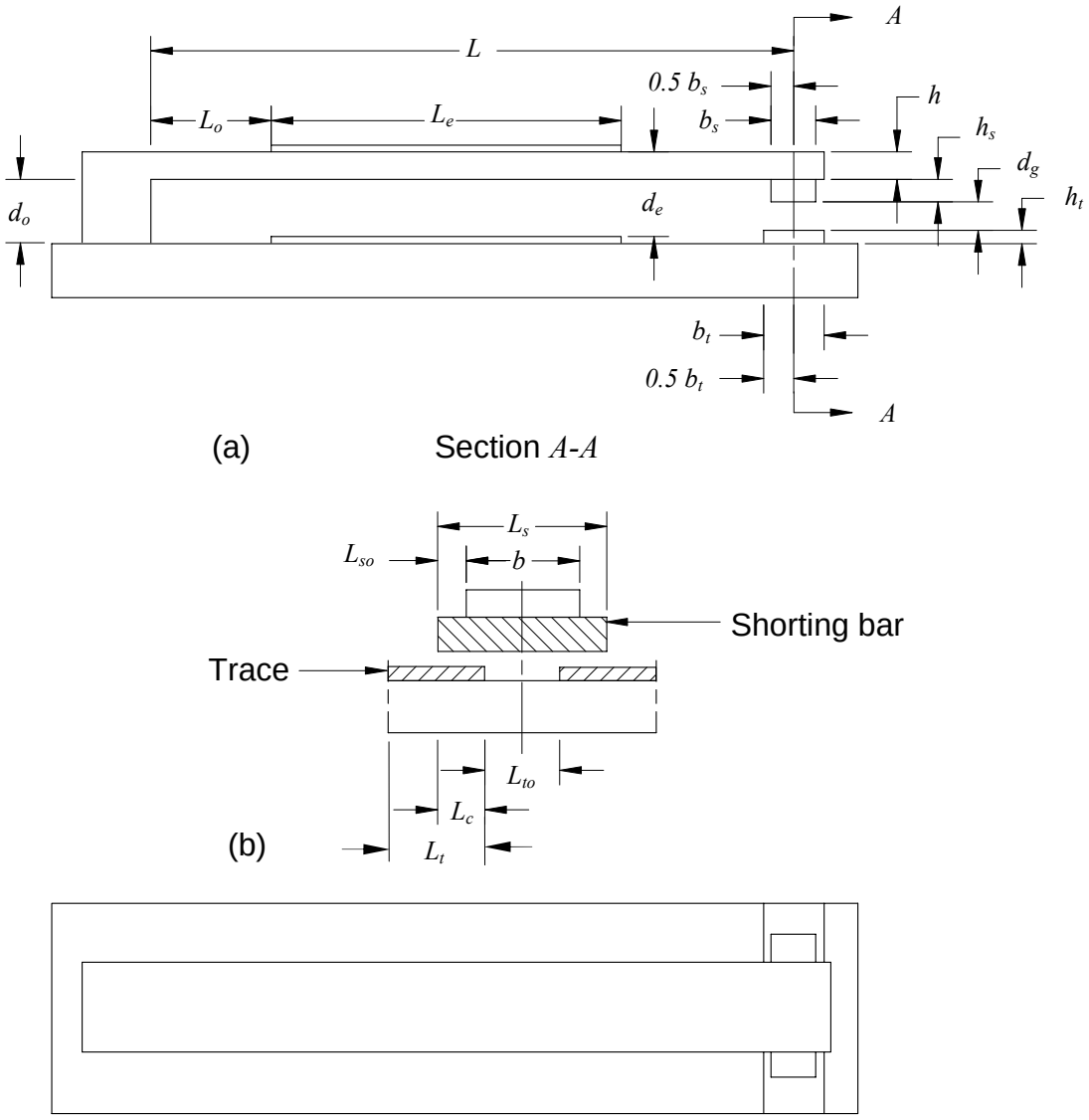

Fig. 2.2. Geometry and dimensions of the RF MEMS switch: (a) cross section, (b) top view.

The microswitch was manufactured using the MUMPs process that uses polysilicon as a structural layer. Material properties used in the calculations are listed in Table 2.2 (Pryputniewicz and Furlong, 2002).

Table 2.1. Dimensions of the RF MEMS switch, Fig. 2.2.

Dimensions of the microswitch	Value	Units
Cantilever length, L	200	μm
Cantilever width, b	20	μm
Cantilever thickness, h	2.5	μm
Distance from the post to electrode, L_o	12	μm
Distance at which the cantilever is suspended, d_o	2.5	μm
Electrode length, L_e	150	μm
Distance between the electrodes, d_e	4.5	μm
Shorting bar length, L_s	26	μm
Shorting bar width, b_s	6	μm
Shorting bar thickness, h_s	1	μm
Length of the contact area, L_c	6	μm
Contact gap distance, d_g	1	μm
Discontinuity in trace under shorting bar, L_{to}	14	μm
Trace length, L_t	80	μm
Trace width, b_t	12	μm
Trace thickness, h_t	0.5	μm

Table 2.2. Material properties of polysilicon.

Property	**Value**	**Units**
Density, ρ	2.33	g/cm^3
Modulus of elasticity, E	160	GPa

This RF MEMS switch is actuated by induced electrostatic force between two parallel conductive plates, the electrodes, one located on the cantilever and the other on the substrate of the microswitch. The voltage induced force brings the two electrodes together bending the cantilever and causing the two end contacts to touch. The touching ends close the conduction path and allow transmission of an electrical signal. As the

voltage between the electrodes is reduced, the elasticity of the cantilever is used to restore its original, off position.

For the thermal analyses the nominal value of the electrical current used was 300 mA, while the contact resistance was set at 1 Ω, for initial considerations. The current and contact resistance values are based on MEMS research at Motorola, Inc. Using these values of current and resistance the total power produced at the contacts of the microswitch was 0.18 W.

3. METHODOLOGY

Characterization of the RF microswitch considered in this thesis was performed using analytical, computational, and experimental solutions (ACES) methodology (Pryputniewicz, 1997). ACES methodology integrates the analytical, computational and experimental modes of solving a problem, while assuring the integrity of the obtained results, Fig. 3.1.

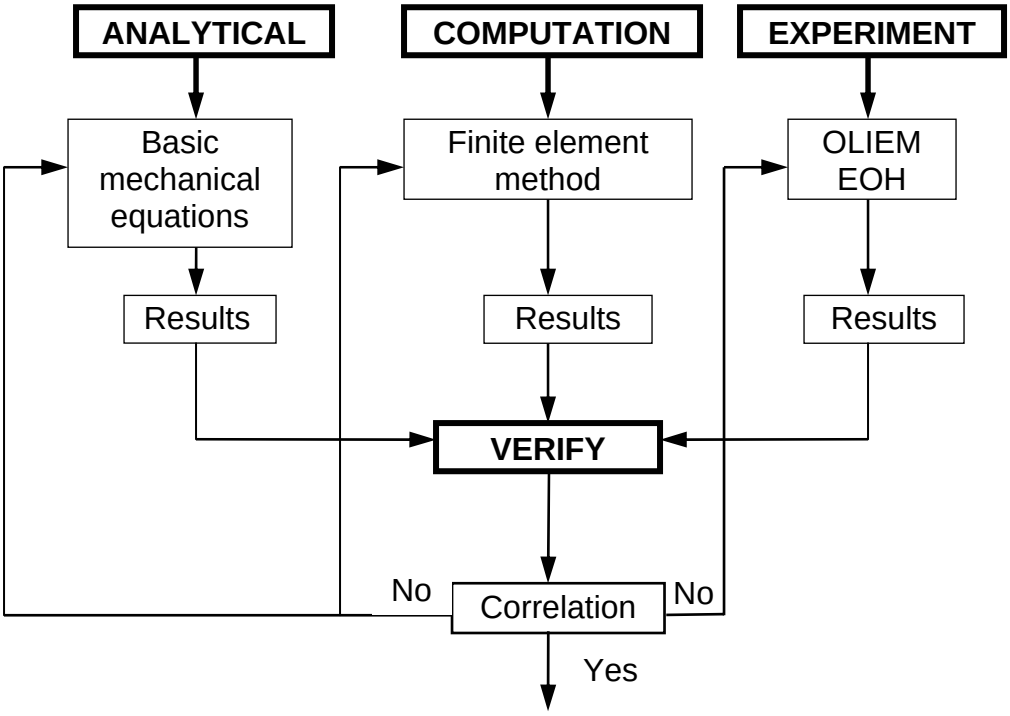

Fig. 3.1. Configuration of the ACES methodology.

3.1. Analytical methods

Analytical calculations were performed to describe mechanical and thermal behavior of the RF microswitch during its operation. The mechanical behavior, defined

in terms of, e.g., stiffness or frequency, was taken into consideration. Thermal calculations, performed in this thesis, include analyses of Joule heat and dissipation of this heat.

3.1.1. Mechanical performance

The RF MEMS switch can be analyzed as a one-dimensional model, Fig. 3.2. The spring in the model represents the spring constant of the cantilever, while the capacitor denotes the capacitance present between the two electrodes, which may also represents an electrostatic force present between the electrodes. In order for the model to be in equilibrium, the summation of forces acting on the cantilever must be equal to zero, Fig. 3.3, i.e.,

$$+\downarrow \sum F = F_{ES} - F_k = 0 \quad , \tag{3.1}$$

where

$$F_{ES} = \frac{1}{2}\frac{\varepsilon_o \varepsilon_r L_e b_e V^2}{{d_e}^2} \tag{3.2}$$

and

$$F_k = kx \quad . \tag{3.3}$$

In the Eq. 3.2, ε_o is the dielectric constant of air, ε_r is the relative permittivity of the material between electrodes, L_e is the length of the electrode, b_e is the width of the electrode, V is the voltage drop between the electrodes, and d_e is the distance between the

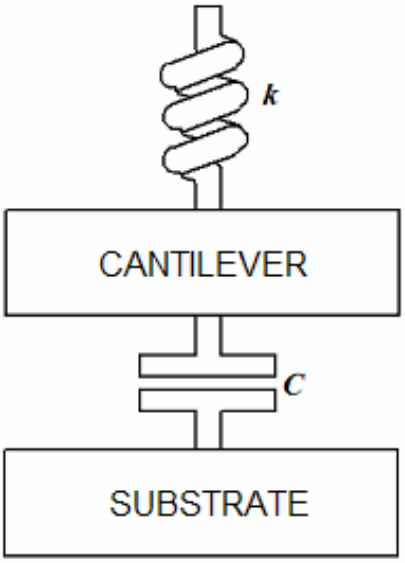

Fig. 3.2. One-dimensional model of the RF MEMS microswitch (Reid and Startman, 2003).

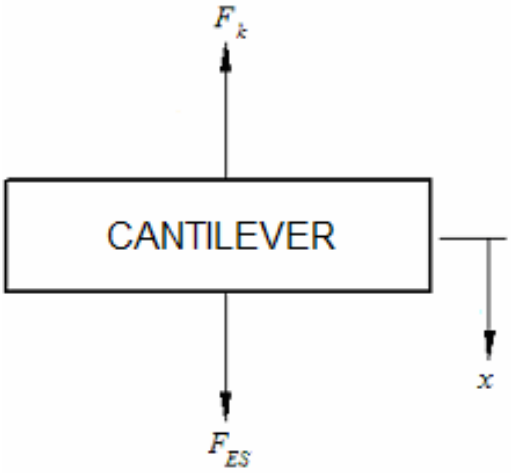

Fig. 3.3. Equivalent free body diagram for the cantilever beam.

two electrodes. With the force calculated in Eq. 3.2 the spring constant, *k*, of the cantilever can be found as

$$k = \frac{1}{2}\frac{\varepsilon_o \varepsilon_r L_e b_e V^2}{d_g {d_e}^2} \quad , \tag{3.4}$$

where d_g is the distance between the "open" contacts of the microswitch.

The voltage, V, necessary to actuate the microswitch depends on the area and the properties of the material used for the electrodes (Reid and Starman, 2003)

$$V = \sqrt{2\frac{F{d_e}^2}{\varepsilon_o \varepsilon_r L_e b_e}} \tag{3.5}$$

where d_e is the distance between the electrodes. It must be remembered, however, that due to stress relaxation, with time, the stiffness of the cantilever may chance. The cantilever spring constant may change as time progresses, thus the electrostatic force, F_{ES}, obtained from Eq. 3.2 may vary with time.

The dynamic mass, m, of the cantilever can be calculated using the following equation (Pryputniewicz and Furlong, 2002):

$$m = \frac{33}{140}\rho bhL \quad , \tag{3.6}$$

where ρ is the density of the cantilever material, b and h are its width and thickness, respectively, and L is its active length. Using the dynamic mass and the spring constant of the cantilever, fundamental natural frequency, f_o, of the cantilever can be found to be (Pryputniewicz, 2001; Pryputniewicz and Furlong, 2002; Hsu, 2002)

$$f_o = \frac{1}{2\pi}\sqrt{\frac{k}{m}} \quad . \tag{3.7}$$

Detailed calculations of the parameters from Eqs 3.2 to 3.7 are included in Appendix A.

The end contacts are the only electrical conductors that allow signals to pass through the interface as soon as the microswitch is actuated and the contact gap is closed. The current passing through the interface is a source of thermal energy, due to Joule heat, which may be catastrophic to the microswitch. The Joule heat is distributed throughout the microswitch via heat transfer as described in Section 3.1.2.

3.1.1.1. Cantilever deformations

The microswitch behaves as a cantilever fully constrained at one end. The beam bends due to the electrostatic force generated between the electrodes. The electrostatic force acting over the overlap area of the electrodes can be expressed as a concentrated force in a geometric center of the overlap. This assumption was utilized in all of the analytical calculations; it was correlated with the results of computational modeling of the electrostatic force distributed, rather than concentrated, between the electrodes.

The concentrated actuation force is not at the end of the cantilever but is acting in the middle of the overlap area of the electrodes. Therefore, for the calculation purposes, the cantilever was divided into two sections: section-1, from the fixed end to the point of application of the equivalent concentrated electrostatic force, and section-2, from the point of application of this force to the free end of the cantilever, Fig. 3.4; lengths of these sections were denoted as L_1 and L_2, respectively.

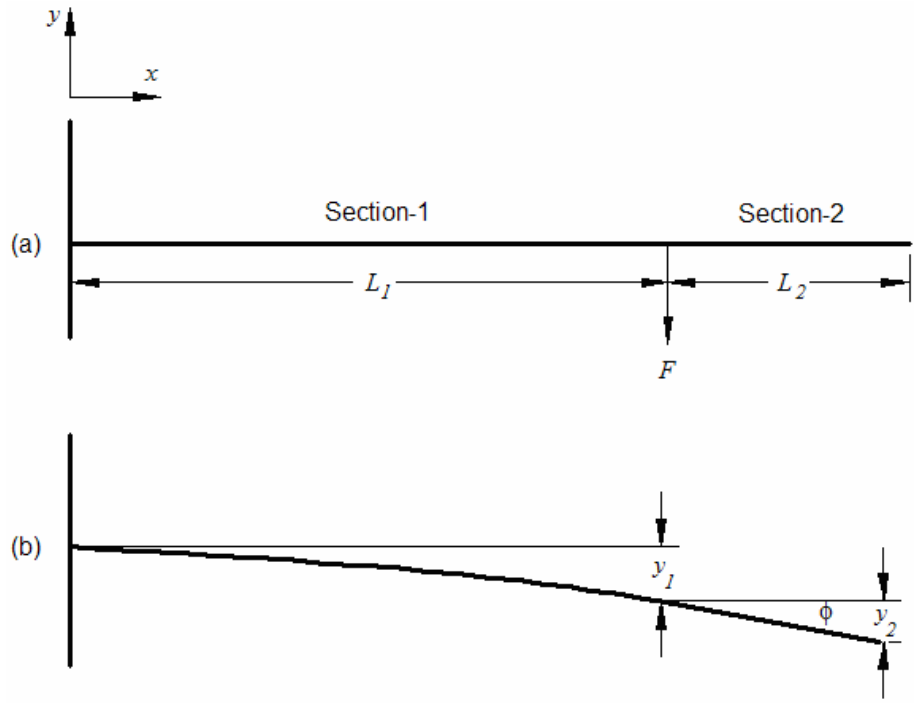

Fig. 3.4. Deformations of electrostatically actuated cantilever: (a) at the beginning of actuation (zero deformation), (b) at the end of actuation (maximum deformation).

In order to describe the shape of the loaded part of the cantilever, deformations of section-1 can be determined using equation of the elastic curve, i.e.,

$$EI\frac{d^2y}{dx^2} = M(x) \quad , \tag{3.8}$$

where E is the modulus of elasticity of the material the cantilever is made of, I is the second moment of area for the cantilever, and M is the bending moment. Second moment of area, or moment of inertia, for an area A in the yz plane, Fig. 3.5, can be calculated as

$$I_{yy} = \int_y z^2\, dA \quad , \tag{3.9}$$

or

$$I_{zz} = \int_z y^2 \, dA \quad , \tag{3.10}$$

depending which axis is the neutral axis. In reality Eqs 3.9 and 3.10 include two integrals, because dA is in terms of dy and dz. For a rectangular area of width b and thickness h, the second moment of area about the axis going through the geometric center of the rectangle and parallel to its width, Fig. 3.6, is expressed as

$$I_{zz} = \frac{1}{12} bh^3 \quad . \tag{3.11}$$

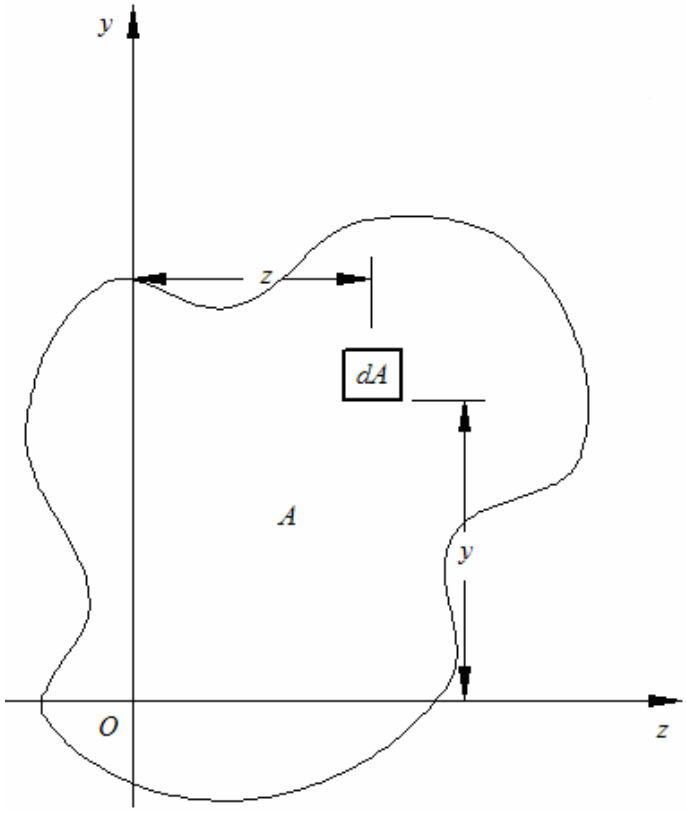

Fig. 3.5. Area in yz plane.

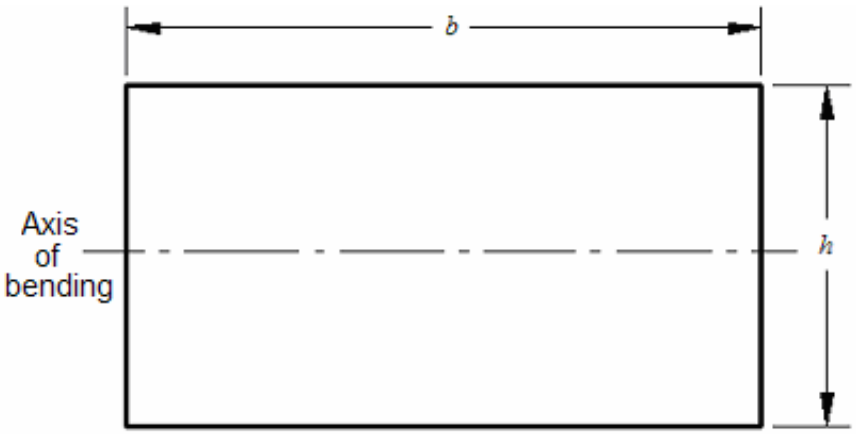

Fig. 3.6. Cross sectional area indicating axis of bending.

Substituting $M(x) = F(x - L_1)$ into Eq. 3.8 and integrating the elastic curve equation once produces a slope, or angle, equation

$$\frac{dy}{dx} = \frac{F}{EI}\left(\frac{1}{2}x^2 - L_1 x\right) + C_1 \quad , \tag{3.12}$$

where C_1 is a constant of integration that must be solved for by applying known boundary conditions. Integrating Eq. 3.12 produces a deformation equation

$$y = \frac{F}{EI}\left(\frac{1}{6}x^3 - \frac{1}{2}L_1 x^2\right) + C_1 x + C_2 \quad , \tag{3.13}$$

where C_2 is the second constant of integration. The constants of integration C_1 and C_2, appearing in Eqs 3.12 and 3.13, can be evaluated subject to boundary conditions characterizing the cantilever, Fig. 3.4, i.e.,

$$\text{at } x = 0 \qquad y\big|_{x=0} = 0 \tag{3.14}$$

and

$$\text{at } x = 0 \qquad \frac{dy}{dx}\bigg|_{x=0} = 0 \quad . \tag{3.15}$$

Solution of Eq. 3.12 subject to Eq. 3.15 yields

$$C_1 = 0 \quad . \tag{3.16}$$

Substituting Eq. 3.16 into Eq. 3.13, and solving the resulting expression subject to Eq. 3.14, we obtain

$$C_2 = 0 \quad . \tag{3.17}$$

Substitution of Eqs 3.16 and 3.17 into Eqs 3.12 and 3.13 yields the following relationships for the slope and deformations of section-1 of the cantilever loaded as shown in Fig. 3.4:

$$\frac{dy}{dx}(x) = \frac{F}{EI}\left(\frac{1}{2}x^2 - L_1 x\right) = \frac{F}{EI}\frac{x}{2}(x - 2L_1) \tag{3.18}$$

and

$$y(x) = \frac{F}{EI}\left(\frac{1}{6}x^3 - \frac{1}{2}L_1 x^2\right) = \frac{F}{EI}\frac{x^2}{6}(x - 3L_1) \quad , \tag{3.19}$$

respectively. Evaluation of Eqs 3.18 and 3.19 at $x = L_1$ provides boundary conditions for determination of slope and deformation of section-2 of the cantilever. Resulting equations for the slope and deformations of section-2 are

$$\frac{dy}{dx}(x) = \frac{1}{2}\frac{F}{EI}{L_1}^2 \tag{3.20}$$

and

$$y(x) = \frac{1}{2}\frac{F}{EI}{L_1}^2(x - L_1) - \frac{1}{3}\frac{F}{EI}{L_1}^3 \quad . \tag{3.21}$$

As the cantilever bends and contact is made by closing the gap d_g, the cantilever is no longer fixed at one end and free at the other, but is now also simply supported at the

previously free end. This fixed – simply supported system is indeterminate, thus both the elastic curve equation, and superposition methods need to be used in order to obtain deformations of the system due to the electrostatic actuation and new boundary conditions. The elastic curve equation was once again utilized to find deformations of the cantilever as a function of position along its length. The solution was obtained as the cantilever was divided to two sections. The boundary conditions were applied according to Fig. 3.7. At the common point of the two sections, the location of the equivalent electrostatic force, continuity conditions were applied.

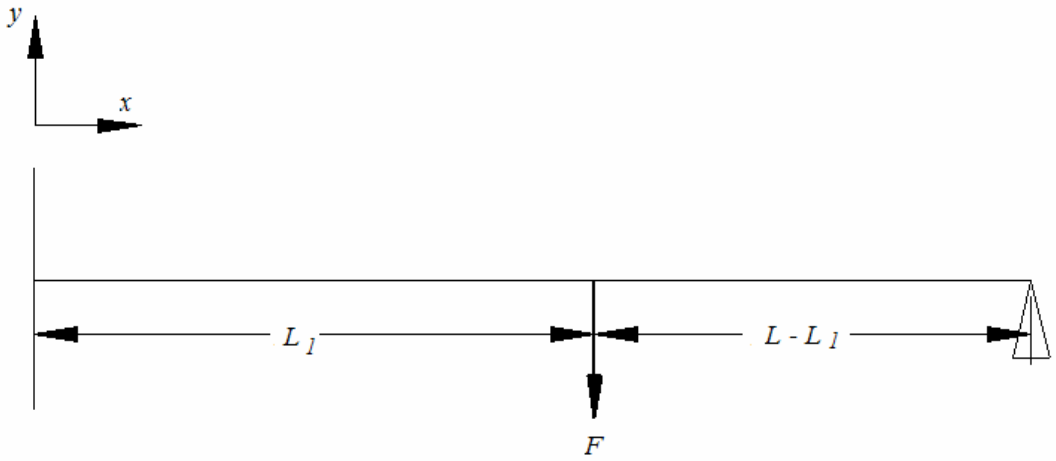

Fig. 3.7. The fixed-simply supported cantilever.

As discussed in Appendix A, the deformation equation for both sections, section-1 denoted by x_1 and section-2 denoted by x_2, is written as

$$y(x)=\frac{1}{EI}\left(\frac{1}{6}Fx_1^{\,3}-\frac{1}{2}FLx_1^{\,2}+\frac{1}{2}FL_1x_1^{\,2}-\frac{1}{6}R_Ax_1^{\,3}-\frac{1}{6}R_Ax_2^{\,3}+\frac{3}{2}FL_1^{\,2}x_2-FLL_1x_2-\frac{5}{6}FL_1^{\,3}+\frac{1}{2}FLL_1^{\,2}\right), \tag{3.22}$$

where

$$R_A = F\left(-6\frac{L_1}{L}+12\frac{{L_1}^2}{L^2}-5\frac{{L_1}^3}{L^3}\right) \quad . \tag{3.23}$$

Equation 3.23, however, does not fully resemble the true boundary conditions of the operating microswitch. The simply supported end of the cantilever is assumed to be level with the fixed end. In reality, the cantilever must bend a distance of the gap d_g before it makes a contact. The deformations of the cantilever with these more realistic boundary conditions can still be described by Eq. 3.22, however, the reaction force R_A changes to

$$R_A = F\left(-6\frac{L_1}{L}+12\frac{{L_1}^2}{L^2}-5\frac{{L_1}^3}{L^3}\right)+\frac{EI}{L^3}6\times10^{-6} \quad , \tag{3.24}$$

where the last term is a result of changed boundary conditions. The force R_A represents the reaction force at the simply supported end of the cantilever at y = 1 μm; for the case of initial contact ideally R_A equals to zero; however, when F increases above nominal contact force R_A achieves nontrivial values. Details of the derivation of Eq. 3.24 are included in Appendix A.

At the simply supported end the cantilever may experience slipping. The force due to slip is a function of the normal force experienced by the end of the cantilever, the curvature of the tip of the cantilever, and the coefficient of friction. For the purposes of illustrating this force no differentiation was made between the static and the kinematic coefficients of friction.

According to the Coulomb friction law,

$$F_S = \mu F_n \quad , \tag{3.25}$$

where F_S is the slip force, μ is the friction coefficient, and F_n is the normal force. Based on Eq. 3.25, the slip force is directly proportional to the normal force with a proportionality constant equal to the coefficient of friction. The coefficient of friction dependents on the nature of the surface and the materials in contact. In this thesis a range of coefficients of friction used was from 0.15 to 0.60 (Beer and Johnston, 1996).

Both the reaction force and the slip force have great effect on the wear of the contact. Their values then have a direct impact on the overall reliability of the microswitch. Detailed calculations of deformations of the cantilever are included in Appendix A.

3.1.2. Thermal analysis

Heat generated by the current flowing through the microswitch and across the contact interface is the source of thermal energy (Holman, 2002). Using the internal electrical resistance of the microswitch, R, and the current, I, passing through it, the Joule heat, Q_J, can be determined as

$$Q_J = RI^2 \quad . \tag{3.26}$$

The internal resistance, R, of the microswitch is mainly due to the contact resistance, R_C, but it also depends on the electrical properties of the conducting material and the geometry of the conductor, R_E, Fig. 3.8, and can be represented as

$$R = R_C + R_E \quad . \tag{3.27}$$

The contact resistance depends on the characteristics of the interface. As discussed in Section 1.4.4 the contact resistance can be calculated using Eqs 1.8 to 1.10. Perhaps the most appropriate contact resistance equation is (Reid and Starman, 2003)

$$R_C = \rho_e \sqrt{\frac{\pi H}{4F_n}} \quad , \tag{3.28}$$

where ρ_e is the electrical resistivity that is specific to the conducting material, H is the hardness of that material, and F_n is the normal force.

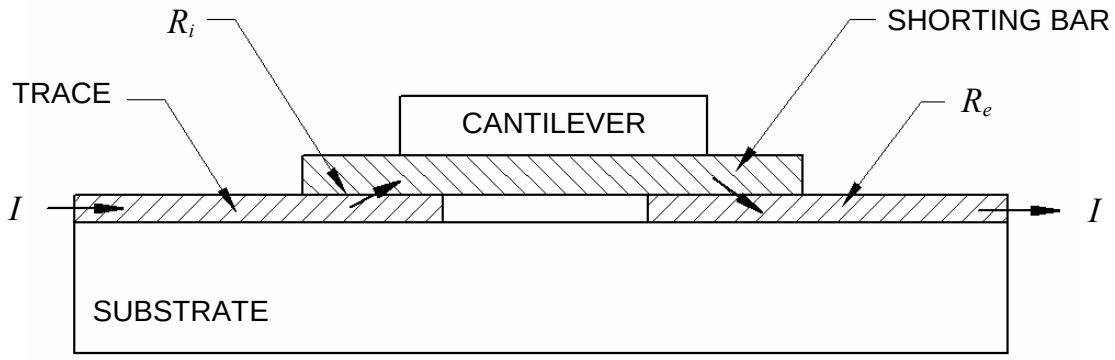

Fig. 3.8. Current flow through the microswitch contact areas.

The electrical resistance of the conducting material depends on electrical resistivity of the material out of which the conductor is made, the cross sectional area, A, of the conductor, and the length of the conductor, L, (Pryputniewicz, 2001), i.e.,

$$R_e = \rho_e \frac{L}{A} \quad . \tag{3.29}$$

The Joule heat is dissipated by tree modes of heat transfer (Pryputniewicz, 2001): convection, Q_c, conduction, Q_k, and radiation, Q_r, i.e.,

$$Q_J = Q_c + Q_k + Q_r \quad . \tag{3.30}$$

The heat due to convection will be transferred away by natural convection, since no air flow is present in the immediate vicinity of the microswitch. The microswitch itself will be modeled as a flat horizontal beam. The convected energy can be calculated as

$$Q_c = hA_c(T_s - T_\infty) \quad , \tag{3.31}$$

where A_c is the area through which heat is transferred by convection, T_s is the surface temperature, T_∞ is the ambient temperature, and h is the convective heat transfer coefficient defined as

$$h = \frac{\overline{Nu}k}{L} \quad , \tag{3.32}$$

where k is thermal conductivity of the medium surrounding the microswitch, L is the length of the cantilever from which the heat is convected away, and Nu is the Nusselt number calculated using (Holman, 2002)

$$\overline{Nu_L} = 0.13(Gr_L \Pr)^{1/3} \quad \text{for} \quad Gr_L \Pr < 2\times10^8 \quad , \tag{3.33}$$

or

$$\overline{Nu_L} = 0.16(Gr_L \Pr)^{1/3} \quad \text{for} \quad 2\times10^8 < Gr_L \Pr < 10^{11} \quad , \tag{3.34}$$

In the Eqs 3.33 and 3.34 Pr is the Prandtl number defined as a function of temperature for specific materials, while Gr is the Grashof number defined by the following equation:

$$Gr_L = \frac{g\beta(T_s - T_\infty)L^3}{\nu^2} \quad , \tag{3.35}$$

where g is the gravitational acceleration, β is the volume coefficient of expansion equal to the reciprocal of the ambient temperature in absolute degrees, but only if the convecting fluid is assumed to be an ideal gas, and v is the kinematic viscosity of the convecting fluid.

Heat transfer by conduction, Q_k, for one-dimensional flow, can be determined using Fourier's Law

$$Q_k = -kA_k \frac{dT}{dx} \quad , \tag{3.36}$$

where k is thermal conductivity of the material, A_k is the area through which conduction takes place, and $\frac{dT}{dx}$ is the temperature gradient in the direction of heat flow.

Equation 3.36 may be written in terms of individual resistances: the thermal resistance of the conductor and the thermal resistance of the contact. The thermal resistance of the conductor can be found using

$$R_k = \frac{x}{kA_k} \quad , \tag{3.37}$$

where x is the distance the heat flux travels, k is the thermal conductivity, and A_k is are cross sectional area through which heat travels by conduction. The thermal contact resistance is defined as

$$R_c = \frac{1}{h_c A_c} \quad , \tag{3.38}$$

where h_c is the contact coefficient, which in general is directly proportional to the surface roughness and A_c is the contact area, and can be found in Norris, et al. (1979). Therefore, Eq. 3.36 can be rewritten as

$$Q_k = \frac{T_1 - T_3}{\left(\frac{x_A}{k_A A_A}\right) + \left(\frac{1}{h_c A_c}\right) + \left(\frac{x_B}{k_B A_B}\right)} \quad , \tag{3.39}$$

where T_1 and T_3 are the temperatures at two opposite ends of the microswitch, and other parameters are as shown in Figs 3.9 and 3.10.

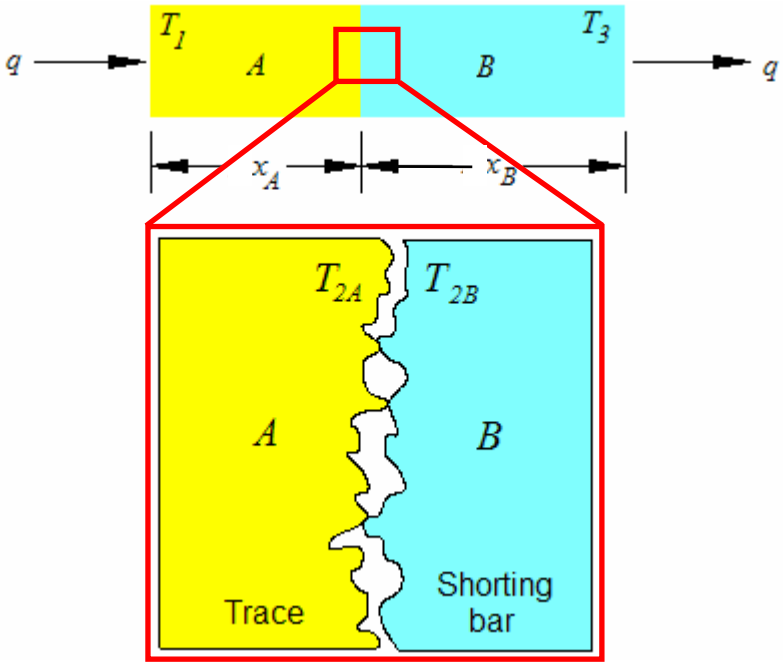

Fig. 3.9. Contact resistance in conduction.

The heat transfer due to radiation for a microswitch that is enclosed by a package may be written as follows (Pryputniewicz, et al., 2001b, 2001c):

$$Q_r = \varepsilon_s \sigma A_r F_s \left(T_s^{\,4} - T_e^{\,4} \right) \quad , \tag{3.40}$$

where ε_s is the emissivity of the surface, σ is the Stefan-Boltzmann constant, A_r is the area of the surface subjected to heat transfer by radiation, F_s is the geometric view factor defining interchange of energy transferred by radiation between the surface and its enclosure, T_s is the temperature of the surface of the microswitch, T_e is the temperature of the enclosure.

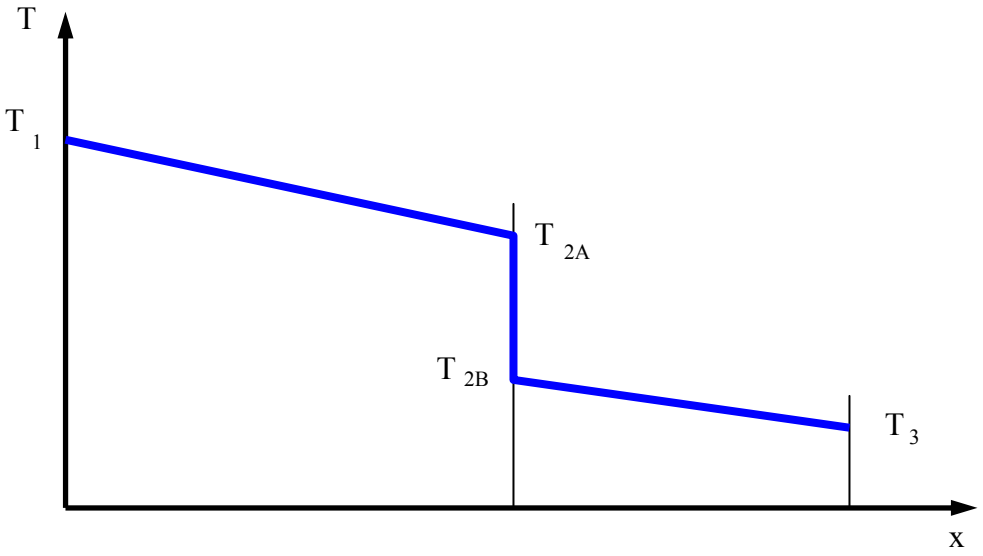

Fig. 3.10. Temperature distribution across an interface.

3.1.3. Maximum microswitch temperature

The temperature of the operating microswitch can also be estimated using the voltage-temperature relation in metallic constrictions (Reid and Starman, 2003). This temperature is computed based on electrical properties of the conducting material in the RF MEMS switch. The voltage-temperature relationship is developed based on Weidemann-Franz law

$$\rho_e k = L_r T \quad , \tag{3.41}$$

where ρ_e is the electrical resistivity, k is the thermal conductivity, L_r is the Lorenz number, and T is the temperature. The Lorenz numbers for common metals are listed in Table 3.1.

Table 3.1. The Lorenz numbers for common metals.

Metal	$L_r\ 10^8\ W\ \Omega\ K^{-2}$	
	273 K	373 K
Ag	2.31	2.37
Au	2.35	2.40
Cd	2.42	2.43
Cu	2.23	2.33
Ir	2.49	2.49
Mo	2.61	2.79
Pb	2.47	2.56
Pt	2.51	2.60
Sn	2.52	2.49
W	3.04	3.20
Zn	2.31	2.33

The voltage-temperature relation in metallic constrictions is written as (Reid and Starman, 2003)

$$T_s^{\,2} - T_\infty^{\,2} = \frac{V^2}{4 L_r} \quad , \tag{3.42}$$

where T_s is the maximum surface temperature, T_∞ is ambient temperature, and V is voltage. The voltage can be calculated using Ohm's law

$$V = IR \quad , \tag{3.43}$$

where V denotes the voltage, I denotes the electrical current, and R denotes the electrical resistance. Since the voltage-temperature relation, given by Eq. 3.42, works for metallic constrictions, the resistance used there is the individual contact resistance. Complete calculations and results of the maximum switch temperature can be found in Appendix B.

3.2. Computational methods

Computer software was used to model the mechanical and thermal characteristics of the RF MEMS switch considered. The software used in the computational part of ACES methodology was based on a finite element method.

3.2.1. Mechanical analysis

Computer design and analysis program was used to develop a three-dimensional model of the microswitch that was considered in this thesis. Finally, the mechanical behavior, characterized by deformations of the cantilever, was analyzed.

3.2.1.1. Pro/ENGINEER model

The microswitch modeled was a cantilever-type RF microswitch, Fig. 3.11. The nominal dimensions used in this study are: L = 200 μm, b = 20 μm, h = 2.5 μm, L_o = 12

μm, d_o = 2.5 μm, L_e = 150 μm, d_e = 4.5 μm, L_s = 26 μm, b_s = 6 μm, h_s = 1 μm, L_c = 6 μm, d_g = 1 μm, L_t = 80 μm, L_{to} = 14 μm, b_t = 12 μm, and h_t = 0.5 μm.

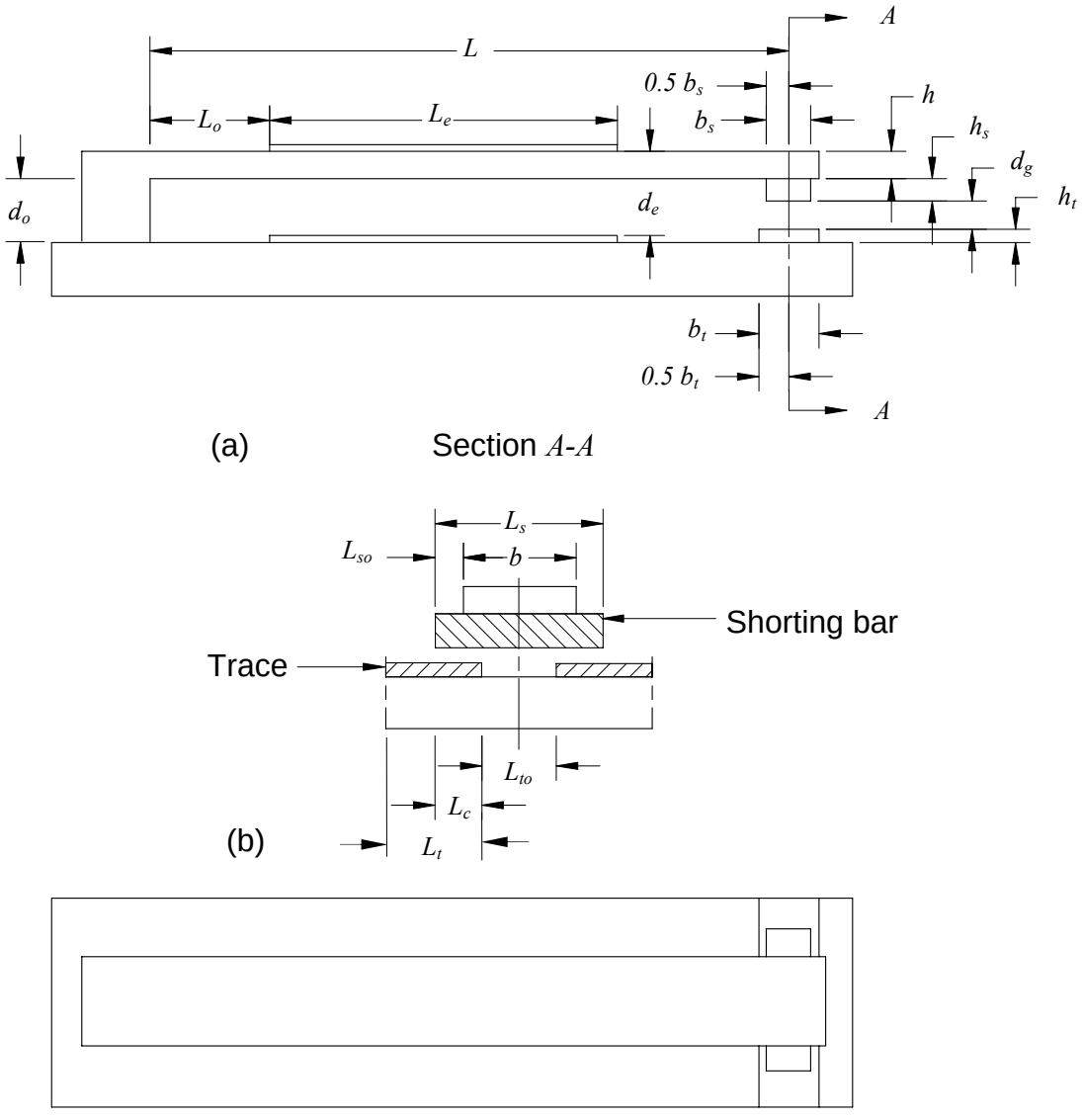

Fig. 3.11. Geometry and dimensions of the RF microswitch: (a) cross section, (b) top view.

It was assumed that the microswitch was made of polysilicon, while the traces and the shorting bar were made of gold. Material properties of polysilicon used in the computations were taken from Table 2.2, which lists the values corresponding to SUMMiT™V process (Pryputniewicz, 2002). The gold material properties, however, were obtained from Pro/ENGINEER material library (PTC, 2003a). Geometry of the microswitch was modeled using a computer aided design (CAD) tool, Pro/ENGINEER (PTC, 2003a). The computer model is shown in Fig. 3.12. It shows the cantilever-type microswitch attached to a substrate. Also on the substrate are two electrical traces that carry signals when the shorting bar on the cantilever closes the circuit, i.e., makes contact with the traces.

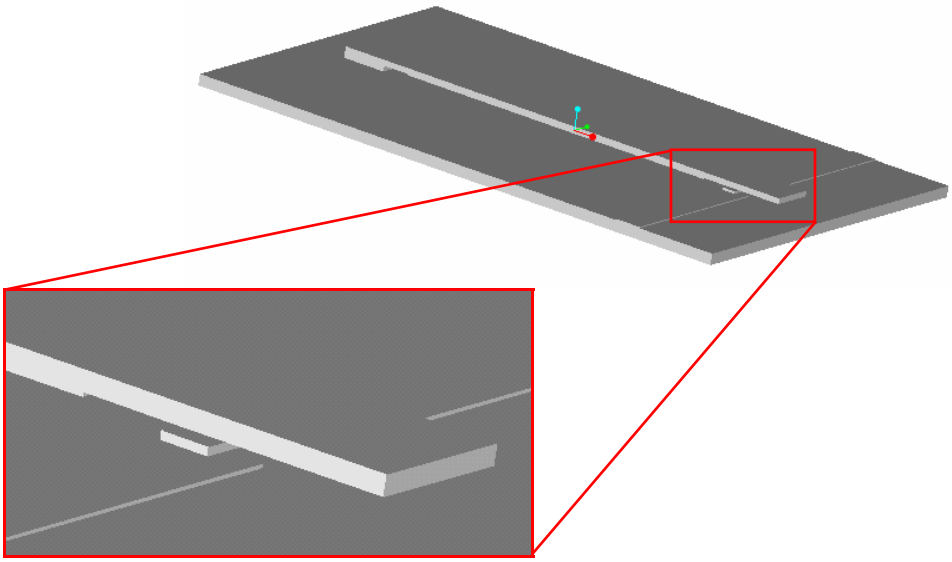

Fig. 3.12. CAD model of the cantilever-type microswitch.

3.2.1.2. Pro/MECHANICA algorithms

Pro/MECHANICA (PTC, 2003b) uses the *p* version of the finite element method to reduce discrimination error in an analysis. The *p* version refers to increasing the degree of the highest complete polynomial (*p*) within an element, by adding nodes to elements, degrees of freedom to nodes, or both, but without changing the number of elements used. This guarantees that a sequence of successively refined meshes will produce convergence (PTC, 2003c).

The *p* version represents the displacement within each element using high-order polynomials, as opposed to the linear and sometimes quadratic or cubic functions. A single *p*-element can, therefore, represent more complex state than a conventional finite element. The use of higher-order elements leads to an increase in the dimensions of the element matrices, thus requiring larger calculation capabilities. However, fewer higher-order elements are needed in order to obtain the same degree of accuracy, i.e., convergence.

A one-dimensional isoparametric element has the following shape functions N_1 and N_2 (PTC, 2003c)

$$N_1 = \frac{1-\xi}{2} \quad , \tag{3.44}$$

and

$$N_2 = \frac{1+\xi}{2} \quad . \tag{3.45}$$

where ξ is the local position along the element studied. A high-order one-dimensional hierarchical shape function is expressed as

$$N_i(\xi) = \phi_{i-1}(\xi) \quad , \tag{3.46}$$

for

$$i = 3, 4, 5, ..., p+1 \quad , \tag{3.47}$$

where

$$\phi_j(\xi) = \frac{1}{(2(2j-1))^{1/2}} (P_j(\xi) - P_{j-2}(\xi)) \quad . \tag{3.48}$$

In Eq. 3.48, the P_j represents the Legendre polynomials, which can be written as

$$P_0 = 1 \quad , \tag{3.49}$$

$$P_1 = \xi \quad , \tag{3.50}$$

$$P_2 = \frac{1}{2}(3\xi^2 - 1) \quad , \tag{3.51}$$

$$P_3 = \frac{1}{2}(5\xi^3 - 3\xi) \quad , \tag{3.52}$$

$$P_4 = \frac{1}{8}(35\xi^4 - 30\xi^2 + 3) \quad , \tag{3.53}$$

$$\vdots$$

$$(n+1)P_{n+1} = (2n+1)\xi P_n - nP_{n-1} \quad . \tag{3.54}$$

The basis functions N_1 and N_2 are the nodal shape, or external shape functions, while the shape functions N_i, i=3, 4, 5, … are the internal shape functions or the internal modes (Babuska and Szabo, 1991).

3.2.2. TAS analysis

The model of the RF microswitch considered in this thesis was also used for thermal analysis. This analysis facilitated finding temperature distributions within the microswitch, as well as finding the maximum temperature of the microswitch and its location. Knowledge of the heat affected zones allows for effective thermal management of the microswitch (Machate, et al., 2003).

3.2.2.1. TAS model

A model of a microswitch with the same geometry and material as the CAD model, described in Section 3.2.1.1, was considered in Thermal Analysis System (TAS) software, Fig. 3.13. As in Fig. 3.11, the model includes the cantilever, part of a wafer it is attached to, and signal traces.

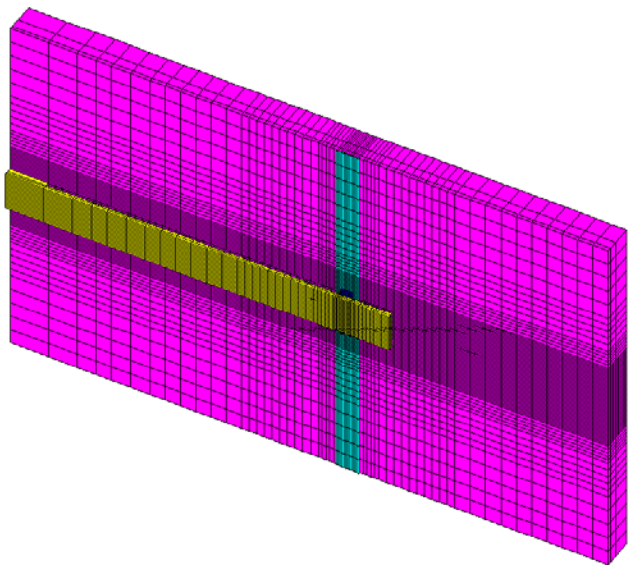

Fig. 3.13. TAS model of the cantilever-type microswitch.

3.2.2.2. TAS algorithms

Thermal Analysis System (TAS) is finite difference software that uses resistors in order to solve for the thermal distributions in a model (Rosato, 2002). In a three-dimensional model of a single element there might be as many as 28 resistors (Pryputniewicz, et al., 2002c). These resistors are derived from the equations for the three modes of heat transfer: convection, conduction and radiation.

The resistance due to convection is calculated according to the equation

$$R_c = \frac{1}{hA_c} \quad , \tag{3.55}$$

where h is a the convection heat transfer coefficient, A_c is the convective area associated with each surface node.

The conduction resistance, R_k, is calculated using equation

$$R_k = \frac{\Delta}{kA_k} \quad , \tag{3.56}$$

where Δ is the distance between the nodes, k is the thermal conductivity, A_k is the cross sectional area through which conductive heat transfer takes place associated with each internal node.

Finally, the resistance related to radiation is calculated from each node of the model to a single reference node according to the equation

$$R_r = \frac{1}{\varepsilon_s \sigma A_r F_s \left(T_1^2 + T_2^2 \right)\left(T_1 + T_2\right)} \quad , \tag{3.57}$$

where A_r is the radiation area associated with each surface node, σ is the Stefan-Boltzmann constant, F_s is the view factor, ε_s is the emissivity of the surface, and T_1 and

T_2 are the absolute temperatures of the two nodes to which the resistor is attached. As the TAS model is developed, more than one resistor may be associated with a given pair of nodes. To speed up the solution process, the multiple resistors can be combined into an equivalent resistance, providing that individual resistances are temperature and time independent, according to the equation

$$R = \left(\frac{1}{R_i} + \frac{1}{R_{i+1}} + \ldots + \frac{1}{R_{i+n}} \right)^{-1} \quad . \tag{3.58}$$

TAS software allows for assigning material properties to as many parts of model as necessary. It uses these properties, along with the assigned thermal conditions to give either a steady state or transient solution. The finite difference steady state solution is computed as (Pryputniewicz, et al., 2002c)

$$T_i = T_{i_{prev}} (1-d) + d \frac{\Sigma \left(\frac{T_{i+1}}{R_{i+1}} \right) + Q_i}{\Sigma \left(\frac{1}{R_{i+1}} \right)} \quad , \tag{3.59}$$

where T_i is newly calculated temperature of the i-th node, d is the damping coefficient with the default value of one, $T_{i_{prev}}$ is the temperature of the i-th node from previous iteration, T_{i+1} is the temperature of the neighboring node to which resistor R_{i+1} is connected, and Q_i is the total heat load on the i-th node. The transient solution is calculated as

$$T_i = \frac{\left[\Sigma \left(\frac{T_{i+1}}{R_{i+1}} \right) + Q_i \right] \Delta t}{\rho c_p V} + T_{i_{prev}} \quad , \tag{3.60}$$

where Δt is a time increment, and the denominator, $\rho c_p V$, is the thermal capacitance of the node.

3.3. Uncertainty analysis

An uncertainty analyses were performed in order to determine how good the results are (Pryputniewicz, 1993). More specifically, the uncertainty analysis relates to deformations of a simply supported-fixed cantilever that is the main component of the RF MEMS switch considered in this thesis.

The uncertainty analysis that was conducted in this thesis was performed based on the root-sum-square (RSS) approach (Pryputniewicz, 1993), which assumes a Gaussian distribution in the values of the uncertainty for the variables to be considered.

For multiple measurements of a single parameter, X, the total RSS uncertainty, δ_X, is defined as

$$\delta_X = \left(B^2 + {P_X}^2\right)^{1/2} \quad , \tag{3.61}$$

where B is the bias limit and P_X is the accuracy limit of the individual uncertainty components. The uncertainty results follow the Gaussian distribution of values, Fig. 3.14, where the $\overline{X}$ is a mean value of a variable and σ is the standard deviation of the occurrence of that variable (Coleman and Steele, 1989).

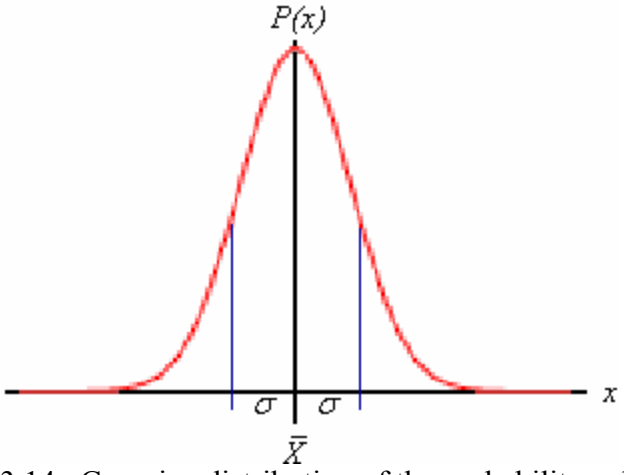

Fig. 3.14. Gaussian distribution of the probability values.

For the case of a result that is calculated from many individual variables, a *general* uncertainty *analysis* must be done using, e.g., the RSS approach. This is a special case of the uncertainty described in Eq. 3.61, where for each variable, X_i,

$$B_{X_i} = 0 \quad . \tag{3.62}$$

This reduces Eq. 3.61 to

$$\delta_{X_i} = P_{X_i} \quad . \tag{3.63}$$

In order to utilize Eq. 3.63, the general uncertainty analysis must begin by writing a phenomenological equation for the parameter X for which uncertainty is to be determined, based on its explicit equation (Pryputniewicz, 1993)

$$X = X\left(X_1, X_2, \ldots, X_n\right) \quad , \tag{3.64}$$

where X_1, X_2, ..., X_n, are independent parameters defining X. Using Eq. 3.64, the uncertainty of X is calculated using the RSS approach as

$$\delta_X = \left[\left(\frac{\partial X}{\partial X_1} \delta_{X_1} \right)^2 + \left(\frac{\partial X}{\partial X_2} \delta_{X_2} \right)^2 + \cdots + \left(\frac{\partial X}{\partial X_n} \delta_{X_n} \right)^2 \right]^{1/2} , \quad (3.65)$$

where the δ_{Xi} represents the uncertainties of the individual parameters X_i (Steward, 2003). Detailed calculations of the uncertainties are included in Appendix B and Appendix C.

3.4. RF circuit analysis

The RF MEMS switch considered in this thesis was a part of a series configuration of a simple two port RF circuit that included a transmission line and a ground, Fig. 3.15. Since the RF microswitch is in series configuration, either microstrip or coplanar waveguide (CPW) can be used as a transmission line.

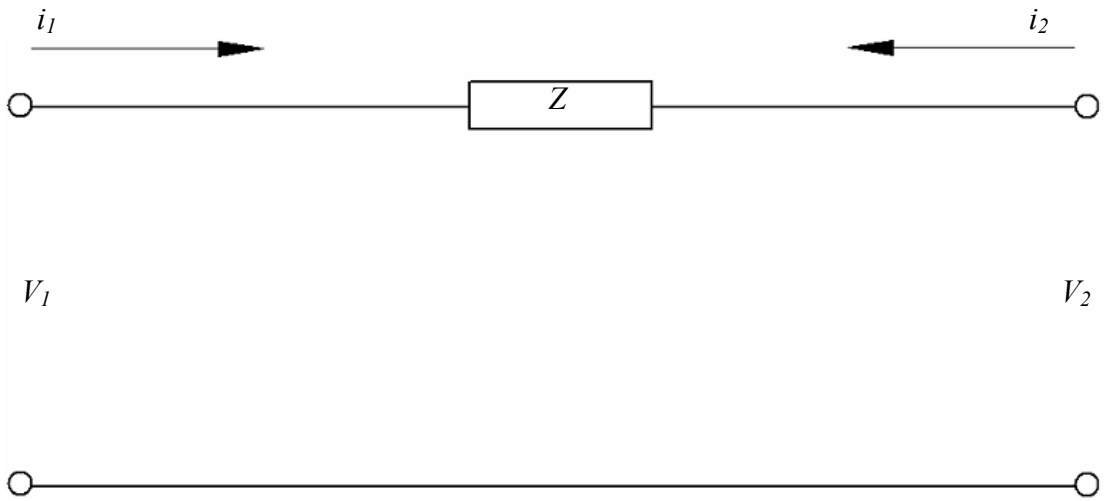

Fig. 3.15. Two port RF circuit in series configuration.

In a microstrip, the ground is located underneath the substrate, and its impedance is extremely sensitive to the substrate thickness. In general, it was observed that using microstrip transmission line produced lower losses then the CPW transmission line. The CPW, however, requires no vias through the substrate in order to ground the microswitch.

For a better understanding of the network an ABCD-matrix can be formed (Ludwig and Bretchko, 2000). This matrix relates the current and the voltage of the circuit. An ABCD-matrix of any two port network can be defined as

$$\begin{Bmatrix} V_1 \\ i_1 \end{Bmatrix} = \begin{bmatrix} A & B \\ C & D \end{bmatrix} \begin{Bmatrix} V_2 \\ -i_2 \end{Bmatrix} \quad , \tag{3.66}$$

where individual components of the matrix for a series configuration are

$$A = \left. \frac{V_1}{V_2} \right|_{i_2=0} = 1 \quad , \tag{3.67}$$

$$B = \left. \frac{V_1}{-i_2} \right|_{V_2=0} = Z \quad , \tag{3.68}$$

$$C = \left. \frac{i_1}{V_2} \right|_{i_2=0} = 0 \quad , \tag{3.69}$$

$$D = \left. \frac{i_1}{-i_2} \right|_{V_2=0} = 1 \quad . \tag{3.70}$$

In Eqs 3.66 to 3.70, V_1 and V_2 are the voltages in the RF circuit before and after the microswitch, respectively, i_1 and i_2 are the currents in the RF circuit before and after the microswitch, and Z is the impedance of the microswitch, Fig. 3.15.

The ABCD-matrix can then be converted to S-parameters. This new, equivalent representation of the circuit allows for better characterization of the electrical performance of the RF MEMS switch. The most important S-parameter is S_{21}. The S_{21} value calculated for an open microswitch provides information about the insertion loss of the microswitch, while the S_{21} value for closed microswitch provides isolation information. In order to calculate the two values of S_{21} both positions of the microswitch had to be modeled in a circuit.

In the open position of the RF MEMS switch the two ends of the shorting bar that overlap with the traces parallel to them build up capacitance, while the shorting bar itself carries inductance. Thus, the open microswitch position would have the impedance Z_{open}, Fig. 3.16.

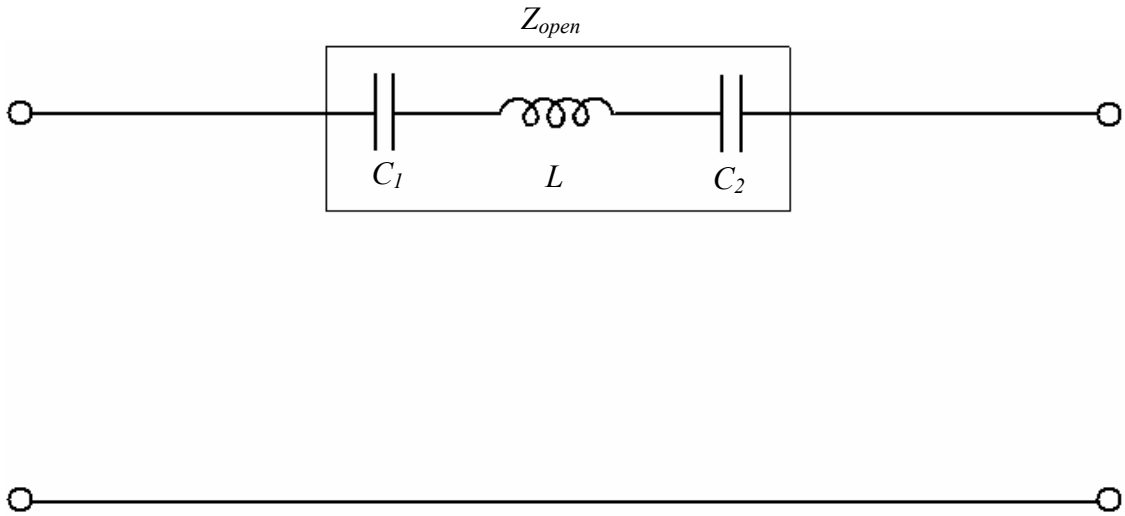

Fig. 3.16. Circuit model of the RF MEMS switch in open position.

The impedance Z_{open} can be calculated using the following equation

$$Z_{open} = \frac{2}{j\omega C} + j\omega L \quad . \tag{3.71}$$

In Eq. 3.71 ω is the signal frequency, j is the imaginary term equal to $\sqrt{-1}$, L is the inductance of the shorting bar, and C is the capacitance between the overlapping contacts. The capacitance can be computed as

$$C = \frac{\varepsilon_o \varepsilon_r A}{d} \quad , \tag{3.72}$$

where ε_o is the dielectric constant of air, ε_r is the relative permittivity of the material between electrodes, A is the overlapping area of the contacts, and d is the distance between the shorting bar and the trace. For the modeling purposes only the inductance of the shorting bar was taken into consideration. The inductance of a rectangular cross section straight strip of length L_s (in centimeters) can be calculated as (Grover, 1946)

$$L = 0.002 L_s \left[\log_e \frac{2L_s}{b_s + h_s} + \frac{1}{2} - \log_e w \right] \quad , \tag{3.73}$$

where L_s, b_s , h_s are length, width, and thickness of the shorting bar, respectively, and w is the geometric constant (Grover, 1946). The last term in Eq. 3.73 can be obtained from Table 3.2 for the given value of $\frac{h_s}{b_s}$. Solution of Eq. 3.73 yields inductance in μH.

The closed microswitch position would have impedance Z_{closed}, where the individual components include contact resistance at the shorting bar trace interfaces and the inductance of the shorting bar, Fig. 3.17. The Z_{closed} can be calculated as

$$Z_{closed} = 2R + j\omega L \quad , \tag{3.74}$$

where R is the electrical resistance and other parameters are as previously defined.

Table 3.2. Values of $\log_e e$ for self inductance calculations.

$\frac{h_s}{b_s}$	$\log_e w$	$\frac{h_s}{b_s}$	$\log_e w$
0	0	0.50	0.00211
0.025	0.00089	0.55	0.00203
0.05	0.00146	0.60	0.00197
0.10	0.00210	0.65	0.00192
0.15	0.00239	0.70	0.00187
0.20	0.00249	0.75	0.00184
0.25	0.00249	0.80	0.00181
0.30	0.00244	0.85	0.00179
0.35	0.00236	0.90	0.00178
0.40	0.00228	0.95	0.00177
0.45	0.00219	1.00	0.00177

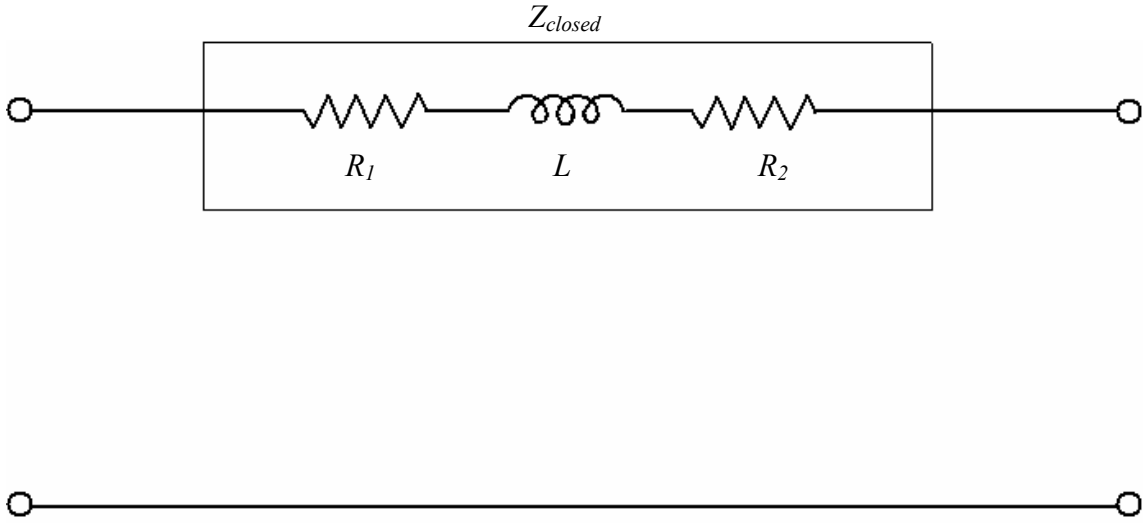

Fig. 3.17. Circuit model of the RF MEMS switch in closed position.

The computed impedance of the open and closed microswitch can then be used when solving for needed S-parameter. The S_{21} parameter can be expressed as (Wolff and Kaul, 1988)

$$S_{21} = \frac{2V_Z}{V_G} \quad , \tag{3.75}$$

where V_Z and V_G are the voltages in the complete circuit that includes the microswitch, Fig. 3.18. It was assumed that the transmission line had a Z_o impedance of 50 Ω on either side of the microswitch and Z was position dependent. Therefore the S_{21} parameter is

$$S_{21} = \frac{2Z_o}{2Z_o + Z} \quad . \tag{3.76}$$

Calculations of the electrical characteristics of the RF circuit are included in Appendix D.

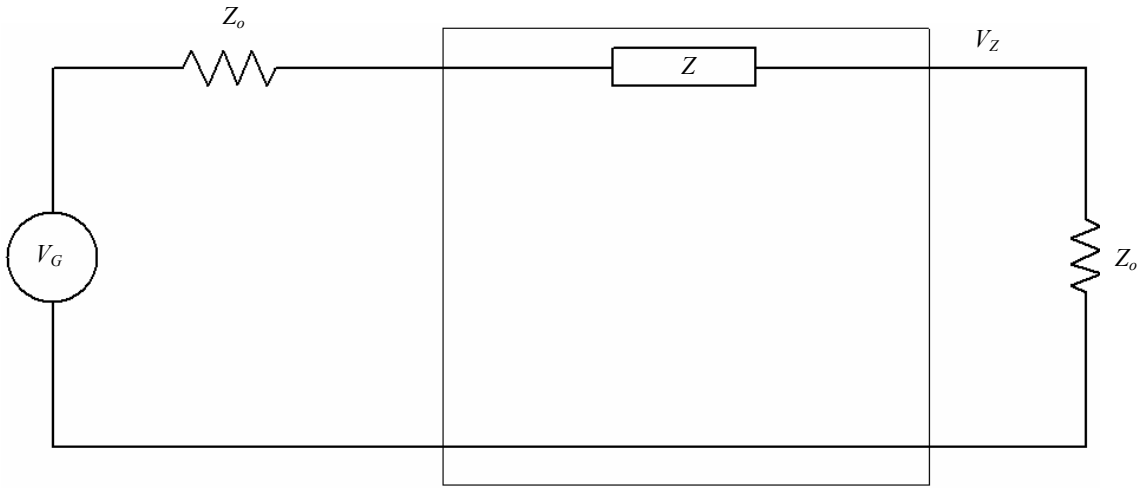

Fig. 3.18. Complete circuit based on RF MEMS switch.

3.5. Experimental methods

The samples of RF MEMS switches obtained by Worcester Polytechnic Institute's Center for Holographic Studies and Laser micro-mechaTronics (CHSLT) were fabricated by Cronos (2002). All the samples were not yet operational, because the sacrificial layer remaining on the substrate, after the Multi-User MEMS Processes (MUMPs) fabrication (Koester, et al., 2001), has not been removed, i.e., the microswitches were not released. The samples have also not been wire-bonded to make electrical connections. Therefore, no experimental analysis was performed on the operation of those microswitches.

However, experimental images were obtained using an optoelectronic laser interferometric microscope (OELIM) setup (Brown and Pryputniewicz, 1998; Brown, 1999; Pryputniewicz and Furlong, 2002, 2003; Pryputniewicz, et al., 2001d). This setup includes a Nikon microscope with a monochromatic light source and a high-speed, high-spatial-resolution digital camera, Fig. 3.19. The magnification of the microscope objective used to obtain the images was 30X, while its numerical aperture was 0.55.

For future experiments an OELIM system must be used. Basic configuration of the OELIM system is shown in Fig. 3.20. In this configuration, laser light is launched into a single mode optical fiber by means of a microscope objective (MO). Then, the single mode fiber is coupled into two fibers by means of a fiber optic directional coupler (DC). One of the optical fibers comprising the DC is used to illuminate the object, while the output from the other fiber provides reference against which the signals from the object are recorded. Both, the object and reference beams are combined by the interferometer (IT) and recorded by the system camera (CCD).

Fig. 3.19. OELIM setup.

Images recorded by the CCD camera are processed by the image-processing computer (IP) to determine the fringe-locus function, Ω, constant values of which define fringe loci on the surface of object under investigation (Pryputniewicz, 1995a, 1995b). The values of Ω relate to the system geometry and the unknown vector **L,** defining deformations, via the relationship (Pryputniewicz, 1995a):

$$\Omega = (\mathbf{K}_2 - \mathbf{K}_1) \bullet \mathbf{L} = \mathbf{K} \bullet \mathbf{L} \quad , \tag{3.77}$$

where **K** is the sensitivity vector defined in terms of vectors $\mathbf{K}_1$ and $\mathbf{K}_2$ identifying directions of illumination and observation, respectively, in the OELIM system, Fig. 3.20.

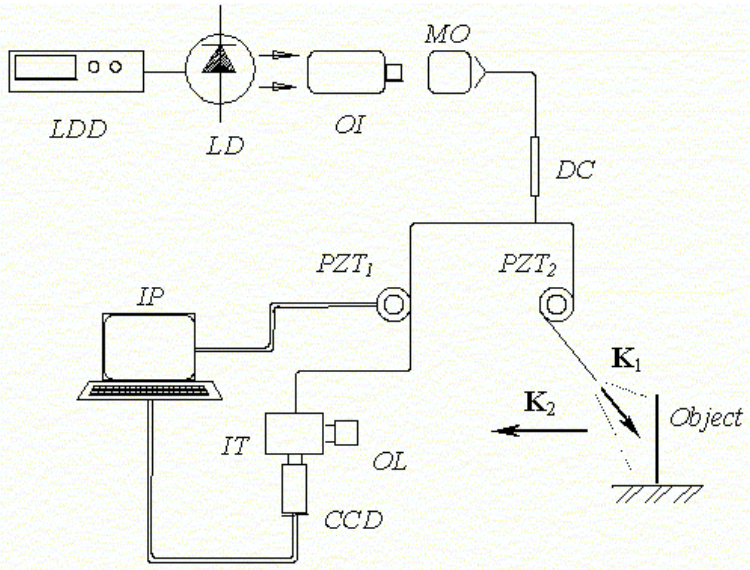

Fig. 3.20. Schematic of the OELIM configuration.

Quantitative determination of structural deformations due to the applied loads can be obtained, by solving a system of equations similar to Eq. 3.77, to yield (Pryputniewicz, 1995a)

$$\mathbf{L} = \left[\tilde{\mathbf{K}}^{\mathrm{T}}\tilde{\mathbf{K}}\right]^{-1}\left(\tilde{\mathbf{K}}^{\mathrm{T}}\Omega\right) \quad , \tag{3.78}$$

where $\tilde{\mathbf{K}}^{\mathrm{T}}$ represents the transpose of the matrix of the sensitivity vectors **K**.

Equation 3.78 indicates that deformations determined from interferograms are functions of **K** and Ω, which have spatial, i.e., (*x,y,z*), distributions over the field of interest on the object being investigated. Equation 3.78 can be represented by a phenomenological equation (Pryputniewicz, 1993) as

$$\mathbf{L} = \mathbf{L}(\mathbf{K}, \Omega) \quad , \tag{3.79}$$

based on which the RSS-type (where RSS represents *the square root of the sum of the squares*) uncertainty in **L**, i.e., $\delta\mathbf{L}$, can be determined to be

$$\delta\mathbf{L} = \left[\left(\frac{\partial \mathbf{L}}{\partial \mathbf{K}} \delta\mathbf{K} \right)^2 + \left(\frac{\partial \mathbf{L}}{\partial \Omega} \delta\Omega \right)^2 \right]^{1/2} \quad , \tag{3.80}$$

where $\partial\mathbf{L}/\partial\mathbf{K}$ and $\partial\mathbf{L}/\partial\Omega$ represent partial derivatives of $\mathbf{L}$ with respect to $\mathbf{K}$ and Ω, respectively, while $\delta\mathbf{K}$ and $\delta\Omega$ represent the uncertainties in $\mathbf{K}$ and Ω, respectively. It should be remembered that $\mathbf{K}$, $\mathbf{L}$, and Ω are functions of spatial coordinates (x,y,z), i.e., $\mathbf{K} = \mathbf{K}(x,y,z)$, $\mathbf{L} = \mathbf{L}(x,y,z)$, and $\boldsymbol{\Omega} = \boldsymbol{\Omega}(x,y,z)$, respectively, when performing partial differentiations. After evaluating, Eq. 3.80 indicates that $\delta\mathbf{L}$ is proportional to the product of the local value of $\mathbf{L}$ with the RSS value of the ratios of the uncertainties in $\mathbf{K}$ and Ω to their corresponding local values, i.e.,

$$\delta\mathbf{L} \propto \mathbf{L}\left[\left(\frac{\delta\mathbf{K}}{\mathbf{K}} \right)^2 + \left(\frac{\delta\Omega}{\Omega} \right)^2 \right]^{1/2} \quad . \tag{3.81}$$

For typical geometries of the OEH systems, based on which the OELIM methodology was developed, used in recording of interferograms, the values of $\delta\mathbf{K}/\mathbf{K}$ are less than 0.01. However, for small deformations, the typical values of $\delta\Omega/\Omega$ are about one order of magnitude greater than the values for $\delta\mathbf{K}/\mathbf{K}$ (Pryputniewicz, 1981). Therefore, the accuracy with which the fringe orders are determined influences the accuracy in the overall determination of deformations (Pryputniewicz, 1981). To minimize this influence, a number of algorithms for determination of Ω were developed (Pryputniewicz, 1990). Some of these algorithms require multiple recordings of each of the two states, in the case of double-exposure method, of the object being investigated with introduction of a discrete phase step between the recordings.

For example, the intensity patterns of the first and the second exposures, $I_n(x,y)$ and $I_n^{'}(x,y)$, respectively, in the double-exposure sequence can be represented by the following equations:

$$I_n(x,y) = I_o(x,y) + I_r(x,y) + 2\left[I_o(x,y)I_r(x,y)\right]^{1/2} \cos\left\{\left[\varphi_o(x,y) - \varphi_r(x,y)\right] + \theta_n\right\} \tag{3.82}$$

and

$$I_n^{'}(x,y) = I_o(x,y) + I_r(x,y) + 2\left[I_o(x,y)I_r(x,y)\right]^{1/2} \cos\left\{\left[\varphi_o(x,y) - \varphi_r(x,y)\right] + \theta_n + \Omega(x,y)\right\} , \tag{3.83}$$

where I_o and I_r denote the object and reference beam irradiances, respectively, with (x,y) denoting spatial coordinates, φ_o denotes random phase of the light reflected from the object, φ_r denotes the phase of the reference beam, θ_n denotes the applied n-th phase step, and Ω is the fringe-locus function relating to the deformations the object incurred between the first and the second exposures; Ω is what we need to determine. When Ω is known, it is used in Eq. 3.78 to find **L**.

In the case of 5-phase-steps algorithm with $\theta_n = 0, \pi/2, \pi, 3\pi/2$, and 2π, the distribution of the values of Ω can be determined using

$$\Omega(x,y) = \tan^{-1}\left\{\frac{2\left[I_2(x,y) - I_4(x,y)\right]}{2I_3(x,y) - I_1(x,y) - I_5(x,y)}\right\} . \tag{3.84}$$

Results produced by Eq. 3.84 depend on the capabilities of the illumination, imaging, and processing subsystems of the OEH system. Developments in laser, fiber

optic, CCD camera, and computer technologies have led to advances in the OEH metrology; in the past, these advances almost paralleled the advances in the image recording media (Pryputniewicz, 1995b). A fiber optic based OEH system, incorporating these developments, is able to measure static and dynamic deformations of objects subjected to a variety of boundary, initial, and leading (BIL) conditions, this system is also able to measure absolute shape of the objects using multiple-wavelength optical contouring (Furlong, 1999).

In response to the needs of the emerging MEMS technology, an optoelectronic laser interferometric microscope (OELIM) system for studies of objects with micron size features was developed (Brown, 1999; Brown and Pryputniewicz, 1998). In the OELIM system, Fig. 3.21, the light beam produced by the laser is directed into an acousto-optic modulator (AOM) and then into a single mode optical fiber. The output of the fiber is collimated by the collimating illumination lens subsystem (C). The resulting light field is then divided into reference and object beams by the beam splitter (BS). The reference beam is directed towards a PZT actuated mirror (M) and back to the beam splitter. The object beam is directed towards the MEMS under study and is reflected back to the beam splitter. The two beams recombine at the BS and are imaged by the long working distance microscope objective (L) onto the sensing element of the CCD camera, which records the resulting interference patterns. These patterns are transferred to the system computer for subsequent quantitative processing.

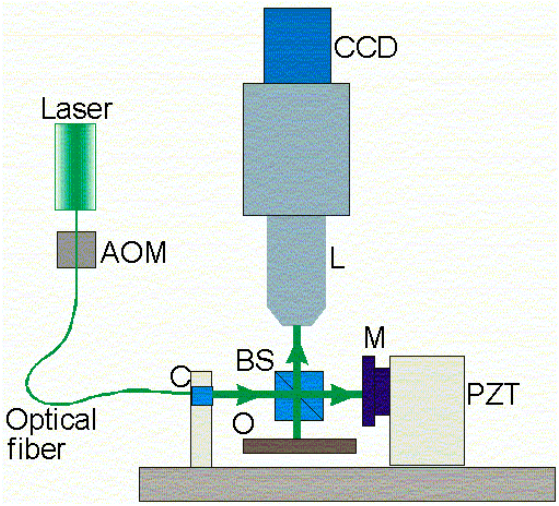

Fig. 3.21. Optical configuration of the OELIM setup.

Using the system shown in Fig. 3.21, issues relating to the sensitivity, accuracy, and precision, associated with application of the algorithm defined by Eq. 3.84 were studied while evaluating the effects that the use of high-spatial and high-digital resolution cameras would have on the results produced (Furlong, et al., 2002). This study is closely coupled with the development of fiber optic couplers and subsystems for efficient beam delivery (Pryputniewicz and Furlong, 2003).

4. RESULTS AND DISCUSSION

The ACES methodology allowed for obtaining well correlated results. Analytical and computational analyses provided solutions which were in agreement with each other, leading us to believe that the microswitch characterization was consistent with currently used practices.

4.1. Analytical results

The RF MEMS contact switch deformations and temperature distributions were calculated according to the fundamental governing equations. Both mechanical bending and the heat transfer analyses produced analytical and computational results indicating deformation and temperature distributions within the RF MEMS switch considered in this thesis.

4.1.1. Deformations

Based on the principals of structural mechanics, the cantilever deformations due to the electrostatic force generated between the electrodes were computed. The magnitude of the electrostatic force required to close the contact gap of 1 μm was 6.44 μN. Deformations of the cantilever at the instant of contact gap closure are shown in Fig. 4.1. The slope for the full length of the cantilever, at the instant of the contact gap closure, is shown in Fig. 4.2. The force required to close the gap between the contacts is

due to the actuation voltage. The gap closing force of 6.44 μN is generated by the actuation voltage of 57 V.

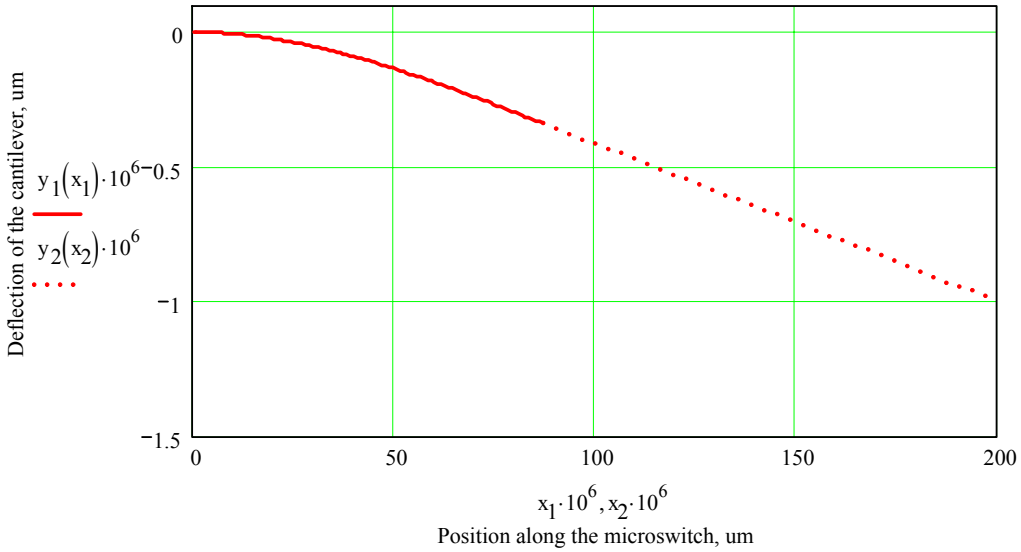

Fig. 4.1. Cantilever deformations as a function of position along the microswitch, at the instant of the contact gap closure, for the electrostatic force of 6.44 μN.

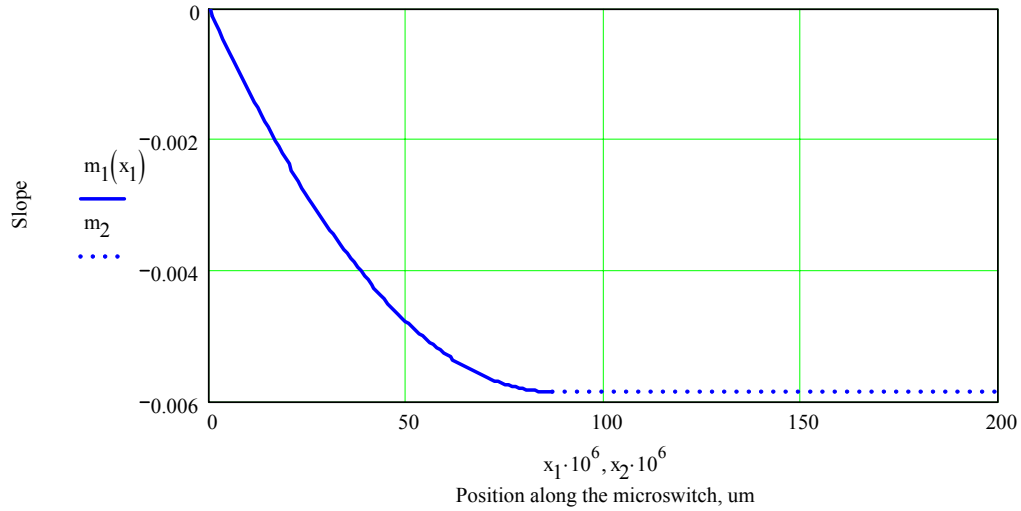

Fig. 4.2. Slope as a function of position along the microswitch, at the instant of the contact gap closure.

When the contact gap is closed, the cantilever is fixed at one end and simply supported at the other, i.e., the contact, end. Thus, computational analysis was also done for a fixed – simply supported system, with the contact end 1 μm lower than the fixed end. The deformation and slope results for this more appropriate configuration are shown in Figs 4.3 and 4.4.

To assure quality electrical interface the electrostatic force must be increased beyond the force necessary to close the contact gap. As the force increases, the cantilever deformations also increase. More bending occurs as the force increases beyond the nominal force required to simply close the contact gap. Cantilever deformations due to the applied force ranging from F to $4F$ are shown in Fig. 4.5.

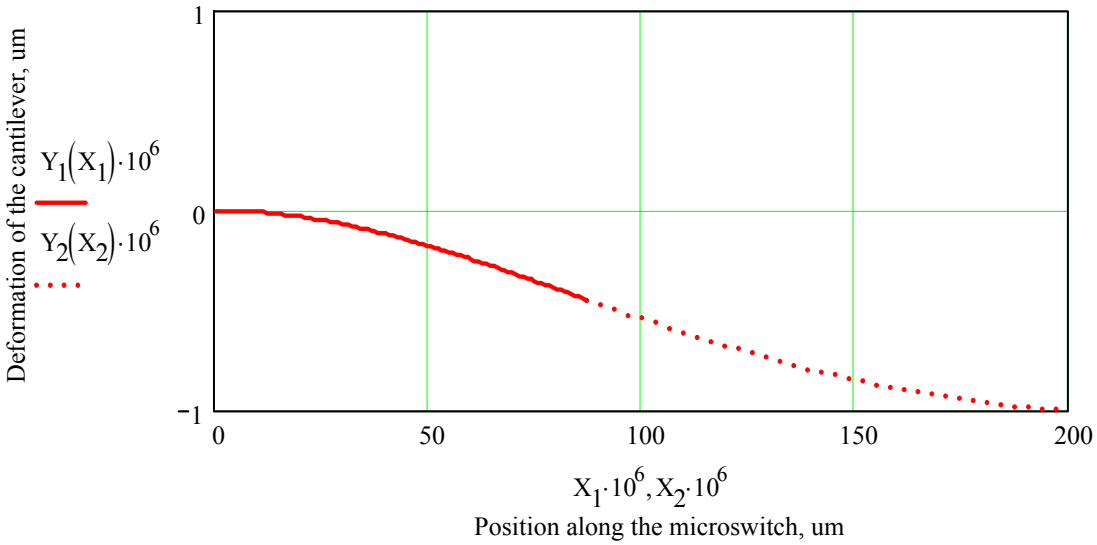

Fig. 4.3. Cantilever deformations as a function of position along the microswitch, at the instant of the gap closure, including positional differences between the fixed and contact ends of the cantilever, for the electrostatic force of 6.44 μN.

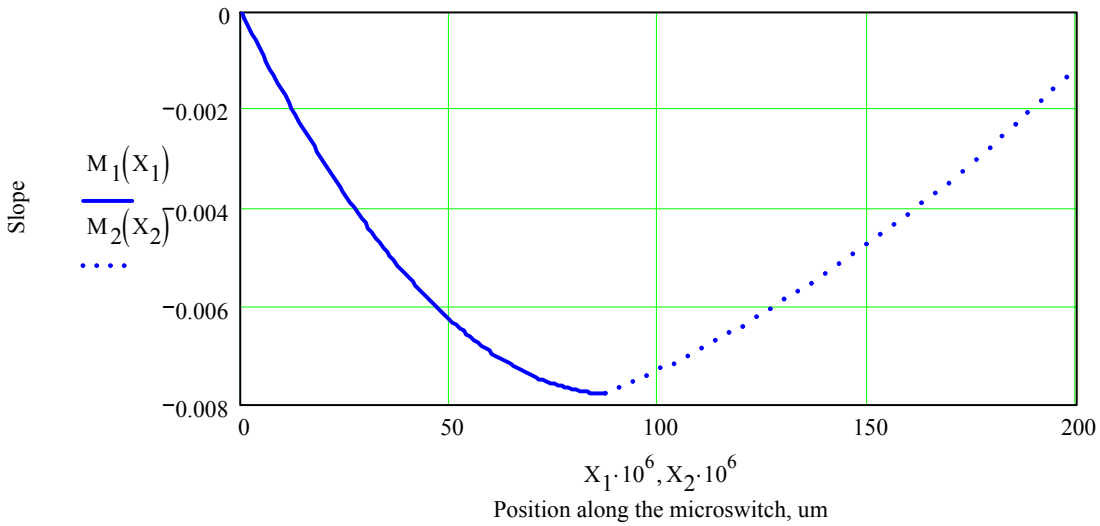

Fig. 4.4. Slope as a function of position along the microswitch, at the instant of the contact gap closure, including positional differences between the fixed and contact ends of the cantilever.

Finally, the slip force, F_S, is considered in this thesis. The slip, or friction, force was calculated for a known range of coefficients of friction and four different values of the normal forces used in the studies of deformations discussed in Section 3.1.1.1. The results obtained from the slip force calculations are shown in Fig. 4.6.

The results shown in Fig. 4.6 correlate well with the assumption made about the slip force relationship with the coefficient of friction and the force normal to the slip, Section 3.1.1.1. The slip force increases greatly as the coefficient of friction and the normal force increase. Results of analysis of the cantilever deformations are included in Appendix A.

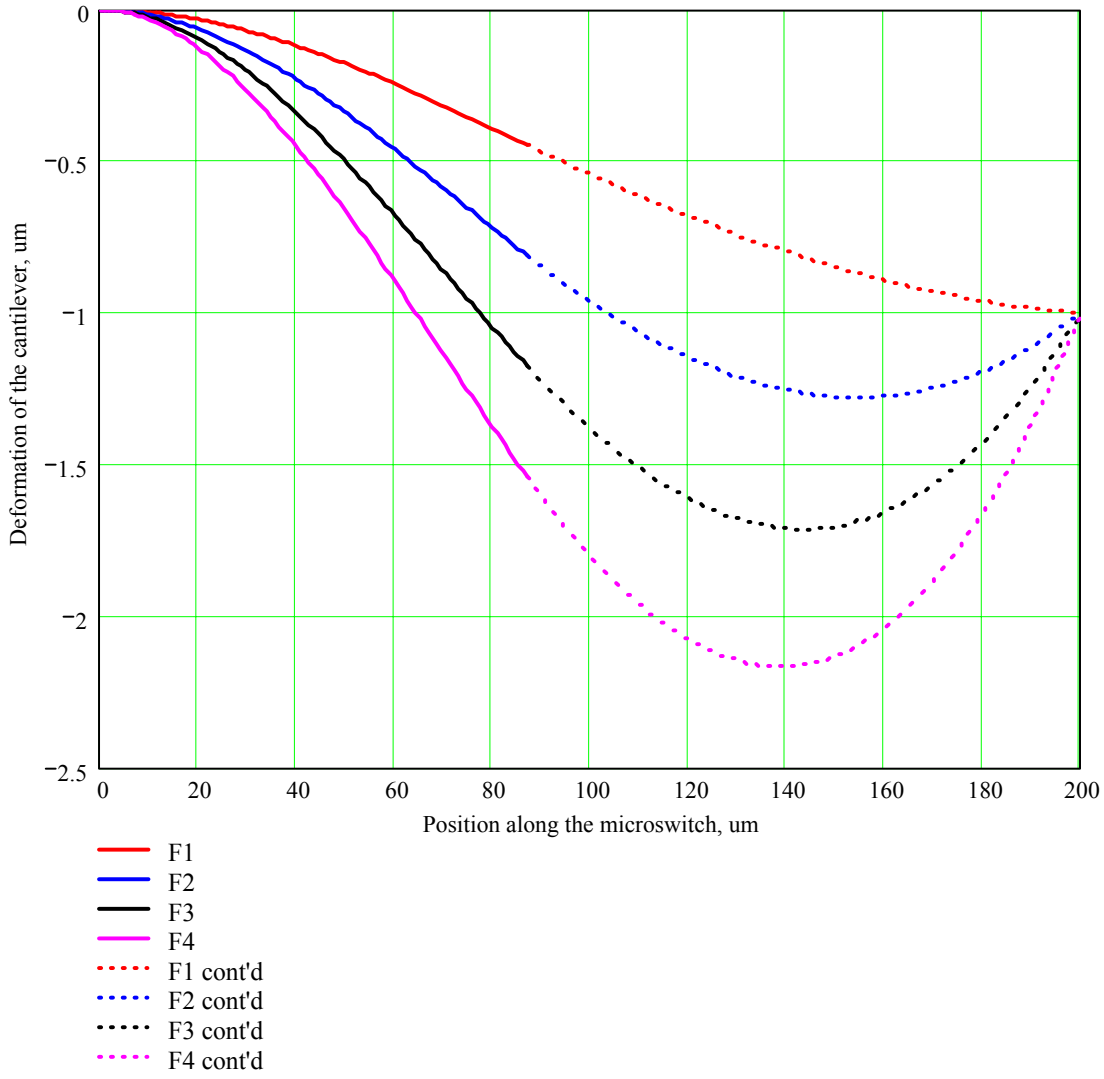

Fig. 4.5. Cantilever deformations as a function of position along the microswitch, where F1 is the nominal force value, F2 is twice that value, F3 is three times that value, and F4 is four times the nominal force value.

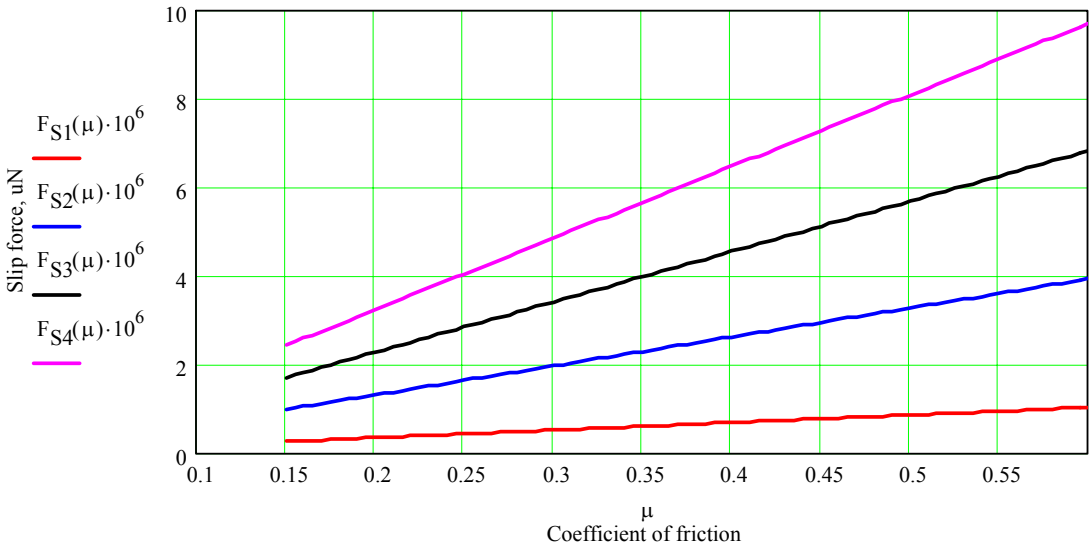

Fig. 4.6. Slip force as a function of coefficient of friction and normal force for F1, F2, F3 and F4.

4.1.2. Temperature

Making use of the voltage-temperature relation based on Weidemann-Franz law Section 3.1.3, it was found that the maximum temperature that the microswitch reaches is 740ºC. These data were compared to the TAS results, which showed maximum switch temperature of 716ºC. The relative correlation of the computational and analytical results obtained was better than 2.5%. From the preformed uncertainty analysis it is apparent that the result is very accurate considering that the overall uncertainty of the analytical solution obtained was over 13%. Complete calculations and results can be found in Appendix B.

4.2. Computational results

The computational results were obtained using Pro/MECHANICA and TAS softwares. Pro/MECHANICA software was used as a finite element software in order to compute the deformations of the RF MEMS switch under the electrostatic loading, while TAS software was used to find a steady state temperature distributions throughout the microswitch. Data obtained from the computational models described in Section 3.2 correlated well with the analytical results obtained using algorithms described in Section 3.1.

4.2.1. Deformations

Static deformations were calculated after the CAD microswitch model was assigned boundary and loading conditions. The distributed electrostatic force in this analysis was equal in magnitude to the concentrated force used in analytical considerations. In the Pro/MECHANICA (PTC, 2003b) simulation, the force was evenly distributed within the overlap area of the electrodes of the microswitch. Figure 4.7 displays the final shape of the cantilever due to the electrostatic load with the maximum deformation of 1 μm at the contacts. The deformations shown in Fig. 4.7 (in mm scale), correlate very closely with the analytically obtained deformations.

The Pro/MECHANICA simulation resulted in a maximum beam deformation of 1.02 μm, while the calculations were based on 1 μm gap size. Taking into consideration the uncertainty in the cantilever deformations, which is about 24% at the simply-

supported end of the cantilever, the two solutions are well within the uncertainty limits; the analytical and computational results are within 2% of each other.

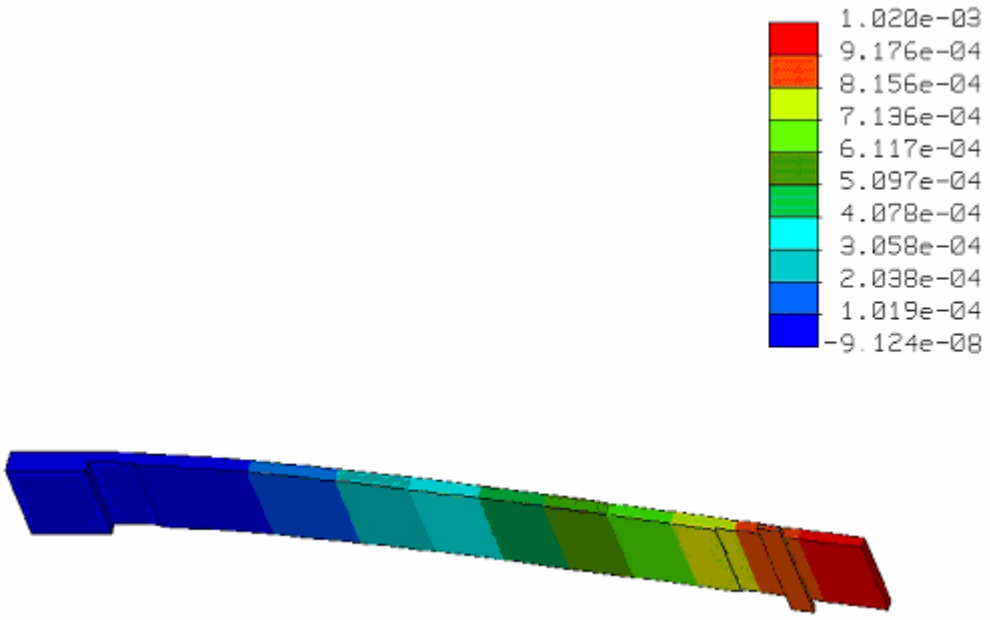

Fig. 4.7. Cantilever deformations (in mm) based on Pro/MECHANICA analysis.

4.2.2. Temperature

TAS software was used to simulate the temperature distributions within the RF MEMS switch. In order to find a steady state temperature profile of the microswitch the CAD model was transferred to TAS and appropriate boundary conditions were applied. The model was assigned appropriate material properties and the source of energy. The heat source was based on the electrical current of 300 mA and the contact resistance, set at 1 Ω, based on the information obtained from the Motorola, Inc.

The TAS model includes electrical current conduction, as well as free convection and radiation. The overall temperature increase due to Joule heating, excluding convective and radiative effects, was computed to be nearly 896ºC, as shown in Fig. 4.8, for the full microswitch temperature profile. The detail view of the heat affected zone is shown in Fig. 4.9. This heat affected zone is the area of the electrical contacts between the traces and the shorting bar.

It was found that the temperature distribution in the microswitch varies as the natural convection and radiation are included in the TAS model. Figure 4.10 shows the overall temperature distribution, including convective and radiative effects, indicating maximum temperature of about 717ºC, which is substantially lower than that shown in Fig. 4.8.

The greatest temperature gradient is throughout the cantilever affecting the shorting bar and the contact end of the cantilever. This is caused by the resistance between the contacts. Figure 4.11 shows in more detail the cantilever beam and the shorting bar.

Since resistance between the contacts has a great effect on temperature profile of the RF MEMS switch, the detail view of the temperature distribution at the contact area is shown in Fig. 4.12. The two sides of the shorting bar that make direct contact with the two ends of the traces are clearly at the temperature of about 717ºC, which is the highest for this case.

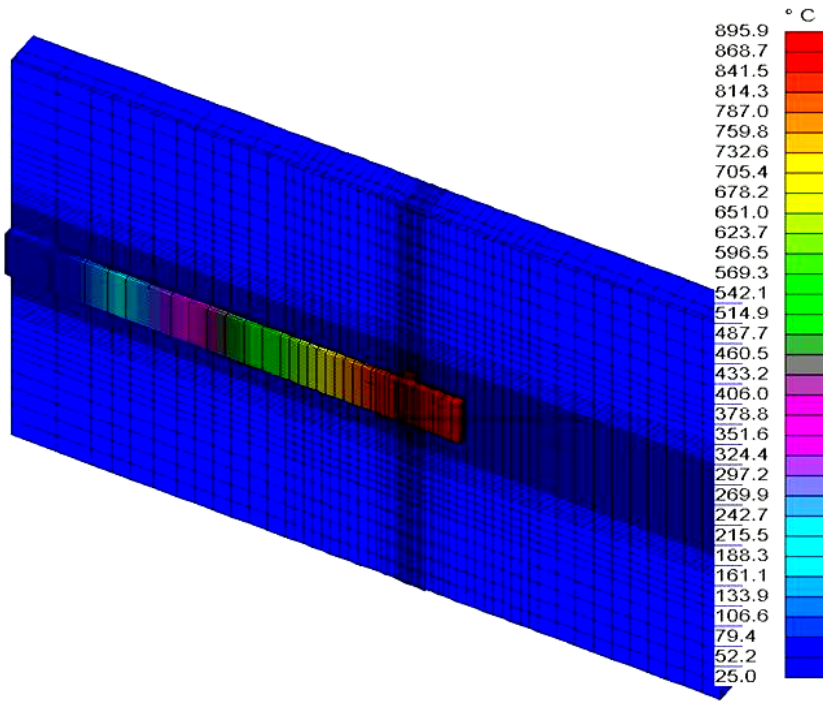

Fig. 4.8. Overall RF MEMS switch temperature distribution excluding convection and radiation.

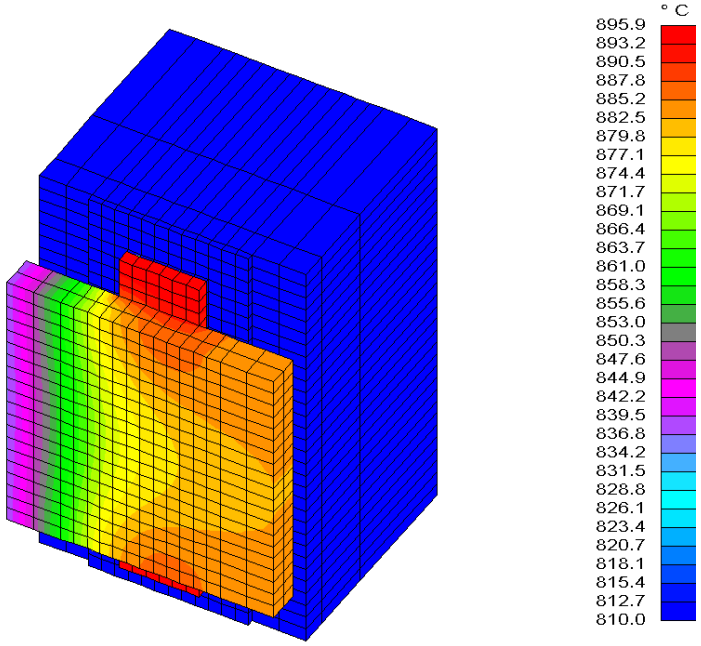

Fig. 4.9. Detail of the contact temperature distribution excluding convection and radiation.

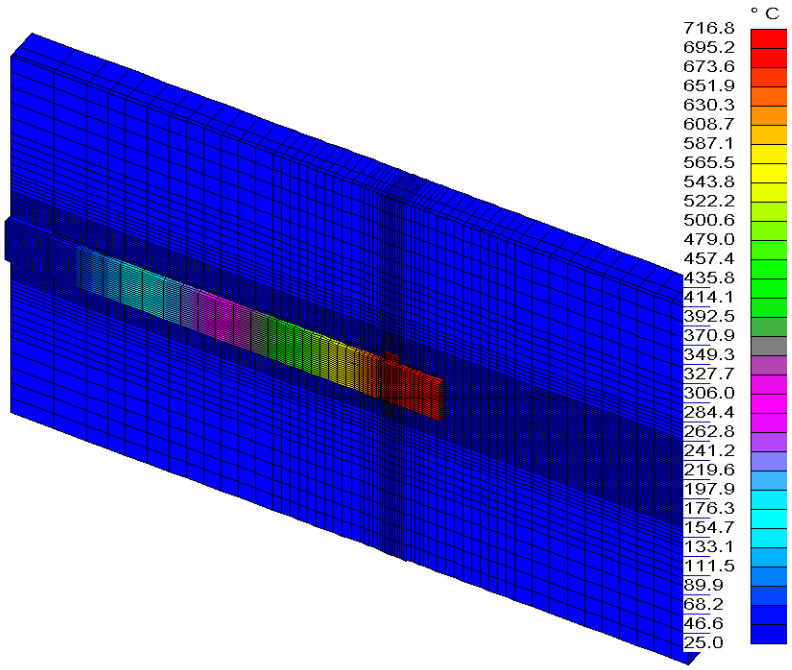

Fig. 4.10. Overall RF MEMS switch temperature distribution including convection and radiation.

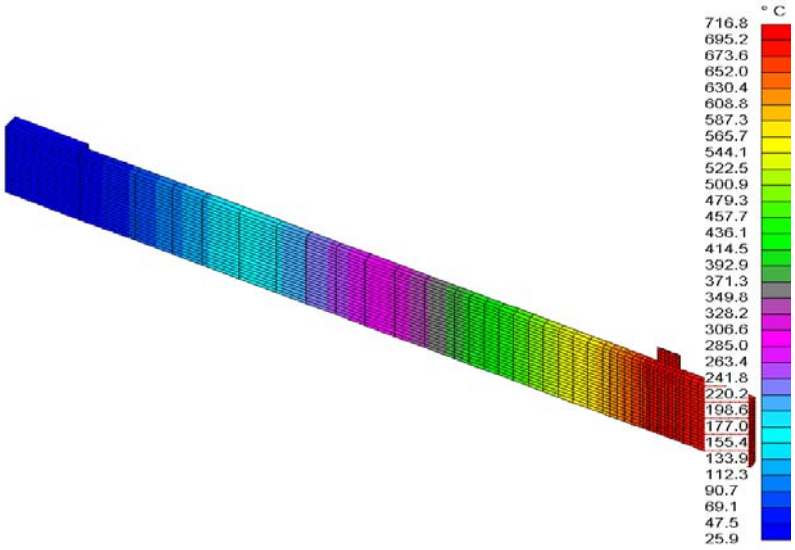

Fig. 4.11. Detail of the cantilever and shorting bar temperature distribution including convection and radiation.

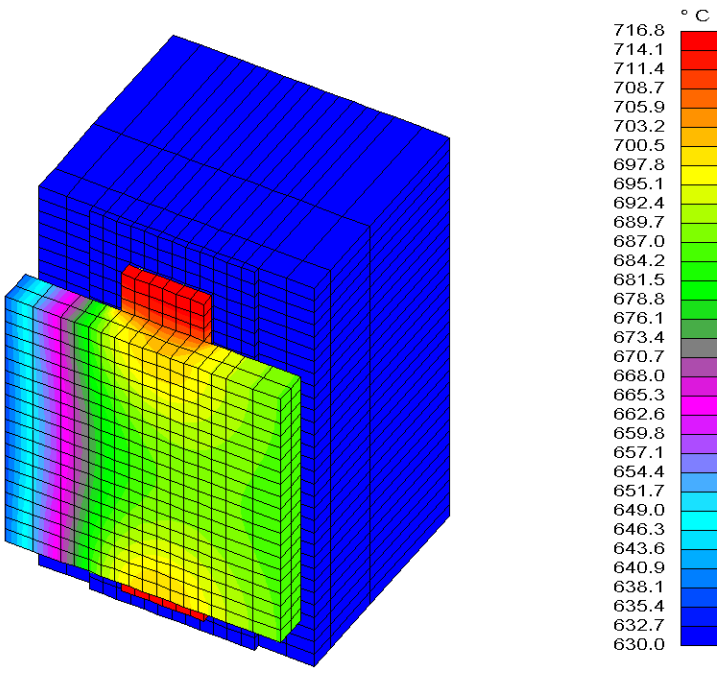

Fig. 4.12. Detail of the contact temperature distribution including convection and radiation.

Figure 4.13 shows that temperature of contact areas ranges from 680 ºC to 717 ºC. The edges of the contacts are hotter, while the area between them is at lower temperature. This is due to heat conducted away by the cantilever.

The same thermal characteristics are shown in the shorting bar temperature distribution, Fig. 4.14. The two edges of the shorting bar experience greater heating then the middle of the shorting bar. This, once again, is due to heat removal by conduction through the cantilever.

The substrate underneath the heat affected zones seems to be only slightly affected by the Joule heat, Fig. 4.15. In the case displayed, the substrate experienced a temperature raise from 25 ºC to 60 ºC. The relatively low temperature raise in the traces is attributed to good heat conduction through the whole substrate.

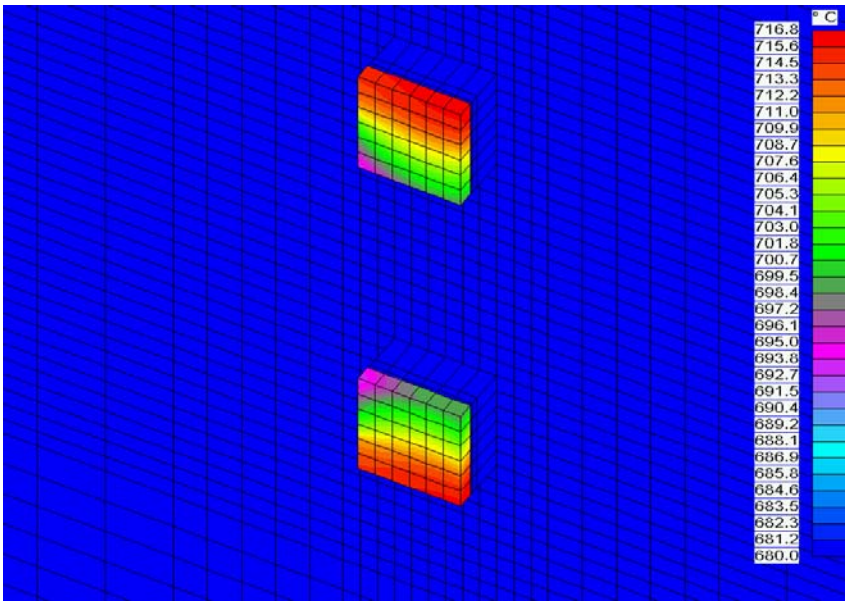

Fig. 4.13. Detail of the temperature distribution within the Joule heat affected zones of the shorting bar at the contact areas including convection and radiation.

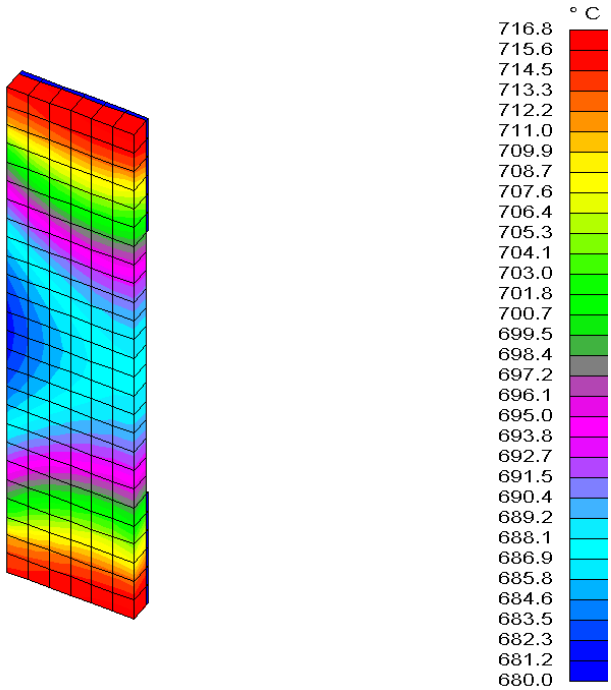

Fig. 4.14. Detail of the shorting bar temperature distribution including convection and radiation.

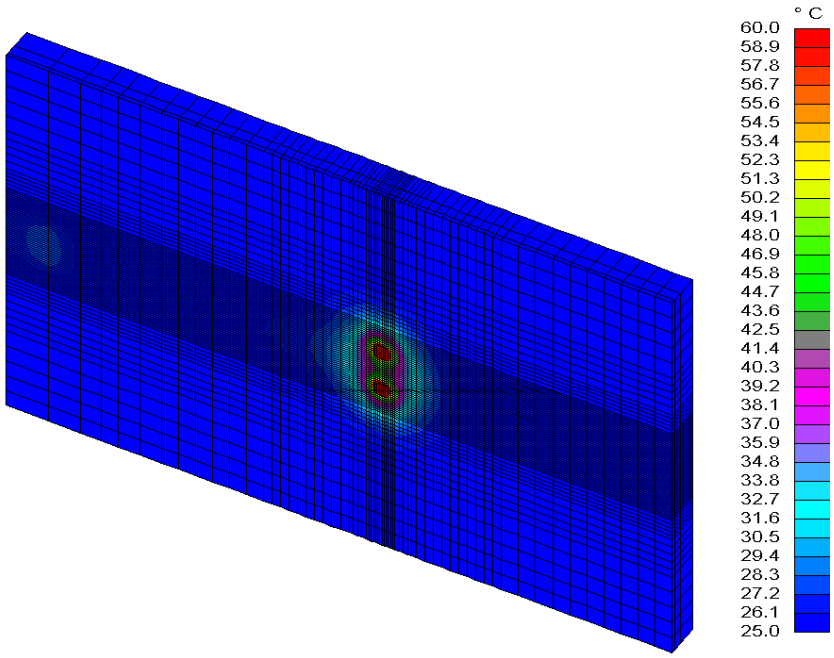

Fig. 4.15. Substrate temperature distribution including convection and radiation.

Due to high temperatures, based on TAS analysis of the microswitch both with and without convection and radiation, another analysis was performed. A thermal analysis was done on the RF MEMS switch, but the contact resistance was reduced by a factor of two, which is feasible because of new fabrication processes that are currently being developed. The 50% decrease in resistance accounted for a drastic drop in maximum temperature of the switch. With this lower resistance, the microswitch reaches the maximum temperature of about 409ºC, Fig. 4.16. This is a 40% temperature reduction, which is very desirable and needed in order to increase reliability of the microswitch.

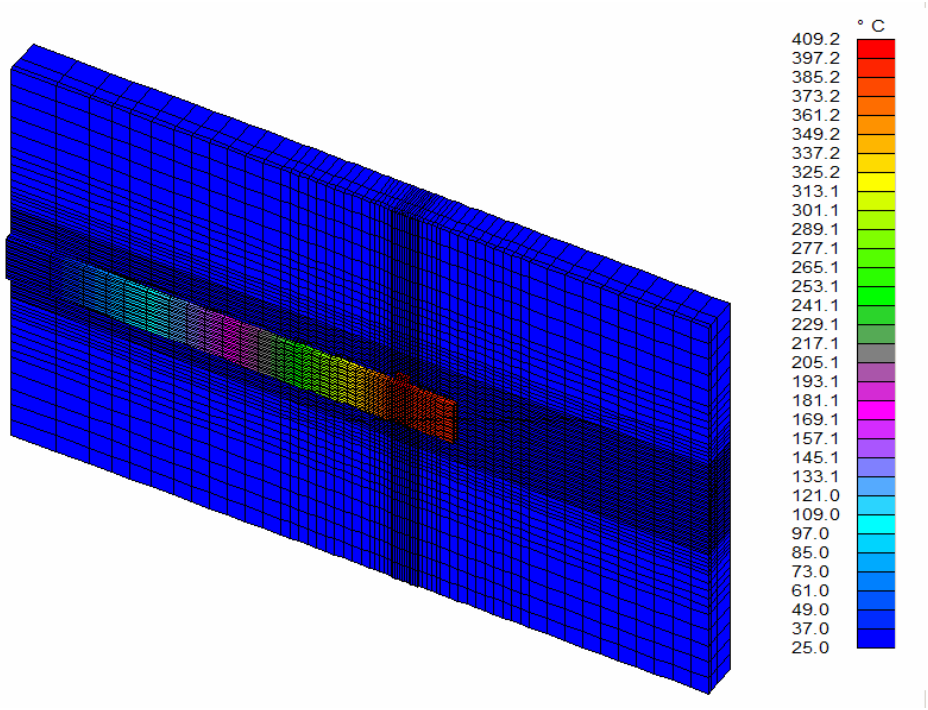

Fig. 4.16. Overall RF MEMS switch temperature distribution including convection and radiation, using a 50% lower contact resistance.

4.3. Uncertainty analysis

In the preliminary uncertainty calculations the uncertainty in the cantilever width was set to half of the least significant digit $\left(\frac{1}{2}LSD\right)$ of its nominal value, while the uncertainty in the cantilever thickness was assumed to be 5% of its nominal value. The uncertainties in various lengths were set at 2 μm due to fabrication tolerances, the uncertainty in the position along the cantilever was defined at 0.25 μm because of current measurement practices, and the uncertainty in modulus of elasticity was fixed at currently achievable measurement accuracy of 5 GPa (Pryputniewicz, 2002).

The overall uncertainty was calculated as a function of position along the cantilever. As in the deformation calculations, the cantilever was divided into two sections: section-1 and section-2. The results obtained for section-1 are shown in Figs 4.17 to 4.20. Similar uncertainty calculations were performed for section-2, with the results illustrated by Figs 4.21 to 4.24. The figures show the overall uncertainty of the maximum deformation of the cantilever as 22%. This value of overall uncertainty in the maximum deformation of the cantilever is unacceptable for application purposes and must be reduced.

The overall uncertainty can be controlled by controlling the individual uncertainties of the parameters defining microswitch geometry and material properties, as well as fabrication processes. The reduction of the percent overall uncertainty can not be done arbitrarily, but should be based on an orderly uncertainty analysis (Pryputniewicz, 1993). Therefore, the values for the individual uncertainties were adjusted according to appropriate values allowed by fabrication processes. Further uncertainty analysis indicated that the largest individual contributor to the percent overall uncertainty in the maximum deformation of the cantilever is the uncertainty in the cantilever thickness. Reducing the uncertainty in thickness to 1% of its nominal value lowers the overall uncertainty in the maximum deformation of the cantilever to 11%. However, even when the uncertainty in thickness is equal to 0.025 μm, it still remains the greatest contributor to the overall uncertainty in maximum deformation of the cantilever. Assuming an uncertainty in the cantilever thickness of 1% of the nominal value is becoming a practice in MEMS manufacturing, but it greatly affects the fabrication cost.

Detailed calculations of the overall uncertainty in the deformations of the cantilever can be found in Appendix C.

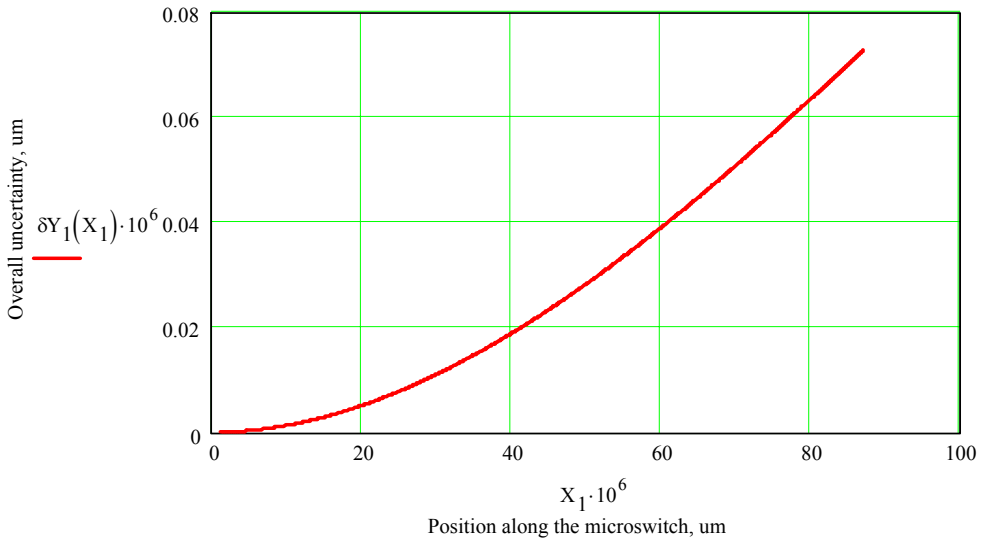

Fig. 4.17. Overall uncertainty in deformations of section-1 of the cantilever as a function of position along the microswitch.

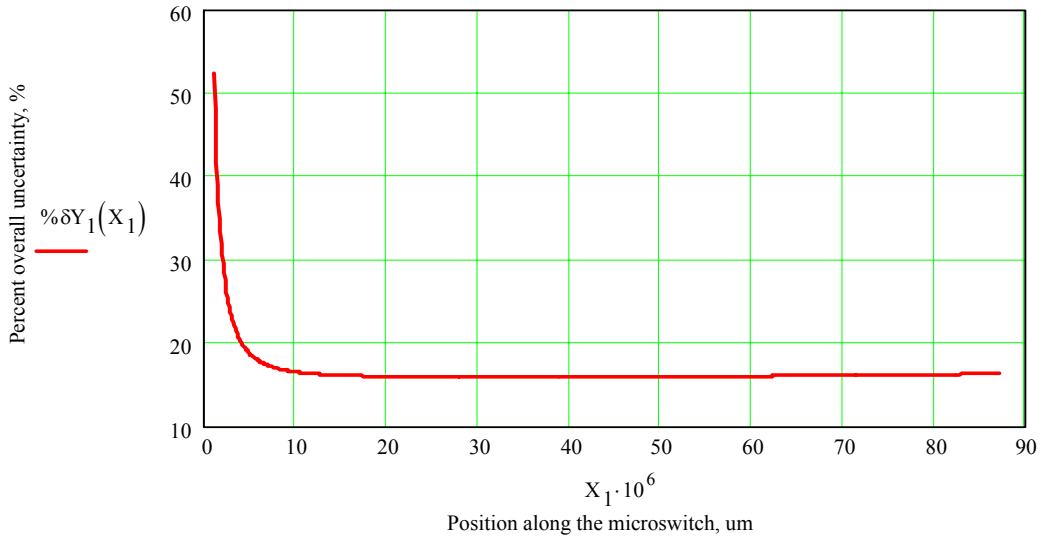

Fig. 4.18. Percent overall uncertainty in deformations of section-1 of the cantilever as a function of position along the microswitch.

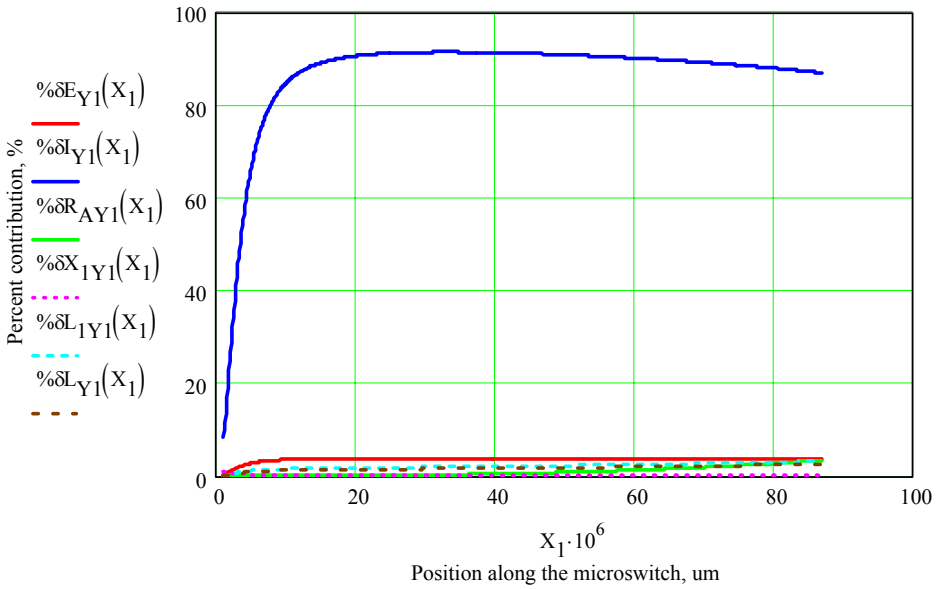

Fig. 4.19. Percent contributions of uncertainties in individual parameters to the overall uncertainty in deformations of section-1 of the cantilever as a function of position along the microswitch on a lin-lin scale.

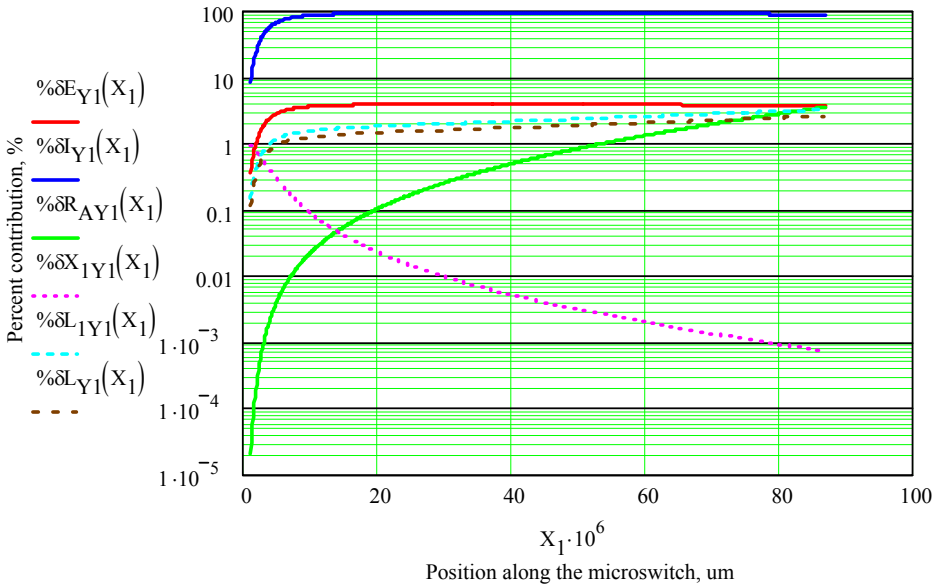

Fig. 4.20. Percent contributions of uncertainties in individual parameters to the overall uncertainty in deformations of section-1 of the cantilever as a function of position along the microswitch on a lin-log scale.

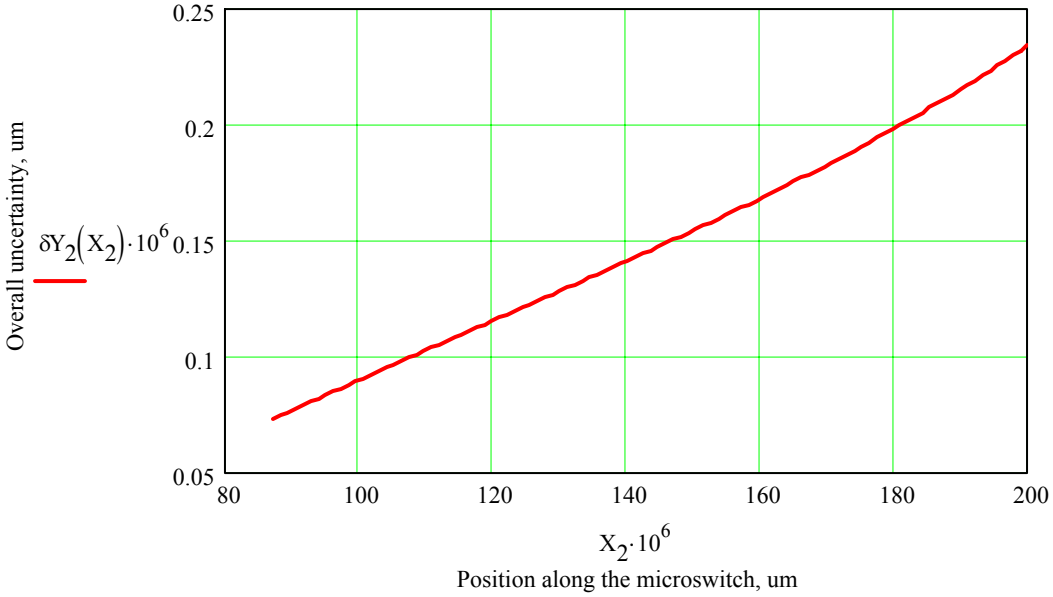

Fig. 4.21. Overall uncertainty in deformations of section-2 of the cantilever as a function of position along the microswitch.

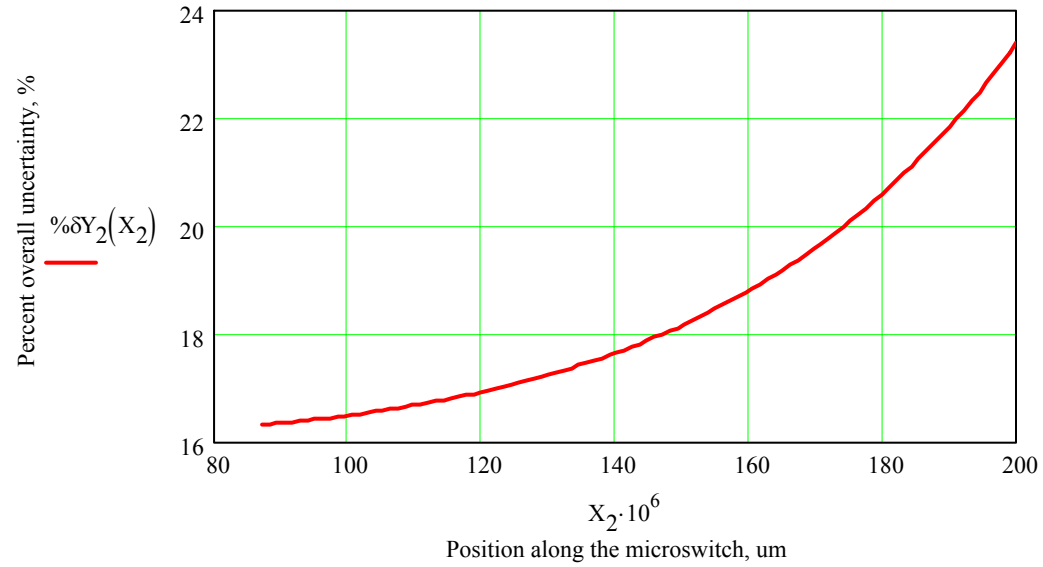

Fig. 4.22. Percent overall uncertainty in deformations of section-2 of the cantilever as a function of position along the microswitch.

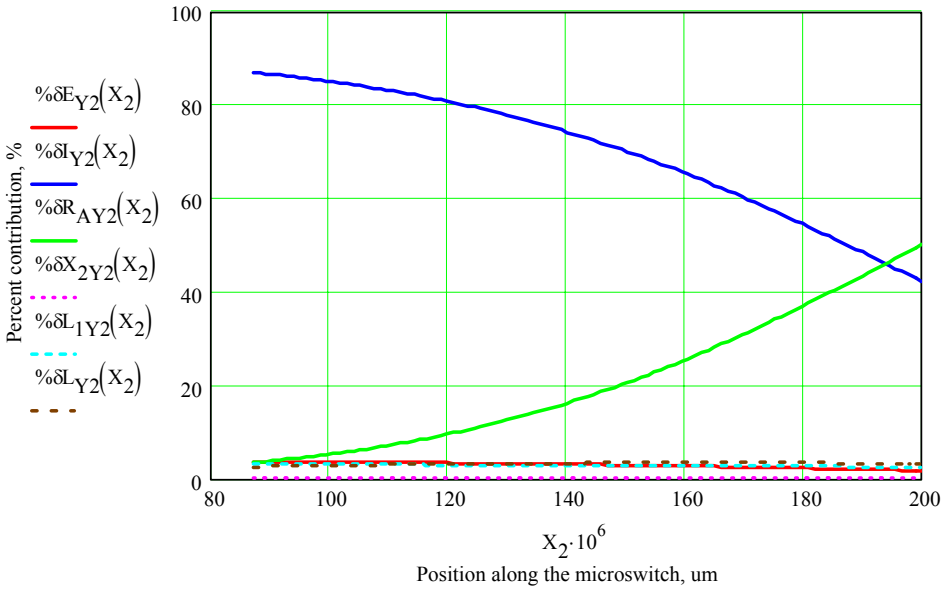

Fig. 4.23. Percent contributions of uncertainties in individual parameters to the overall uncertainty in deformations of section-2 of the cantilever as a function of position along the microswitch on a lin-lin scale.

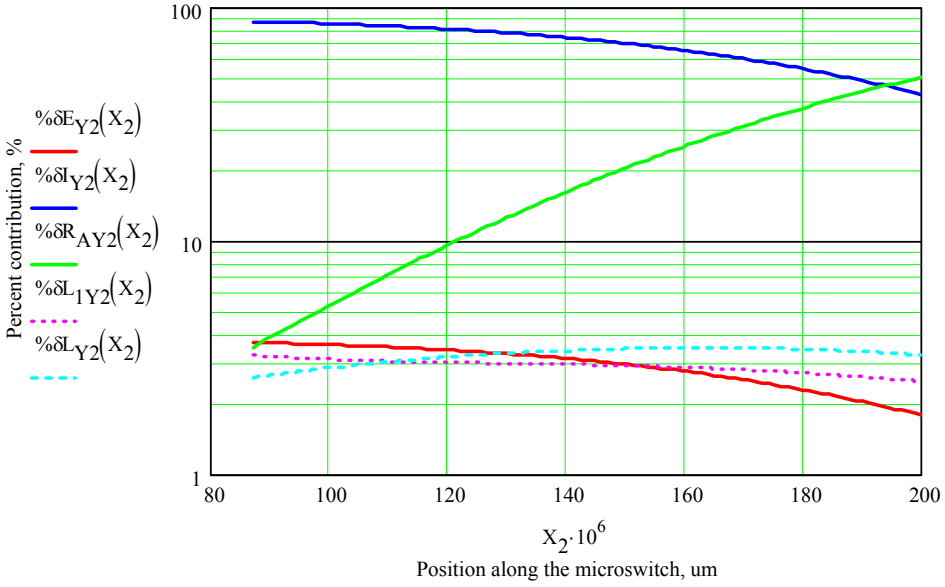

Fig. 4.24. Percent contributions of uncertainties in individual parameters to the overall uncertainty in deformations of section-2 of the cantilever as a function of position along the microswitch on a lin-log scale.

4.4. Circuit performance

The S-parameters of any RF circuit give information about the performance of the circuit. The S_{21} obtained form the S-parameter matrix describes the isolation and insertion loss of the RF microswitch included in the circuit. The isolation of the microswitch is found as the RF microswitch is open, while the insertion loss is found as the microswitch is in its closed position. Both the isolation and insertion loss of the RF microswitch considered in this thesis are functions of operational frequency, as shown in Figs 4.25 and 4.26, respectively.

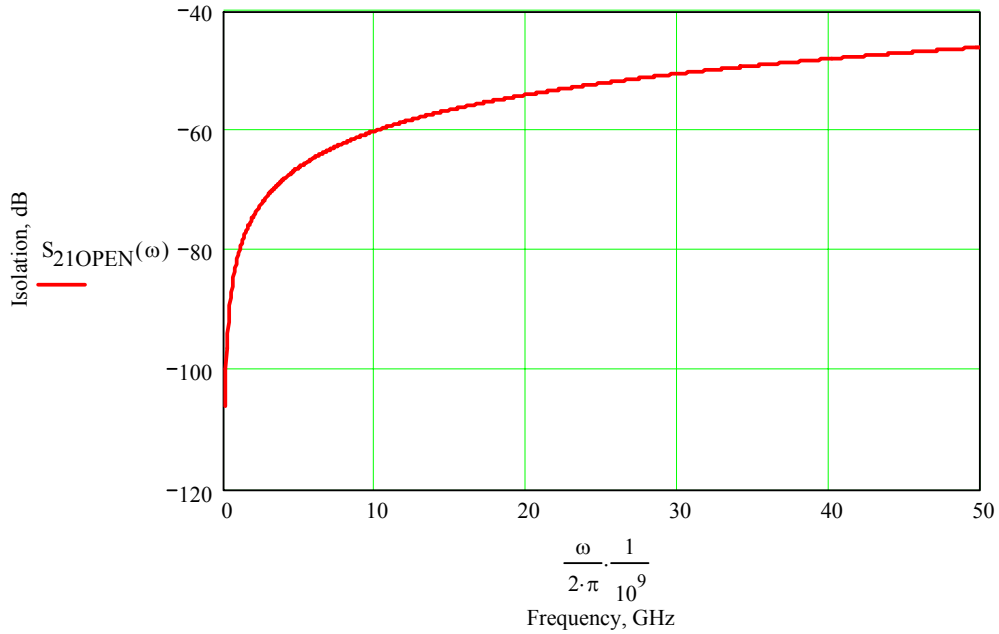

Fig. 4.25. Isolation of the RF microswitch as a function of its operational frequency.

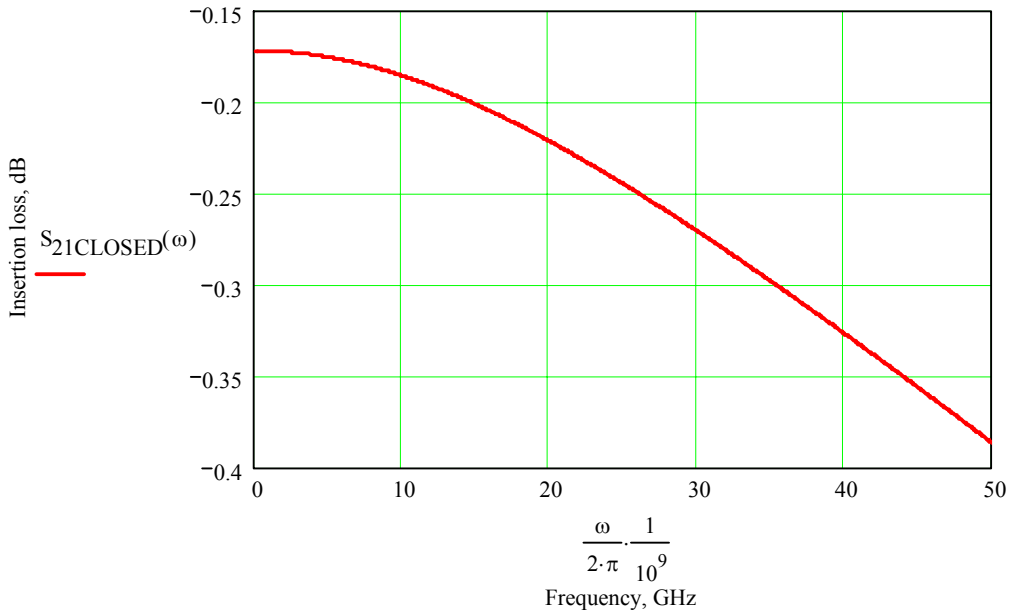

Fig. 4.26. Insertion loss of the RF microswitch as a function of its operational frequency.

Figure 4.25 shows that isolation decreases as the operational frequency of the microswitch increases. Although insertion loss, Fig. 4.26, is not a strong function of operational frequency of the microswitch it increases as the frequency increases.

4.5. Experimental images

Using the OEILM setup described in Section 3.5 images shown in Figs 4.27 to 4.30 were recorded. These images are necessary to configure the OELIM system for measurements and characterization of the RF MEMS switches during their functional operation (Pryputniewicz, et al., 2002a, 2002b). This characterization will be done in the future, as a follow-up of this thesis.

The image shown in Fig. 4.27 displays a full die with multiple RF MEMS components on it. The components are various cantilever-type microswitches, number of capacitive microswitches, as well as some combdrive activated microswitches. A more detailed image, shown in Fig. 4.28, illustrates number of capacitive RF MEMS switches as well as eighteen sets of cantilever-type microswitches. The cantilever-type microswitches are in sets of five, each with variable width dimension. These sets of microswitches, each of different length, are shown in Fig. 4.29. Finally, Fig. 4.30 shows the cantilever type contact RF MEMS switch, which needs to be released before its functional utilization. This particular microswitch is 18 μm wide and 200 μm long.

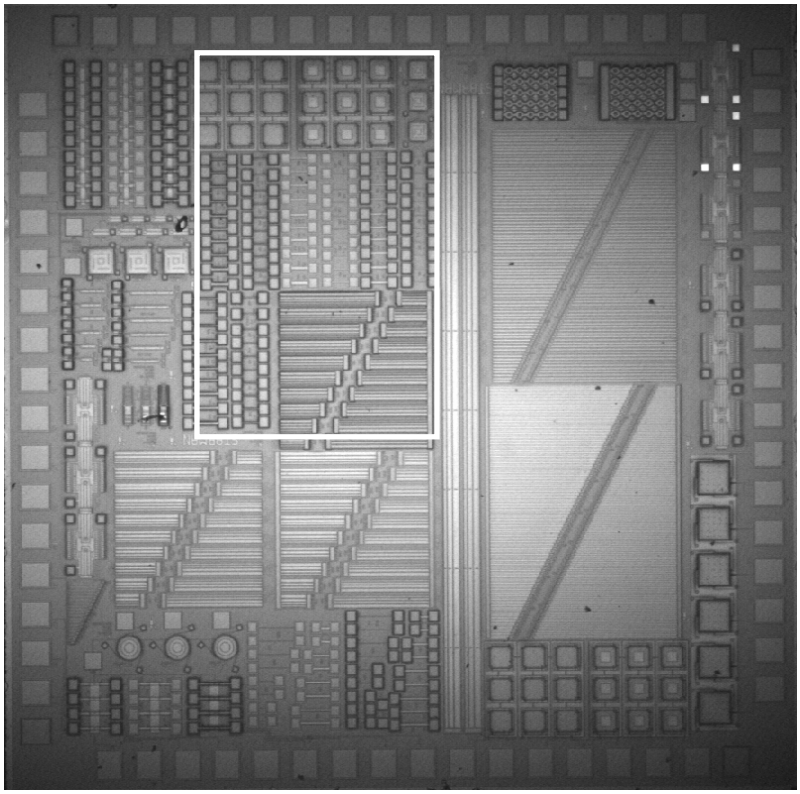

Fig. 4.27. Unreleased die containing multiple RF MEMS components, 5 mm × 5 mm.

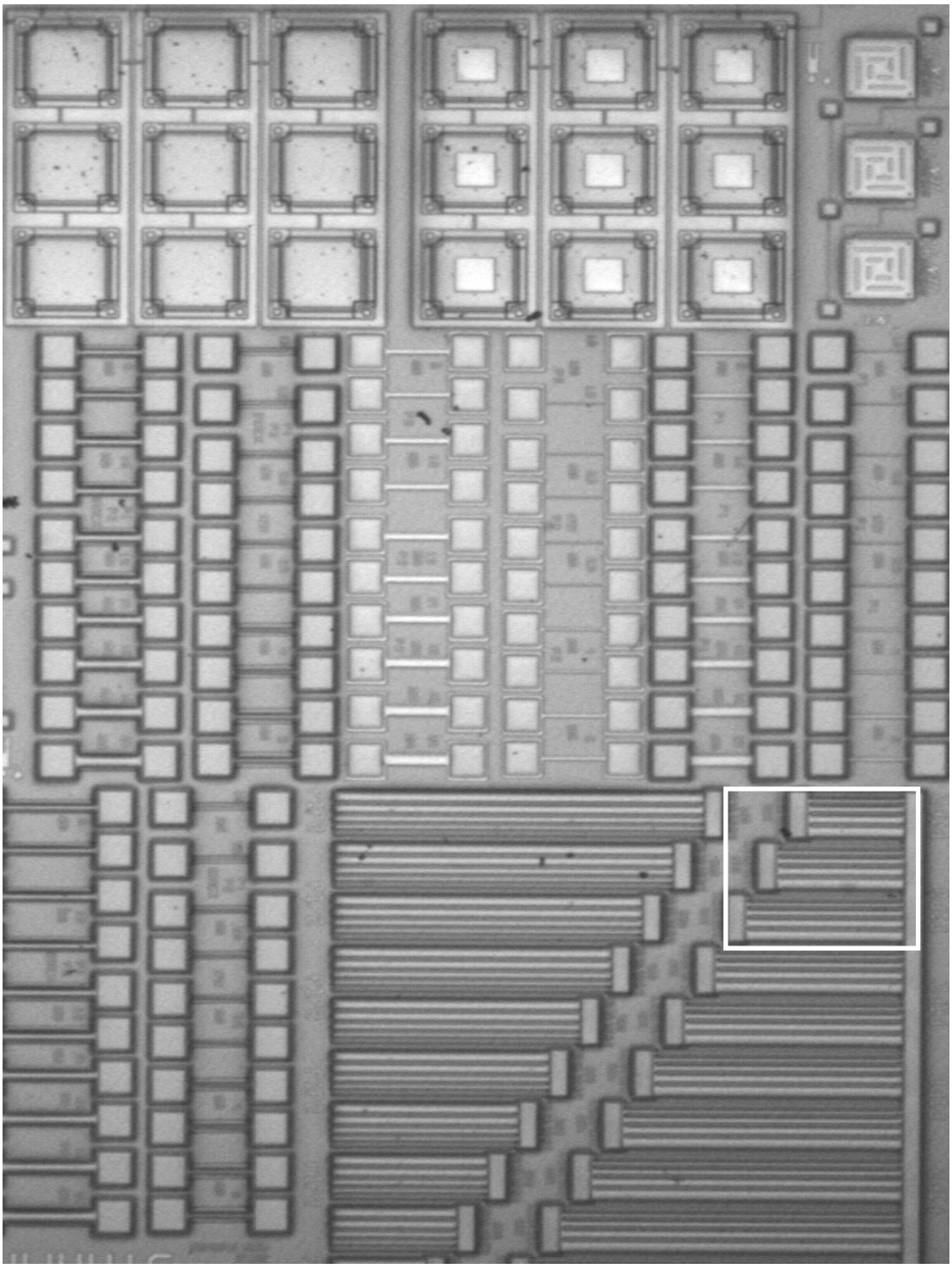

Fig. 4.28. Detail of the unreleased die, highlighted in Fig. 4.27.

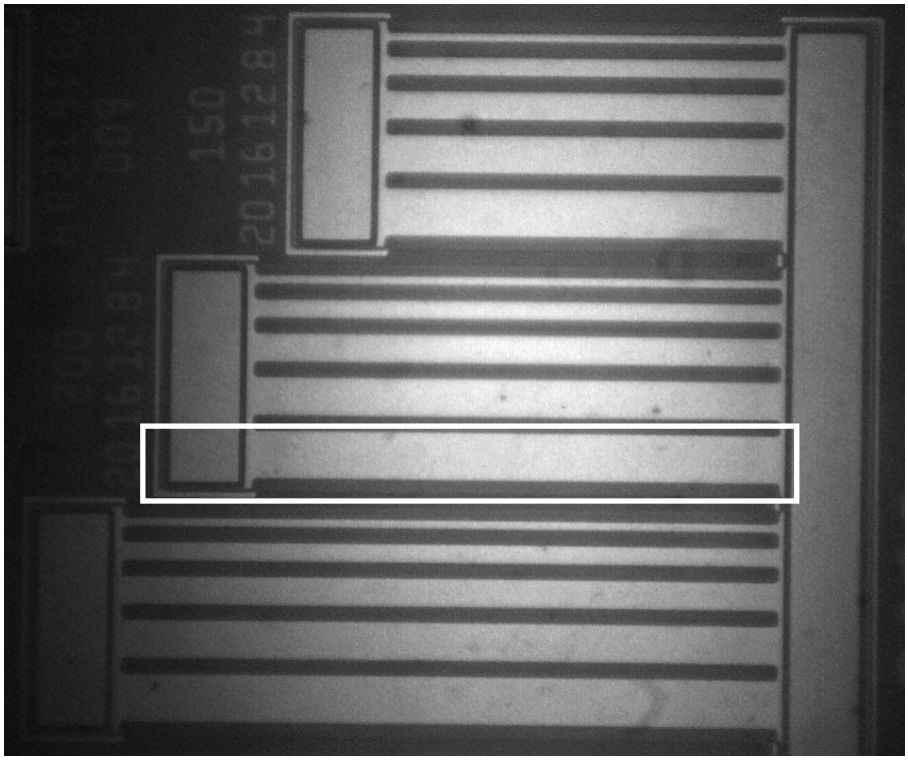

Fig. 4.29. Unreleased cantilever-type RF MEMS switches of variable width, highlighted in Fig. 4.28.

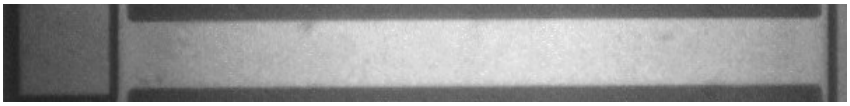

Fig. 4.30. Unreleased cantilever type RF MEMS switch, highlighted in Fig. 4.29, 200 μm long and 18 μm wide.

Interferometric images were obtained using the OELIM methodology. Five phase shifted images necessary to analyze the deformations of the die, due to residual stresses developed during the fabrication process, were recorded. Figure 4.31 shows a sample image of the cantilever-type RF MEMS switches. From these images a wrapped phase map is obtained, Fig. 4.32. Phase unwrapping is performed in order to determine deformations of the section of the die being characterized, Fig. 4.33.

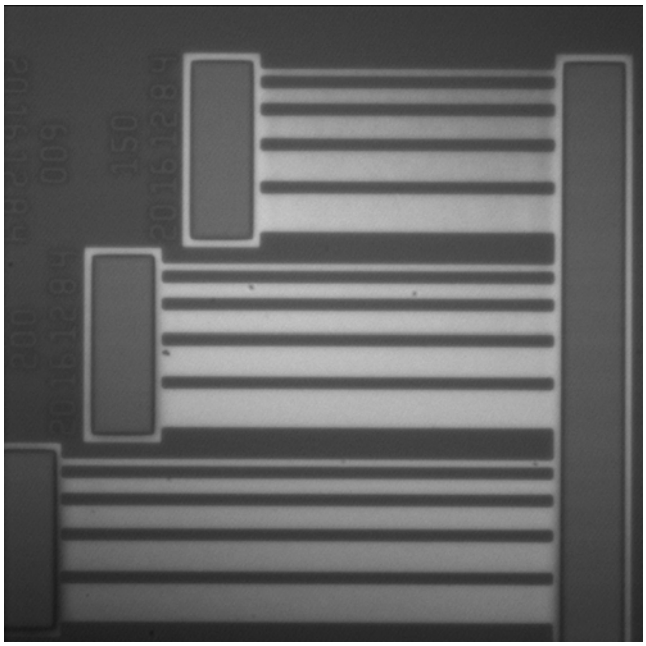

Fig. 4.31. Sample phase shifted image of the RF MEMS switches.

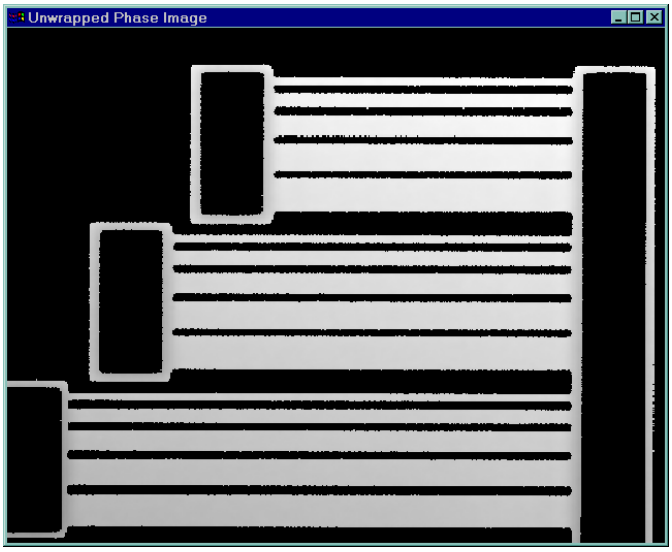

Fig. 4.32. Wrapped phase map of the RF MEMS switches.

Results shown in Fig. 4.33 indicate a maximum out of plane deformation of 350 nm, which is rather large, considering that the microswitches are not yet released. The

interferometric images aid greatly in determining the manufacturing reliability of the RF MEMS switches.

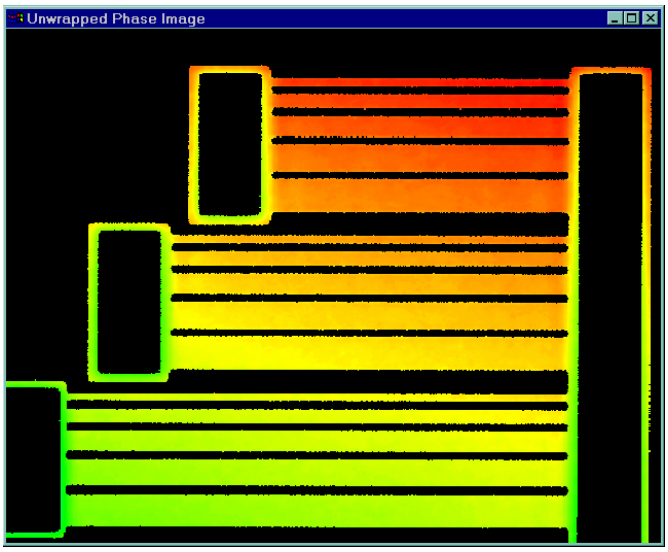

Fig. 4.33. OELIM determined deformations of a section of die containing representative RF MEMS contact switches.

5. CONCLUSIONS AND FUTURE WORK

Preliminary analytical and computational modeling of the RF MEMS contact switch were successfully performed using a set of relationships specially developed in this thesis, Pro/MECHANICA software, and Thermal Analysis System (TAS) softwares. Preliminary experimental evaluation of a microswitch was also initiated. Use of the analytical, computational, and experimental approaches to study, in this thesis, reliability of the RF MEMS switches, is based on the analytical, computational, and experimental solutions (ACES) methodology.

Results obtained in this thesis indicate correlation between the parameters specifying operational conditions of the microswitch and the temperatures reached by the microswitch. The electrostatic force, along with other parameters, like surface finish or material properties of the conductor, directly affect the electrical resistance of the contacts. By increasing contact force the electrical resistance can be minimized. Low electrical resistance has an impact on power dissipation through the switch, thus the thermal resistance. Controlled thermal resistance directly affects the operational temperatures and, therefore, reliability of the RF MEMS switches.

Calculations performed according to the equations governing stress distributions showed that the force of 6.44 μN is sufficient to close the contact gap(s). The calculations also showed that increasing the force, acting on the cantilever-type microswitch, increases actual areas of the contacts. The increases in the actual contact area(s) lead to lower interfacial resistance(s) that, in turn, result in lower temperature raises due to Joule heating, thus increasing reliability of the RF MEMS switches.

Increased force, however, also results in greater wear of the contacts. Greater wear, eventually, leads to tribological failure of the microswitches, adversely affecting their reliability. Therefore, careful considerations of multiple effects, frequently conflicting, of a change in a specific parameter, characterizing functional operation of the RF MEMS switches, must be made before the change is recommended for implementation.

Computational analyses of deformations of the cantilever-type microswitch produced results in good agreement with those obtained from the analytical solutions. The Pro/MECHANICA model showed a deformation of 1.0 μm due to the electrostatic force of 6.44 μN, thus effectively closing the contact gap, which, for the configuration of the microswitch used in this thesis, was 1.0 μm.

Computational modeling in TAS clearly showed that two ends of the shorting bar, in the configuration of the RF MEMS switch considered in this thesis, are affected the most by the Joule heat. As expected, these heat-affected zones are the contact interfaces between the shorting bar and the traces. Temperatures of these areas reached the magnitudes of about 700°C, for the design and operating conditions considered in this thesis. However, the maximum temperatures reduced to about 400°C when contact resistance was reduced to half of its original value. At these high temperatures, the material used for contacts, in this case gold, softens and tends to migrate, causing material transfer between the contacts, which leads to a premature wear. These are cumulative temporal effects that should be avoided in order to increase reliability and life expectancy of the microswitch.

In the future, TAS modeling and simulation of thermal effects in the microswitches should be continued to include different geometries, dimensions, materials, and operating conditions. Also, experiments should be conducted to measure actual thermal fields and dynamic characteristics of operational RF MEMS switches.

Measurements of thermal fields are necessary to validate computational results. This can be achieved by using, e.g., microscope based computer controlled infrared (IR) camera system, which determines temperature fields based on distributions of emissive characteristics of the surface, measured during selfcalibration.

Dynamic characteristics are critical for effective optimization of microswitches because they must close and open on demand and accurate knowledge of their response times, and corresponding mode shapes, is necessary to assure quality of their functional operation. These characteristics can be determined using optoelectronic laser interferometric microscope (OELIM) methodology, which was pioneered at WPI-ME/CHSLT-NEST laboratories. OELIM methodology provides very high spatial resolution and nanometer measurement accuracy in full-field-of-view and near real-time while assuring noninvasive remote measurements and, as such, is particularly suitable for studies and investigation of MEMS.

Only with the completion of experiments, and correlation of the experimental results with the analytical and computational results, the ACES methodology will be fulfilled. This correlation must be judiciously performed subject to rigorous uncertainty analysis. Then, recommendations can be made to change specific parameters affecting design and performance of the RF MEMS switches. When these recommendations are

implemented and new microswitches are fabricated, they will have to be tested, subject to the ACES methodology, to determine the effects due to the changes made and to validate the improvements resulting from these changes.

When validated, the ACES methodology may become an invaluable tool in the development of reliable RF MEMS switches.

REFERENCES

I. Babuska and B. Szabo, 1991, *Finite element analysis*, Wiley, New York.

F. P. Beer and E. R. Johnston, Jr., 1996, *Mechanics of materials*, 2nd ed., McGraw-Hill, New York.

E. Brown, 1998, "RF-MEMS switches for reconfigurable integrated circuits," *IEEE Trans. on Microwave Theory and Techniques*, 46:1868-1880.

G. C. Brown, 1999, *Laser interferometric methodologies for characterizing static and dynamic behavior of MEMS*, Ph.D. Dissertation, Worcester Polytechnic Institute, Worcester, MA.

G. C. Brown and R. J. Pryputniewicz, 1998, "Holographic microscope for measuring displacements of vibrating microbeams using time-average electro-optic holography," *Opt. Eng.*, 37:1398-1405.

B. Bhushan, 1996, "Contact mechanics of rough surfaces in tribology: single asperity contact," *Appl. Mech. Rev.*, 49:275-298.

B. Bhushan, 1998, "Contact mechanics of rough surfaces in tribology: multiple asperity contact," *Tribology Lett.*, 4:1-35.

W. R. Chang, I. Etsion, and D. B. Bogy, 1987, "An elastic-plastic model for the contact of rough surfaces," *J. Tribology*, 109:257-263.

H. W. Coleman and W. G. Steele, Jr., 1989, *Experimentation and uncertainty analysis for engineers*, Wiley, New York, pp. 26-47.

Cronos, 2002, *MEMS Business Unit*, JDS Uniphase, Research Triangle Park, NC.

H. J. De Los Santos and R. J. Richards, 2001, "MEMS for RF/microwave wireless applications: the next wave," *Microwave J.*, 44:20-41.

C. Furlong, 1999, *Hybrid, experimental and computational, approach for the efficient study and optimization of mechanical and electro-mechanical components*, Ph.D. Dissertation, Worcester Polytechnic Institute, Worcester, MA.

C. Furlong, J. S. Yokum, and R. J. Pryputniewicz, 2002, "Sensitivity, accuracy, and precision issues in optoelectronic holography based on fiber optics and high-spatial and high-digital resolution cameras," *Proc. SPIE*, 4778:216-223.

J. A. Greenwood, 1966, "Constriction resistance and the real area of contact," *British J. of Appl. Phys.*, 17:1621-1632.

J. A. Greenwood and J. B. P. Williamson, 1966, "Contact of nominally flat surfaces," *Proc. Roy. Soc. London*, A295:300-319.

F. W. Grover, 1946, *Inductance calculation, working formulas and tables*, Dover Publications, New York.

J. P. Holman, 2002, *Heat transfer*, 9th ed., McGraw-Hill, New York.

T. R. Hsu, 2002, *MEMS & microsystems: design and manufacturing*, McGraw-Hill, New York.

S. Kalpakjian and S. R. Schmid, 2001, *Manufacturing engineering and technology*, Prentice-Hall, Upper Saddle River, NJ.

D. A. Koester, R. Mahadevan, B. Hardy, and K. W. Markus, 2001, *MUMPs® design handbook*, Rev. 7.0, Cronos Integrated Microsystems, Research Triangle Park, NC.

X. Li, F. Sherman, and C. J. Kim, 1999, "Design and development of MEM microwave switches," *MICRO Project 98-070*, University of California, Los Angeles, CA.

R. Ludwig and P. Bretchko, 2000, *RF circuit design theory and applications*, Prentice-Hall, Upper Saddle River, NJ.

R. Maboudian, R. Ashurst, and C. Carraro, 2000, "Self-assembled monolayers as anti-stiction coating for MEMS: characteristics and recent developments," *Sensors and Actuators*, A82:219-223.

M. S. Machate, D. A. Rosato, C. Furlong, and R. J. Pryputniewicz, 2003, "Thermal management of RF MEMS switches: computational investigation," *Proc. 30th Annual Symp. and Exhibition of IMAPS-NE*, Boxboro, MA, pp. 174-182.

R. S. Mroczkowski, 1998, *Electronic connector handbook*, McGraw-Hill, New York.

R. H. Norris, F. F. Buckland, N. D. Fitzroy, and D. A. Kaminski, 1979, *Heat transfer data book*, General Electric Company, Corporate Research and Development, Schenectady, NY.

K. Petersen, 1979, "Micromechanical switches on silicon." *IBM J. Res. Develop.*, 23:376-385.

D. R. Pryputniewicz, 1997, *ACES approach to the development of microcomponents*, MS Thesis, Worcester Polytechnic Institute, Worcester, MA.

D. R. Pryputniewicz, D. G. Grabbe, and R. J. Pryputniewicz, 2001a, "New microcontact for separable, reusable, high digital speed level-2 interconnections," *Proc. 35th Internat. Symp.on Microelectronics*, Denver, CO, pp. 784-798.

R. J. Pryputniewicz, 1981, "High precision hologrammetry," *Internat. Arch. Photogramm.*, 24:377-386.

R. J. Pryputniewicz, 1990, "Automated systems for quantitative analysis of holograms," *Holography*, SPIE-IS8:215-246.

R. J. Pryputniewicz, 1993, *Engineering experimentation*, Worcester Polytechnic Institute, Worcester, MA.

R. J. Pryputniewicz, 1995a, "Hologram interferometry from silver halide to silicon and… beyond," *Proc. SPIE*, 2545:405-427.

R. J. Pryputniewicz, 1995b, "Quantitative determination of displacements and strains from holograms," Ch. 3 in *Holographic interferometry*, Vol. 68 of Springer Series in Sciences, Springer-Verlag, Berlin, pp. 33-72.

R. J. Pryputniewicz, 2001, *Integrated thermomechanical design and analysis*, Worcester Polytechnic Institute, Worcester, MA.

R. J. Pryputniewicz, 2002, *MEMS SUMMiT™V technology*, Worcester Polytechnic Institute, Worcester, MA.

R. J. Pryputniewicz and C. Furlong, 2002, *MEMS and nanotechnology*, Worcester Polytechnic Institute, Worcester, MA.

R. J. Pryputniewicz and C. Furlong, 2003, "Novel optoelectronic methodology for testing of MOEMS," *Proc. Internat. Symp. on MOEMS and Miniaturized Systems III*, SPIE-4983:11-25.

R. J. Pryputniewicz, C. Furlong, S. P. Mizar, P.W. Wilkerson, and A. J. Przekwas, 2001b, "RF MEMS: investigation of a fast contact switch," *Proc. 29th Symp. and Exhibition of IMAPS-NE*, Boxboro, MA, pp. 284-288.

R. J. Pryputniewicz, P.W. Wilkerson, A. J. Przekwas, and C. Furlong, 2001c, "RF MEMS: modeling and simulation of switch dynamics," *Proc. 35th Internat. Symp.on Microelectronics*, Denver, CO, pp. 267-272.

R. J. Pryputniewicz, C. Furlong, G. C. Brown, E. J. Pryputniewicz, and M. E. Seta, 2001d, "Optoelectronic method for studies of MEMS," *Proc. Internat. Congress on Experimental and Applied Mechanics for Emerging Technologies*, Portland, OR, pp. 817-820.

R. J. Pryputniewicz, D. Rosato, and C. Furlong, 2002a, "Measurements and simulation of SMT components," *Proc. 35th Inter. Symp. on Microelectronics*, Denver, CO, pp. 151-156.

R. J. Pryputniewicz, P. W. Wilkerson, A. J. Przekwas, and C. Furlong, 2002b, "Modeling and simulation of RF MEMS switches," *Paper No. IMECE2002-34504*, Am. Soc. Mech. Eng., New York.

R. J. Pryputniewicz, C. Furlong, and E. J. Pryputniewicz, 2002c, "Optimization of contact dynamics for an RF MEMS switch," *Paper No. IMECE2002-39504*, Am. Soc. Mech. Eng., New York.

PTC, 2003a, *Pro/ENGINEER user manual*, Parametric Technology Corporation, Needham, MA.

PTC, 2003b, *Pro/MECHANICA user manual*, Parametric Technology Corporation, Needham, MA.

PTC, 2003c, "Suggested technique for understanding the p-version of the finite element method," *PTC Technical Support Knowledge Base*, http://www.ptc.com/cs/cs_24/howto/mst2432/mst2432.htm, Parametric Technology Corporation, Needham, MA.

J. R. Reid and L. A. Starman, 2003, "RF MEMS: switches, variable capacitors, and circuits," *IEEE course notes*, AFRL/SNHA, Hanscom AFB, MA.

D. A. Rosato, 2002, *Thermal analysis system – user's manual*, Ver. 6.1, Harvard Thermal, Inc., Harvard, MA.

V. Steward, 2003, *Modeling of a folded spring supporting MEMS gyroscope*, MS Thesis, Worcester Polytechnic Institute, Worcester, MA.

Tyco, 2000a, "Relay contact life," *Application Note 13C3236*, Tyco Electronics Corporation – P&B, Winston-Salem, NC.

Tyco, 2000b, "Contact arc phenomenon," *Application Note 13C3203*, Tyco Electronics Corporation – P&B, Winston-Salem, NC.

C. Wang, R. Ramadoss, S. Lee, K. C. Gupta, V. Bright, and Y. C. Lee, 2001, "Flexible circuit-based RF MEMS switches," *Paper No. IMECE2001/MEMS-23907*, Am. Soc. Mech. Eng., New York.

E. A. Wolff and R. Kaul, 1988, *Microwave engineering and system applications*, Wiley, New York.

J. Yao and M. Chang, 1995, "A surface micromachined miniature switches for telecommunications applications with signal frequencies from DC up to 4 GHz," *Transducers'95*, 2: 384-387.

J. Zou, C. Lui, J. Schutt-Aine, J. Chen, and S. M. Kang, 2000, "Development of a wide tuning range MEMS tunable capacitor for wireless communication systems," *Technical Digest, Internat. Electron Devices Meeting (IEDM)*, pp. 403-406.

APPENDIX A. ANALYSIS OF DEFORMATIONS OF THE CANTILEVER

Equation to model deformations of the cantilever are based on the parameters defined in Fig. A.1.

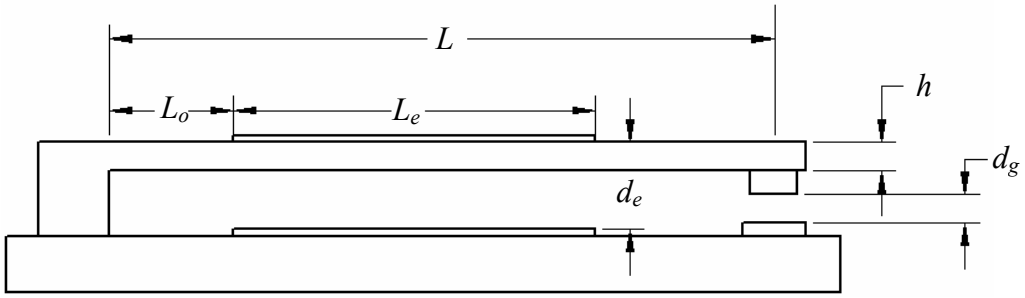

Fig. A.1. RF MEMS cantilever-type microswitch considered in this thesis.

Nominal values of the parameters defined Fig. A.1, as used in this thesis, are as follows:

beam width:	$b = 20$	μm
beam thickness:	$h = 2.5$	μm
beam length:	$L = 200$	μm
distance to electrode:	$L_o = 12$	μm
electrode gap distance:	$d_e = 4.5$	μm
contact gap distance:	$d_g = 1$	μm
electrode length:	$L_e = 150$	μm
electrode width:	$b_e = 20$	μm
modulus of elasticity:	$E = 160$	GPa
density:	$\rho = 2.33$	$\frac{\text{g}}{\text{cm}^3}$

air dielectric constant: $\varepsilon_o = 8.85\ 10^{-6}$ $\frac{\text{F}}{\mu\text{m}}$

relative permittivity of polysilicon: $\varepsilon_r = 3$.

The elastic deformation of the cantilever due to the applied force can be determined using the elastic curve equation

$$EI\frac{d^2y}{dx^2} = M(x) \quad , \tag{A.1}$$

where

$$I = \frac{1}{12}bh^3 \quad . \tag{A.2}$$

Deformations of the cantilever before contact is made are calculated using parametric designations shown in Fig. A.2. The parameters L_1 and L_2 can be rewritten in terms of the cantilever geometry as

$$L_1 = L_o + \frac{L_e}{2} \tag{A.3}$$

and

$$L_2 = L - L_1 \quad . \tag{A.4}$$

For calculation purposes the ranges of the horizontal or x-distances are defined as

$$x_1 = 0, \frac{L_1}{N} \ldots L_1 \tag{A.5}$$

and

$$x_2 = L_1, L_1 + \frac{L - L_1}{N} \ldots L \tag{A.6}$$

where N is the number of increments in the set range and it is equal to 100.

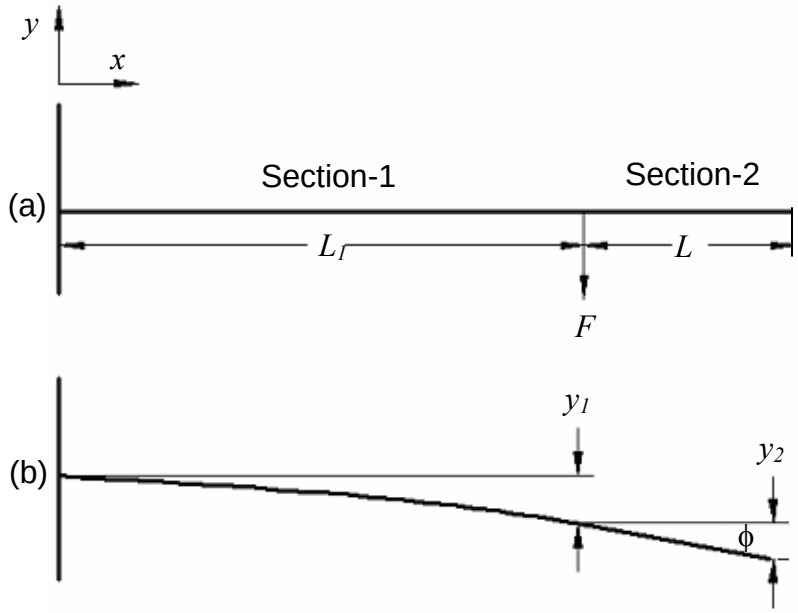

Fig. A.2. Deformations of electrostatically actuated cantilever: (a) at the beginning of actuation (zero deformation), (b) at the end of actuation (maximum deformation).

Deformations of the cantilever due to electrostatic force will vary along its length. The deformations of the cantilever from its attached end to the point of force application, i.e., within section-1, can be represented by an elastic curve, while the deformations for portion of the cantilever from the point of the force application to the free end, i.e., section-2, can be represented as a linear function of position. Based on Fig. A.3, the summation of forces for section-1 of the cantilever is as follows:

$$\sum_{y} F = R_o - F = 0 \quad , \tag{A.7}$$

where forces in the upward direction are considered positive. Solving Eq. A.7 for F gives

$$R_o = F \quad . \tag{A.8}$$

The summation of moments for section-1 of the cantilever is

$$\sum_{o} M = Fx - M_o = 0 \qquad , \tag{A.9}$$

where moments in clockwise direction are assumed to be positive.

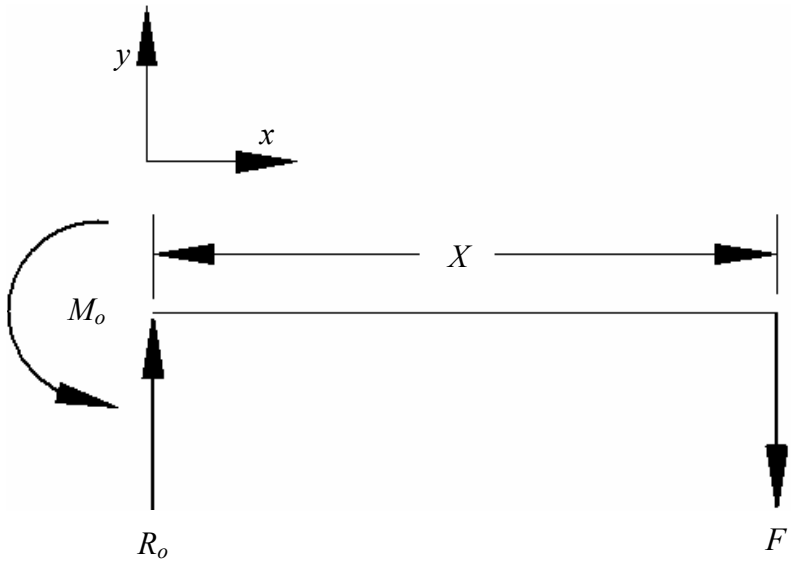

Fig. A.3. Free-body diagram of section-1 of the cantilever.

Based on Eq. A.9,

$$M_o = FL_1 \qquad , \tag{A.10}$$

if L_1 is substituted for x, knowing that section-1 has the length of L_1. Summing the forces at an arbitrary distance x, Fig. A.4, we obtain

$$\sum_{y} F = R_o - V_1 = 0 \qquad . \tag{A.11}$$

Solution of Eq. A.11 for V_1 yields

$$V_1 = R_o = F \qquad , \tag{A.12}$$

where Eq. A.8 was used for simplification. Summation of moments for section-1 at an arbitrary position x gives

$$\sum_{o} M = V_1 x - M_1 - M_o = 0 \quad . \tag{A.13}$$

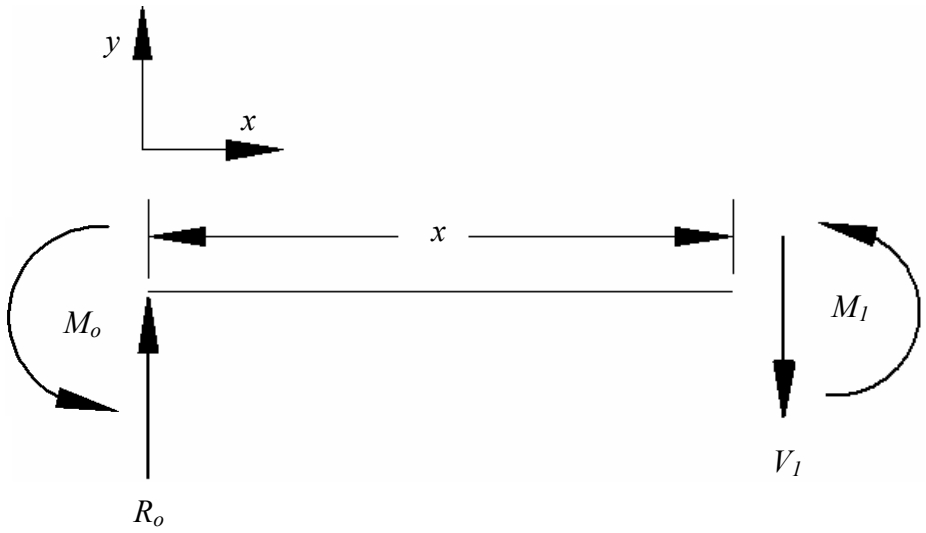

Fig. A.4. Free-body diagram of section-1 of the cantilever at an arbitrary distance x.

As Eq. A.13 is solved for M_1, the result obtained is

$$M_1 = Fx - FL_1 \quad , \tag{A.14}$$

where equivalency of the free-body diagrams of section-1, shown in Figs A.3 and A.4, was taken into consideration. Equation A.14 is then substituted into the general form of the elastic curve equation, i.e.,

$$EI\frac{d^2y}{dx^2} = M(x) = Fx - FL_1 \quad . \tag{A.15}$$

Equation A.15 is integrated once to obtain a general form of the slope equation

$$EI\frac{dy}{dx} = \frac{1}{2}Fx^2 - FL_1x + C_1 \tag{A.16}$$

and integrated again to obtain the general form of the deformation equation for the cantilever

$$EIy = \frac{1}{6}Fx^3 - \frac{1}{2}FL_1x^2 + C_1x + C_2 \quad . \tag{A.17}$$

By applying cantilever boundary conditions at its fixed end, i.e., at $x = 0$, which are

$$y = 0 \tag{A.18}$$

and

$$\frac{dy}{dx} = 0 \quad , \tag{A.19}$$

Eq. A.17 becomes

$$EIy = \frac{1}{6}Fx^3 - \frac{1}{2}FL_1x^2 \quad , \tag{A.20}$$

because, based on boundary conditions specified in Eqs A.18 to A.19,

$$C_1 = 0 \tag{A.21}$$

and

$$C_2 = 0 \quad . \tag{A.22}$$

Therefore Eq. A.16 defining slope of the loaded cantilever, becomes

$$EI\frac{dy}{dx} = \frac{1}{2}Fx^2 - FL_1x \quad . \tag{A.23}$$

Based on preliminary analysis of load deformation characteristics of the RF MEMS contact switch geometry considered in this thesis, equivalent magnitude of the electrostatic force required to close the gap, d_g = 1 μm, at the contact end of the

cantilever, is 6.44 μN. This nominal value of the equivalent force was used in all analyses included in this appendix, unless otherwise specified. Therefore, in the following determinations of deformations and slopes of the cantilever, as function of position along its length, the concentrated force of 6.44 μN applied in the negative *y*-direction at the geometric center of the overlap area of the electrodes actuating the cantilever, i.e., the force of -6.44 μN, will be used. The equation defining deformations of section-1 as a function of position along the cantilever can be written, based on Eq. A.20, as

$$y_1(x_1) = \frac{F}{EI}\left(\frac{1}{6}{x_1}^3 - \frac{1}{2}L_1{x_1}^2\right) \quad , \tag{A.24}$$

while the slope of section-1 as a function of the position along the cantilever, based on Eq. A.23, is

$$m_1(x_1) = \frac{F}{EI}\left(\frac{1}{2}{x_1}^2 - L_1x_1\right) \quad . \tag{A.25}$$

Graphical representations of Eqs A.24 and A.25 are shown in Figs A.5 and A.6, respectively.

Relationships equivalent to Eqs A.24 and A.25, which define deformations and slope of section-1 of the cantilever as a function of position along the microswitch, for section-2 are based on the fact that this section is a straight line characterized by the slope equal to the slope at the end of section-1, i.e., at $x_1 = L_1$, and deformations based on the slope-intercept representation of a line, where the intercept is defined by the deformation of section-1 at $x_1 = L_1$. That is, deformations of section-2 can be defined as

$$y_2(x_2) = m_2(x_2 - L_1) + y_{1\max} \quad , \tag{A.26}$$

where x_2 is the local coordinate within section-2, m_2 is the slope of section-2, and y_{1max} is the intercept, based on the solution for deformation of section-1 at L_1. The specific value of parameters appearing in Eq. A.26 are determined using Eqs A.24 and A.25. Using Eq. A.24 evaluated at $x_1 = L_1$, we obtain

$$y_{1\max} = \frac{1}{3}\frac{F}{EI}L_1^{\,3} \quad , \tag{A.27}$$

which using the force of -6.44 μN, yields

$$y_{1\max} = -3.393\times10^{-1}\,\mu\text{m} \quad . \tag{A.28}$$

Based on Eq. A.25, evaluated at $x_1 = L_1$, the maximum slope of section-1 can be defined by the equation

$$m_{1\max} = \frac{1}{2}\frac{F}{EI}L_1^{\,2} \quad , \tag{A.29}$$

solution of which, subject to F = -6.44 μN, gives

$$m_{1\max} = -5.8504\times10^{-3}\,\text{rad} \quad . \tag{A.30}$$

Therefore, using the result shown in Eq. A.30, the slope of section-2, as a function of position along the microswitch, can be shown to be

$$m_2(x_2) = m_{1\max} = -5.8504\times10^{-3}\,\text{rad} \quad . \tag{A.31}$$

Equation A.31 indicates that slope of section-2 is independent of position along the microswitch. Therefore, substituting Eqs A.28 and A.31 into Eq. A.26, we obtain

$$y_2(x_2) = -5.8504\times10^{-3}(x_2 - L_1) - 3.393\times10^{-1}\,\mu\text{m} \quad . \tag{A.32}$$

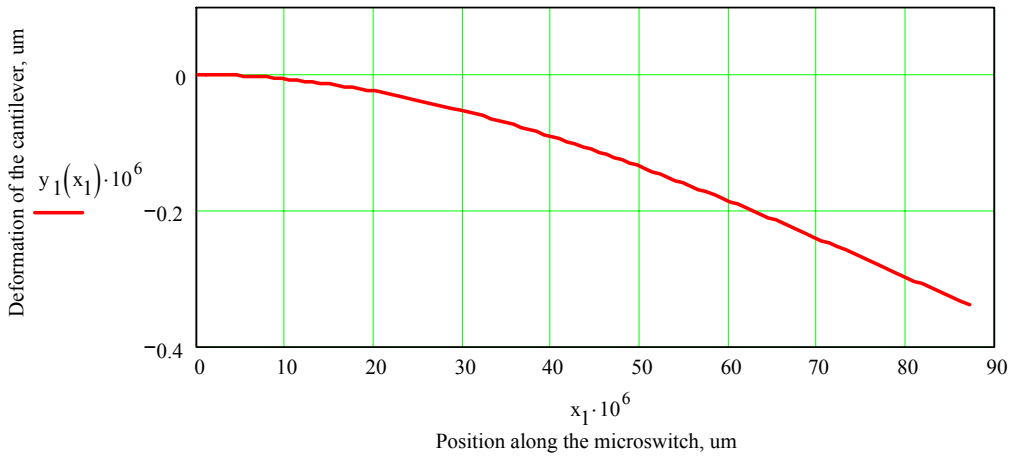

Fig. A.5. Deformations of section-1 of the cantilever as a function of position along the microswitch.

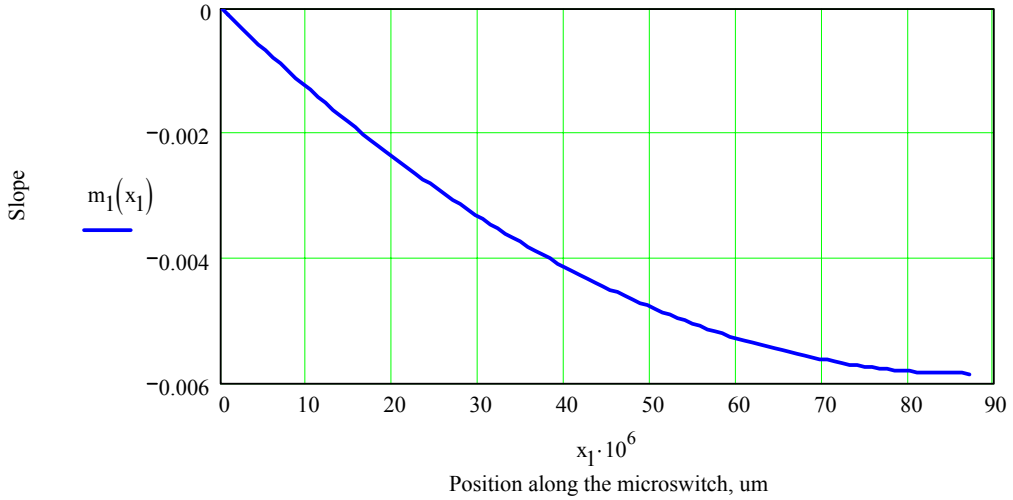

Fig. A.6. Slope of section-1 of the cantilever as a function of position along the microswitch.

Maximum deformation of the entire cantilever can be determined from Eq. A.32 by setting $x_2 = L$ which yields

$$y_{2\max} = -6.611\times10^{-1} - 3.393\times10^{-1} = -1 \ \mu\text{m} \quad . \tag{A.33}$$

Both deformation and slope of section-2 as a function of position along the cantilever are shown in Figs A.7 and A.8, while the deformations and slope of the entire cantilever as functions of position along the microswitch are shown in Fig A.9 and Fig. A.10, respectively.

Once the free end of the cantilever reaches the contact it is supported by it. Thus, elastic deformations of the cantilever due to the applied force have to be determined using this time, different boundary conditions. Deformations of the cantilever beam fixed at one end and simply supported on the other are determined using parameters introduced in Fig. A.11. For the calculation purposes it is assumed that the simply supported end of the cantilever does not move in *y*-direction.

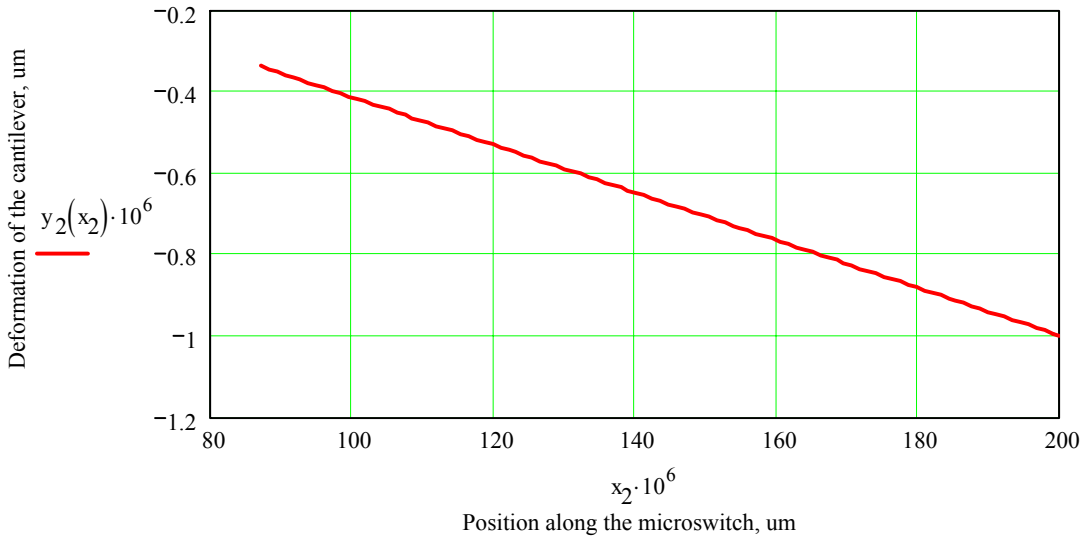

Fig. A.7. Deformations of section-2 of the cantilever as a function of position along the microswitch.

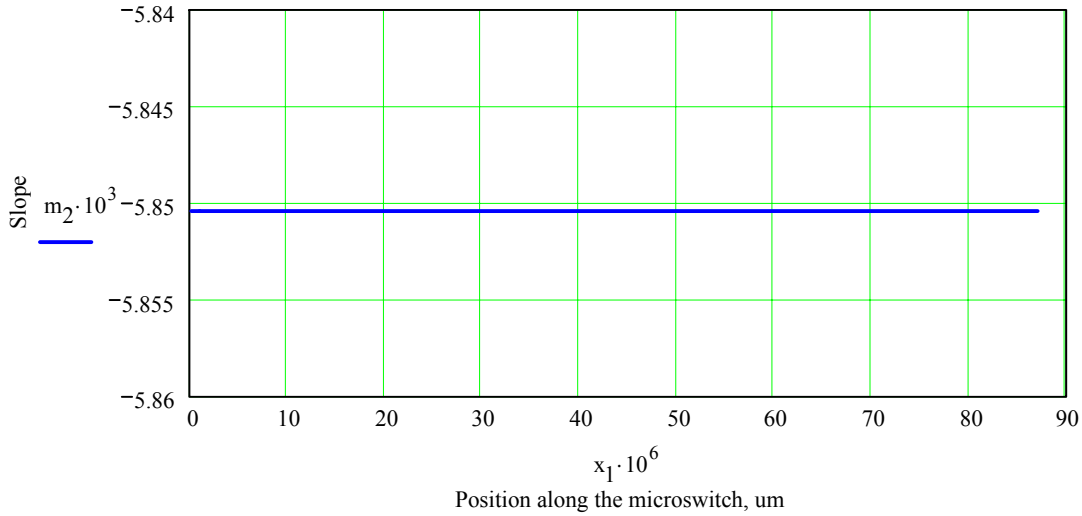

Fig. A.8. Slope of section-2 of the cantilever as a function of position along the microswitch.

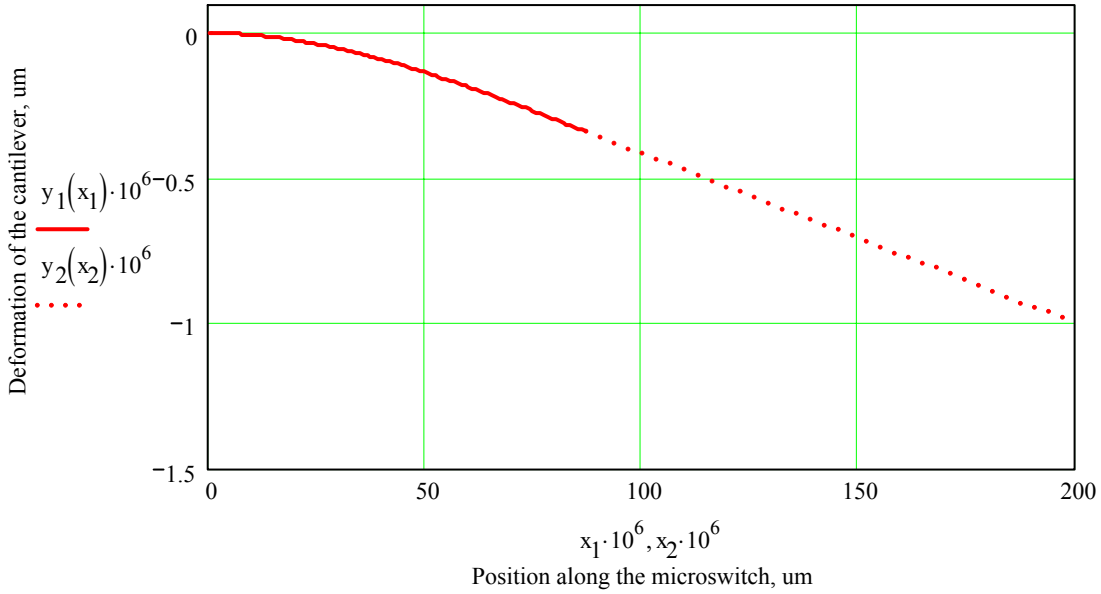

Fig. A.9. Deformations of the entire cantilever as a function of position along the microswitch.

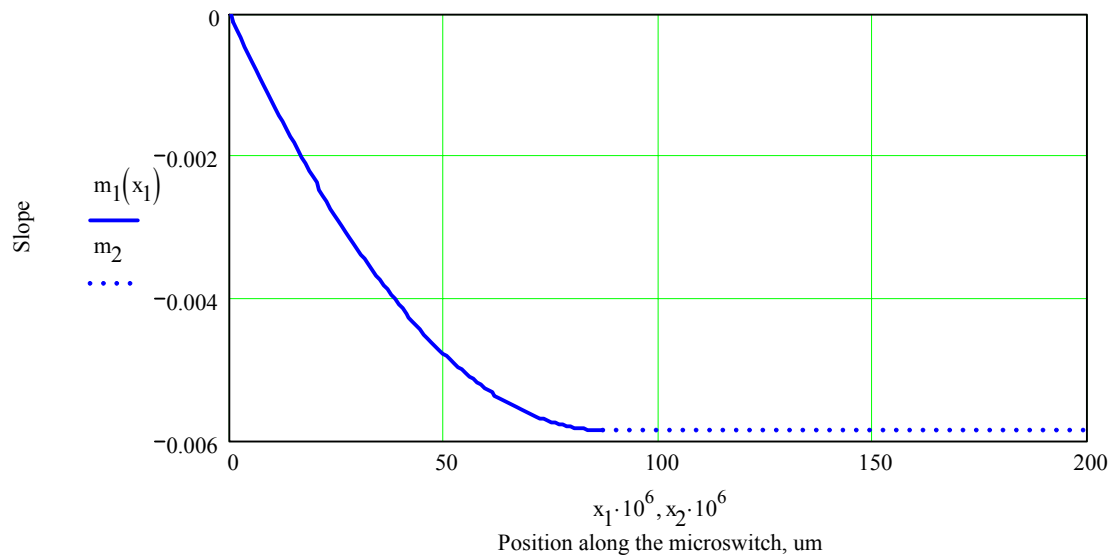

Fig. A.10. Slope of the entire cantilever as a function of position along the microswitch.

As before, L_1 can be rewritten in terms of the cantilever geometry, i.e.,

$$L_1 = L_o + \frac{L_e}{2} \quad . \tag{A.34}$$

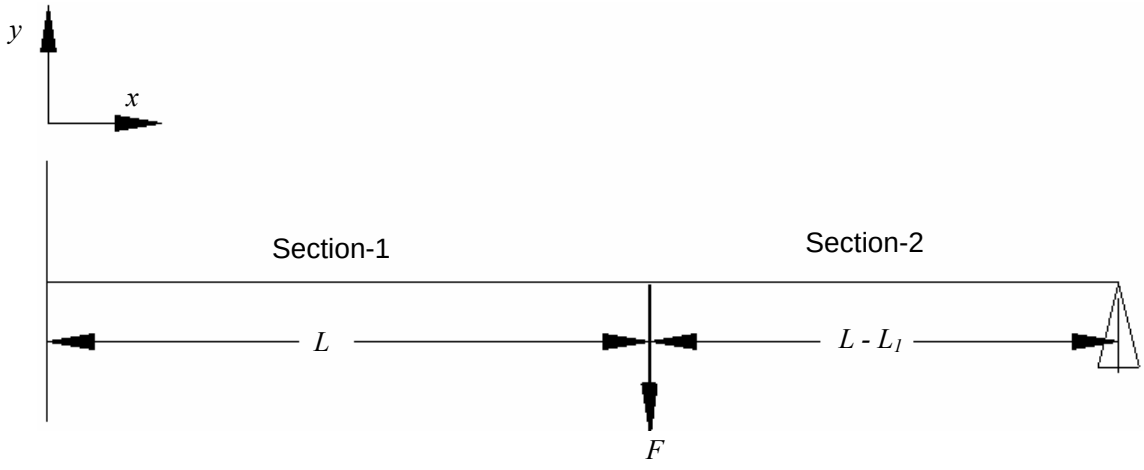

Fig. A.11. Free-body diagram of a fixed-simply supported cantilever, after contact is made.

For the purpose of calculations, the ranges of the horizontal or *x*-distance will be defined as

$$X_1 = 0, \frac{L - L_1}{N} \ldots L - L_1 \tag{A.35}$$

and

$$X_2 = L - L_1, L - L_1 + \frac{L_1}{N} \ldots L \quad , \tag{A.36}$$

where N is the number of increments in the set range and it is equal to 100.

To facilitate derivation of the governing equations, the cantilever had to be divided into two separate sections: section-1, which represents the cantilever from its fixed end to the point of force application and section-2, which represents the cantilever from the point of applied concentrated load to the simply supported end. Summation of forces of section-1 at an arbitrary distance X_1, Fig. A.12, gives

$$\sum_y F = R_A - V_1 = 0 \qquad . \tag{A.37}$$

As Eq. A.37 is solved for V_1, we obtain

$$V_1 = R_A \qquad . \tag{A.38}$$

The summation of moments for section-1 is

$$\sum_B M = -R_A X_1 + M_1 = 0 \qquad . \tag{A.39}$$

When Eq. A.39 is solved for M_1, we obtain

$$M_1 = R_A X_1 \qquad . \tag{A.40}$$

Substituting Eq. A.40 into the general form of the elastic curve we find

$$EI\frac{d^2Y_1}{dx^2} = M(X_1) = R_A X_1 \quad . \tag{A.41}$$

Integrating Eq. A.44 we obtain the general form of the slope equation

$$EI\frac{dY_1}{dx} = \frac{1}{2}R_A {X_1}^2 + C_1 \tag{A.42}$$

and integrating it again we obtain the deformation equation

$$EIY_1 = \frac{1}{6}R_A {X_1}^3 + C_1 X_1 + C_2 \quad . \tag{A.43}$$

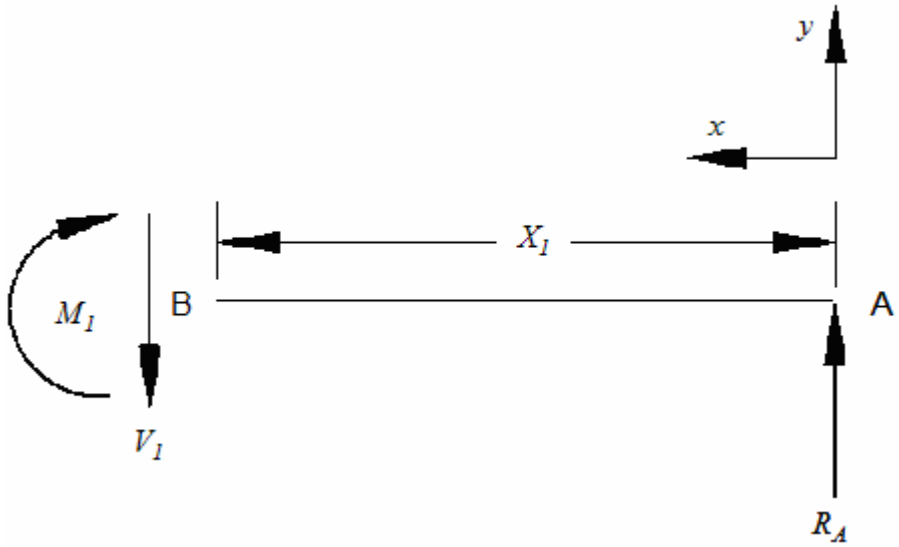

Fig. A.12. Free-body diagram of section-1 of the cantilever, after contact is made.

Summation of forces and moments of section-2 of the cantilever, Fig. A.13, at an arbitrary distance X_2 are as follows:

$$\sum_y F = R_A - F + V_2 = 0 \quad , \tag{A.44}$$

$$V_2 = F - R_A \quad , \tag{A.45}$$

$$\sum_C M = R_A X_2 - F\left[X_2 - \left(L - L_1\right)\right] - M_2 = 0 \quad , \tag{A.46}$$

$$M_2 = R_A X_2 - F X_2 + FL - FL_1 \quad . \tag{A.47}$$

In this case the moments are assumed to be positive in counter clockwise direction.

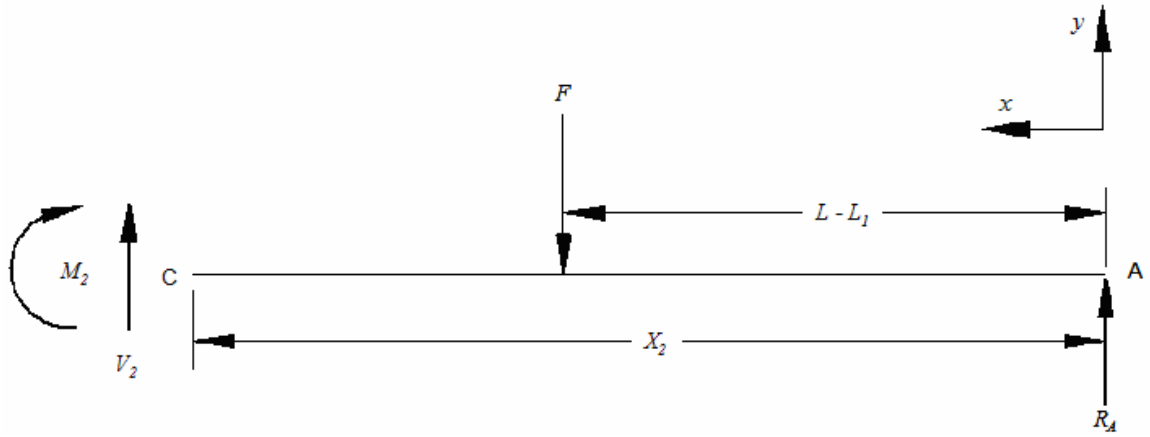

Fig. A.13. Free-body diagram of section-2 of the cantilever, after contact is made.

Substituting Eq. A.47 into the general form of the elastic curve we obtain

$$EI\frac{d^2Y_2}{dx^2} = M\left(X_2\right) = R_A X_2 - F X_2 + FL - FL_1 \quad . \tag{A.48}$$

Integrating Eq. A.48 we find the general form of the slope equation

$$EI\frac{dY_2}{dx} = \frac{1}{2}R_A {X_2}^2 - \frac{1}{2}F{X_2}^2 + FLX_2 - FL_1 X_2 + C_3 \tag{A.49}$$

and integrating it again gives the general form of the deformation equation

$$EIY_2 = \frac{1}{6}R_A {X_2}^3 - \frac{1}{6}F{X_2}^3 + \frac{1}{2}FL{X_2}^2 - \frac{1}{2}FL_1 {X_2}^2 + C_3 X_2 + C_4 \quad . \tag{A.50}$$

In order to solve the unknowns in Eqs A.42 and A.43 and Eqs A.49 and A.50 boundary and continuity conditions have to be applied. The boundary conditions for the cantilever with the fixed-simply supported ends are

$$\text{at} \qquad X_1 = 0 \qquad Y_1 = 0 \quad , \tag{A.51}$$

$$\text{at} \qquad X_2 = L \qquad Y_2 = 0 \quad , \tag{A.52}$$

and

$$\text{at} \qquad X_2 = L \qquad \frac{dY_2}{dx} = 0 \quad , \tag{A.53}$$

while the continuity conditions at the point of force application are

$$\text{at} \qquad X_1 = X_2 = L - L_1 \qquad Y_1 = Y_2 \tag{A.54}$$

and

$$\text{at} \qquad X_1 = X_2 = L - L_1 \qquad \frac{dY_1}{dx} = \frac{dY_2}{dx} \quad . \tag{A.55}$$

Use of Eqs A.51 to A.55 allows determination of all the unknowns in Eqs A.42, A.43, A.49, and A.50, and they are

$$C_1 = -\frac{3}{2} F {L_1}^2 - FLL_1 \quad , \tag{A.56}$$

$$C_2 = \frac{5}{6} F {L_1}^3 - \frac{1}{2} FL {L_1}^2 \quad , \tag{A.57}$$

$$C_3 = 0 \quad , \tag{A.58}$$

$$C_4 = 0 \quad , \tag{A.59}$$

and

$$R_A = F\left(12\frac{{L_1}^2}{L^2} - 6\frac{L_1}{L} - 5\frac{{L_1}^3}{L^3}\right) \quad . \tag{A.60}$$

Substituting Eqs A.56 to A.60 into Eqs A.49 and A.50, the deformations and slope for section-1 of the cantilever become

$$Y_1(X_1) = \frac{1}{EI}\left(\frac{1}{6}F{X_1}^3 - \frac{1}{2}FL{X_1}^2 + \frac{1}{2}FL_1{X_1}^2 - \frac{1}{6}R_A{X_1}^3\right) \tag{A.61}$$

and

$$M_1(X_1) = \frac{1}{EI}\left(\frac{1}{2}F{X_1}^2 - FLX_1 + FL_1X_1 - \frac{1}{2}R_A{X_1}^2\right) \quad , \tag{A.62}$$

respectively. Graphical representations of Eqs A.61 and A.62 are shown in Figs A.14 and A.15, respectively. Deformation and slope of section-2 become

$$Y_2(X_2) = \frac{1}{EI}\left(-\frac{1}{6}R_A{X_2}^3 + \frac{3}{2}F{L_1}^2X_2 - FLL_1X_2 - \frac{5}{6}F{L_1}^3 + \frac{1}{2}FL{L_1}^2\right) \tag{A.63}$$

and

$$M_2(X_2) = \frac{1}{EI}\left(-\frac{1}{2}R_A{X_2}^2 + \frac{3}{2}F{L_1}^2 - FLL_1\right) \quad . \tag{A.64}$$

Deformations and slope of section-2 as functions of position along the cantilever are shown in Figs A.16 and A.17, respectively. Deformations and slope of the entire cantilever, consisting of section-1 and section-2, are shown in Figs A.18 and A.19, respectively.

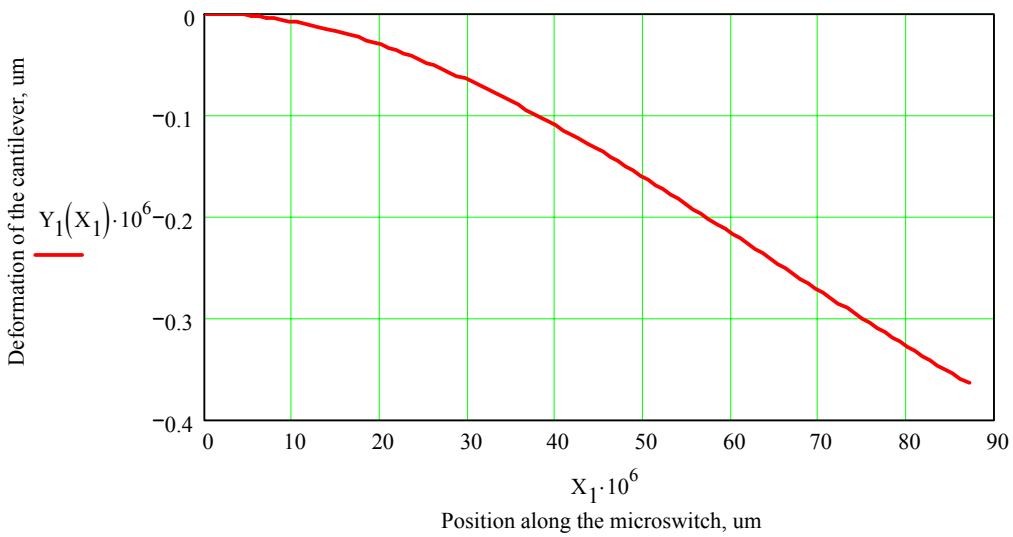

Fig. A.14. Deformations of section-1 of the cantilever as a function of position along the microswitch, after contact is made.

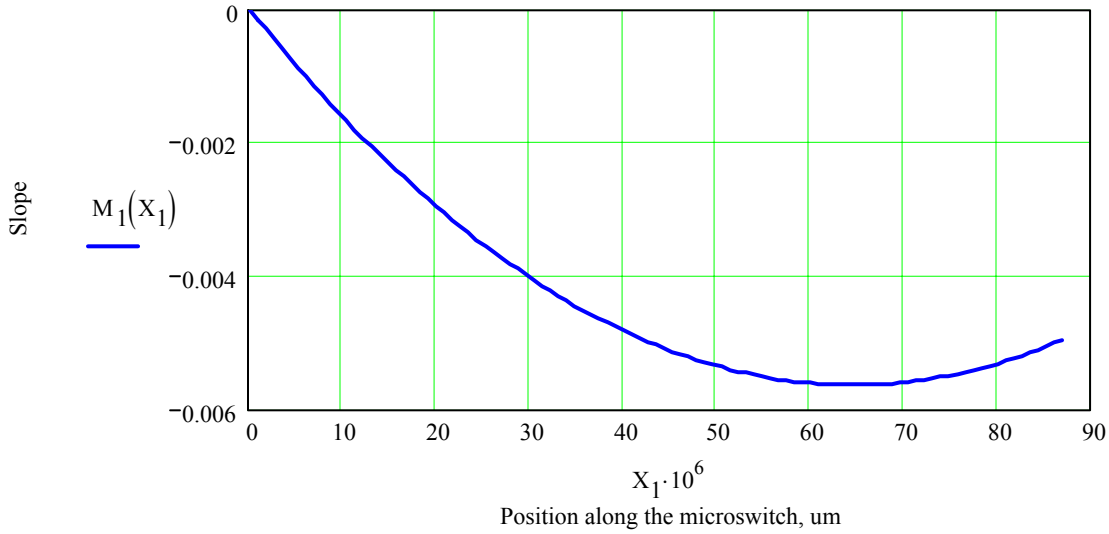

Fig. A.15. Slope of section-1 of the cantilever as a function of position along the microswitch, after contact is made.

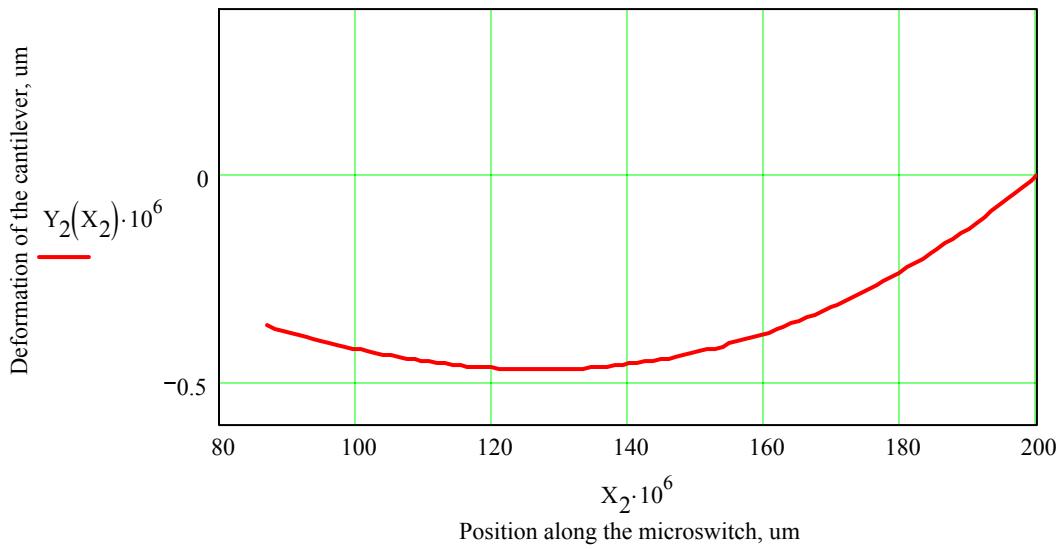

Fig. A.16. Deformations of section-2 of the cantilever as a function of position along the microswitch, after contact is made.

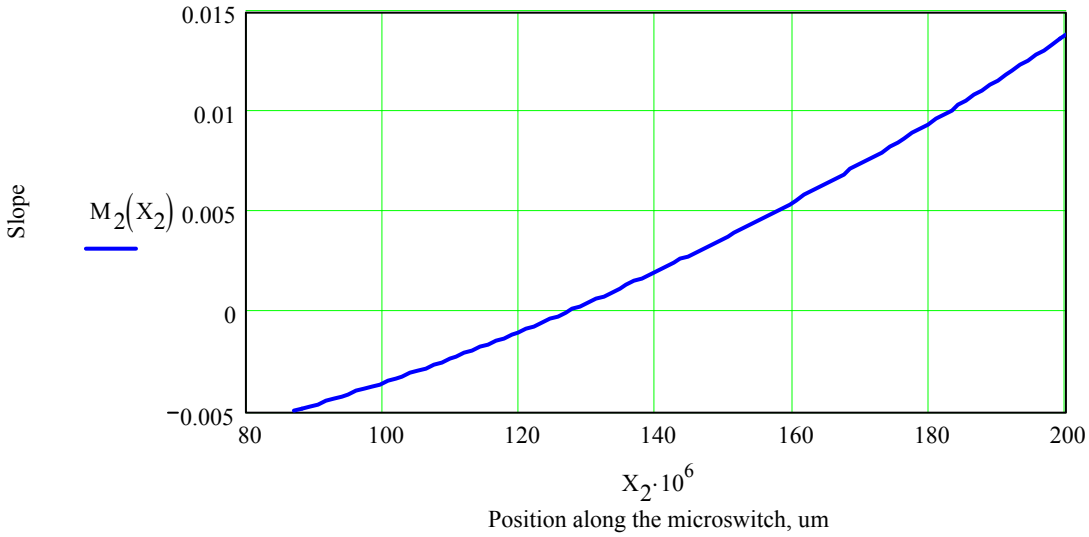

Fig. A.17. Slope of section-2 of the cantilever as a function of position along the microswitch, after contact is made.

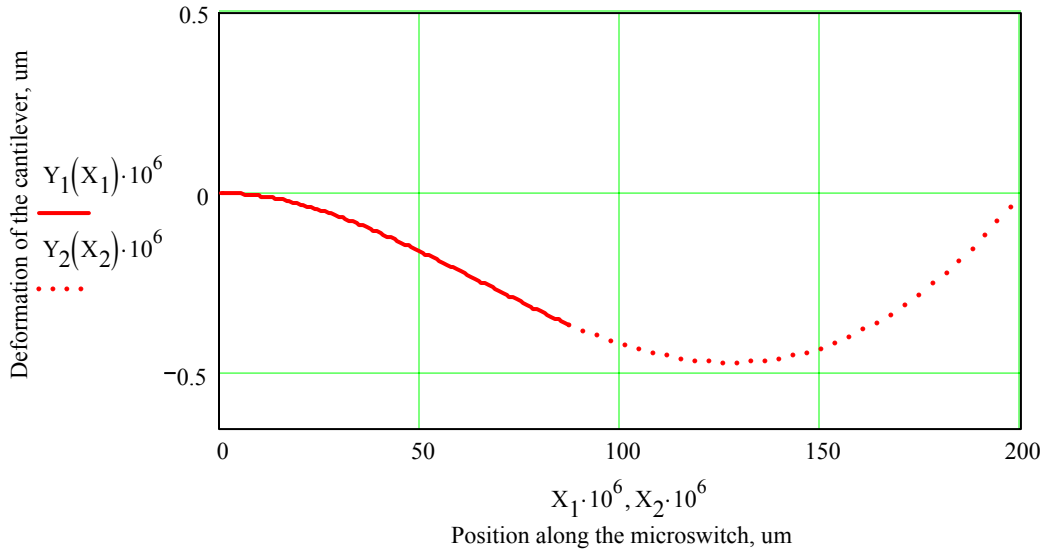

Fig. A.18. Deformations of the entire cantilever as a function of position along the microswitch, after contact is made.

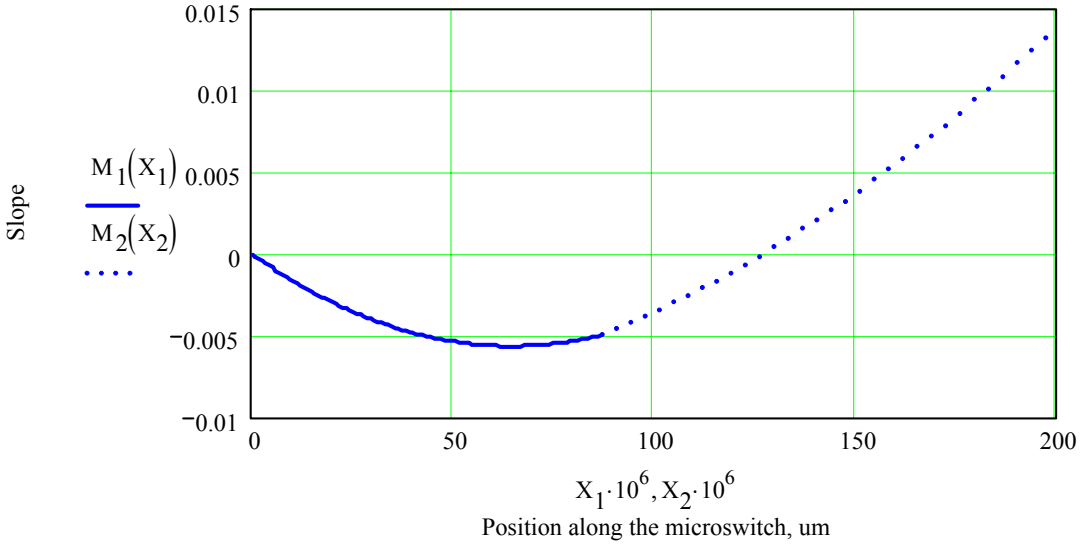

Fig. A.19. Slope of the entire cantilever as a function of position along the microswitch, after contact is made.

When we consider bending of the cantilever and motion of its free end to close the gap d_g so that contacts are made between the shorting bar and the traces, Eq. A.60 becomes

$$R_A = F\left(12\frac{{L_1}^2}{L^2} - 6\frac{L_1}{L} - 5\frac{{L_1}^3}{L^3}\right) + \frac{EI}{L^3}6\times10^{-6} \quad . \tag{A.65}$$

Equation A.65 is a result of simultaneously solving all the deformation and slope equations while applying one new boundary condition. The changed boundary condition is

$$\text{at} \qquad X_2 = L \qquad\qquad Y_2 = 1\times10^{-6} \quad , \tag{A.66}$$

because the simply supported end of the cantilever is now the gap distance d_g lower than the fixed end. For that reason, an additional term of $1\times10^{-6}\,EI$ is produced. As Eq. A.50, which utilizes the boundary condition from Eq. A.66, is solved for R_A, all terms are divided by L^3, and then multiplied by 6 in order to simplify the equation.

Substituting Eq. A.65 in place of Eq. A.60 into Eqs A.49 and A.50 we obtain deformations and slope of the cantilever for the new boundary condition. The new results are shown in Figs A.20 to A.25.

Response of the cantilever to force magnitudes different than that required to close the gap was also studied. Deformations of the cantilever were found for the following four values of the force:

$$F_1 = 6.44\,\mu\text{N} \quad , \tag{A.67}$$

$$F_2 = 2F_1\,\mu\text{N} \quad , \tag{A.68}$$

$$F_3 = 3F_1\,\mu\text{N} \quad , \tag{A.69}$$

and

$$F_4 = 4F_1\,\mu\text{N} \quad . \tag{A.70}$$

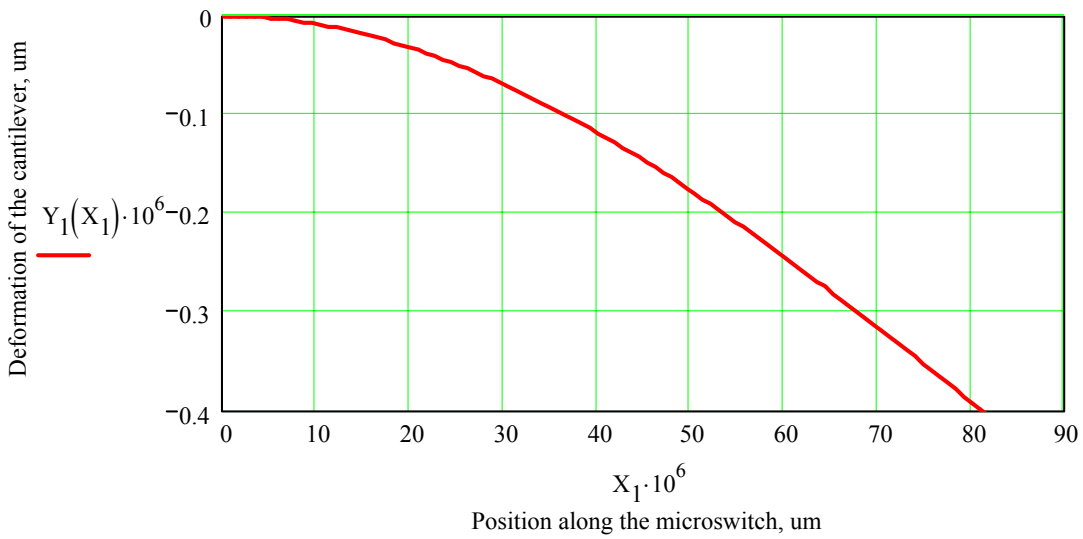

Fig. A.20. Deformations of section-1 of the cantilever as a function of position along the microswitch, after contact is made by closing the gap $d_g = 1\mu m$.

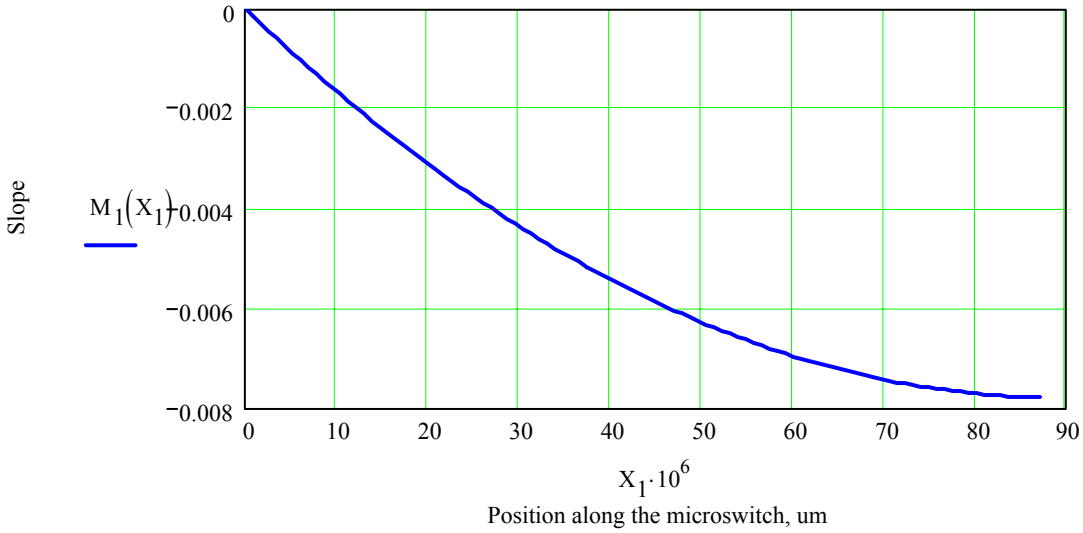

Fig. A.21. Slope of section-1 of the cantilever as a function of position along the microswitch, after contact is made by closing the gap $d_g = 1\mu m$.

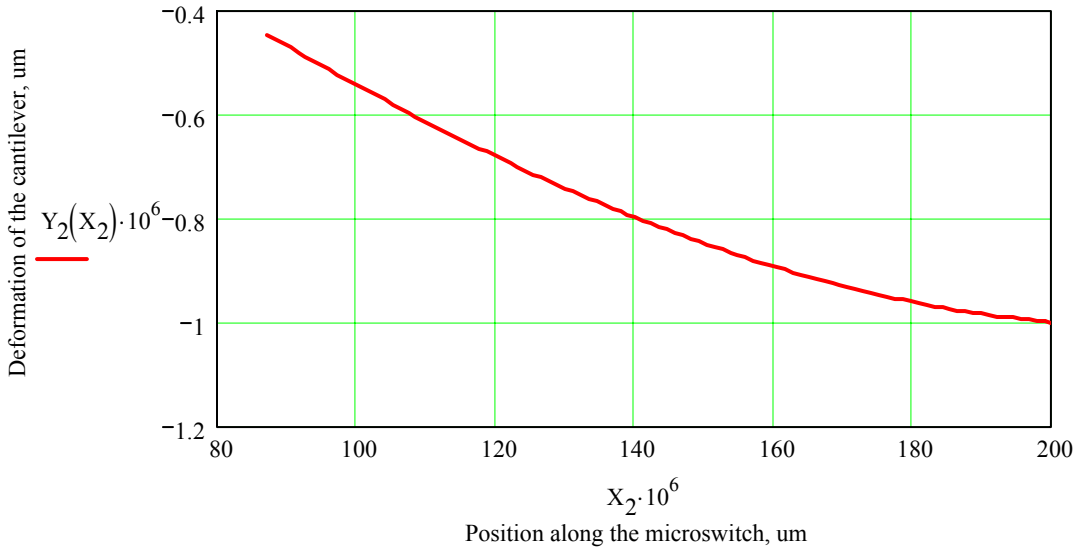

Fig. A.22. Deformations of section-2 of the cantilever as a function of position along the microswitch, after contact is made by closing the gap $d_g = 1\mu m$.

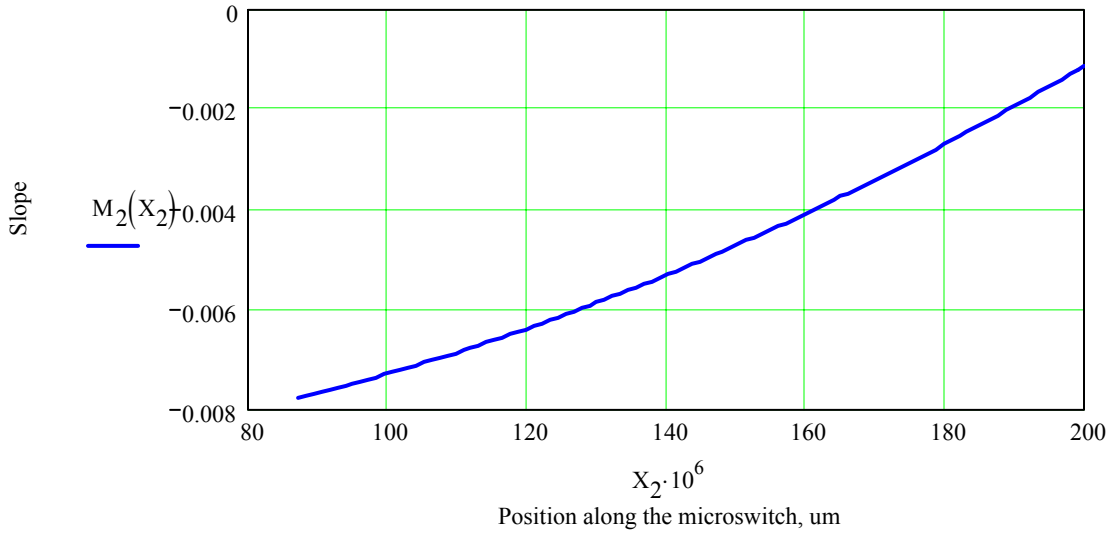

Fig. A.23. Slope of section-2 of the cantilever as a function of position along the microswitch, after contact is made by closing the gap $d_g = 1\mu m$.

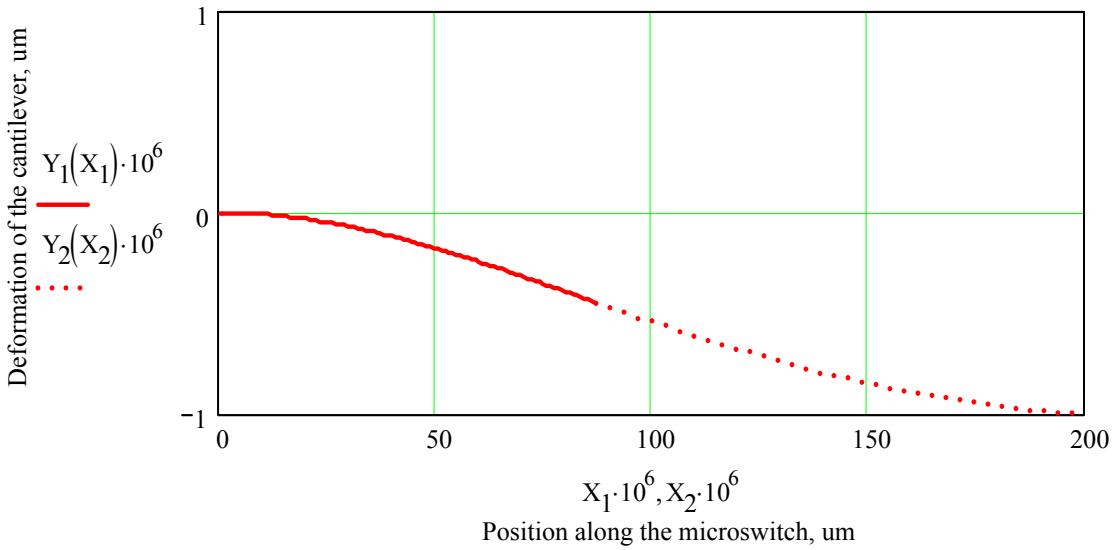

Fig. A.24. Deformations of the entire cantilever as a function of position along the microswitch, after contact is made by closing the gap d_g = 1μm.

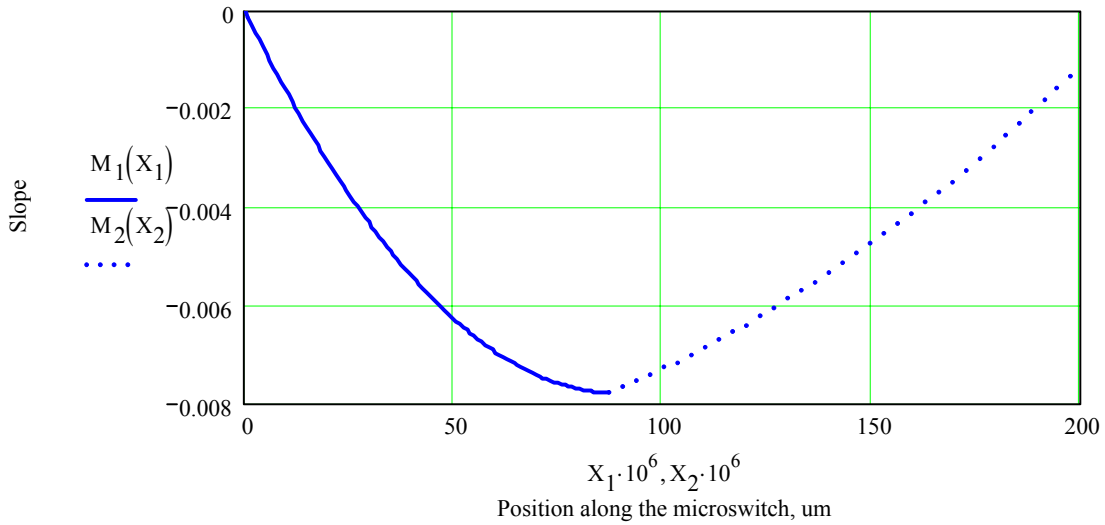

Fig. A.25. Slope of the entire cantilever as a function of position along the microswitch, after contact is made by closing the gap d_g = 1μm.

Forces defined by Eqs A.67 to A.70 were substituted into Eq. A.65 to obtain

$$R_{A1} = F_1\left(12\frac{{L_1}^2}{L^2} - 6\frac{L_1}{L} - 5\frac{{L_1}^3}{L^3}\right) + \frac{EI}{L^3}6\times10^{-6} \quad , \tag{A.71}$$

$$R_{A2} = F_2\left(12\frac{{L_1}^2}{L^2} - 6\frac{L_1}{L} - 5\frac{{L_1}^3}{L^3}\right) + \frac{EI}{L^3}6\times10^{-6} \quad , \tag{A.72}$$

$$R_{A3} = F_3\left(12\frac{{L_1}^2}{L^2} - 6\frac{L_1}{L} - 5\frac{{L_1}^3}{L^3}\right) + \frac{EI}{L^3}6\times10^{-6} \quad , \tag{A.73}$$

and

$$R_{A4} = F_4\left(12\frac{{L_1}^2}{L^2} - 6\frac{L_1}{L} - 5\frac{{L_1}^3}{L^3}\right) + \frac{EI}{L^3}6\times10^{-6} \quad . \tag{A.74}$$

Substituting Eqs A.71 to A.74 into Eqs A.61 and A.63, the following equations, representing deformations of section-1 and section-2 of the cantilever due to each force were obtained:

$$Y_{11}(X_1) = \frac{1}{EI}\left(\frac{1}{6}F_1{X_1}^3 - \frac{1}{2}F_1L{X_1}^2 + \frac{1}{2}F_1L_1{X_1}^2 - \frac{1}{6}R_{A1}{X_1}^3\right) \quad , \tag{A.75}$$

$$Y_{21}(X_2) = \frac{1}{EI}\left(-\frac{1}{6}R_{A1}{X_2}^3 + \frac{3}{2}F_1{L_1}^2X_2 - F_1LL_1X_2 - \frac{5}{6}F_1{L_1}^3 + \frac{1}{2}F_1L{L_1}^2\right) \quad , \tag{A.76}$$

$$Y_{12}(X_1) = \frac{1}{EI}\left(\frac{1}{6}F_2{X_1}^3 - \frac{1}{2}F_2L{X_1}^2 + \frac{1}{2}F_2L_1{X_1}^2 - \frac{1}{6}R_{A2}{X_1}^3\right) \quad , \tag{A.77}$$

$$Y_{22}(X_2) = \frac{1}{EI}\left(-\frac{1}{6}R_{A2}{X_2}^3 + \frac{3}{2}F_2{L_1}^2X_2 - F_2LL_1X_2 - \frac{5}{6}F_2{L_1}^3 + \frac{1}{2}F_2L{L_1}^2\right) \quad , \tag{A.78}$$

$$Y_{13}(X_1) = \frac{1}{EI}\left(\frac{1}{6}F_3 {X_1}^3 - \frac{1}{2}F_3 L {X_1}^2 + \frac{1}{2}F_3 L_1 {X_1}^2 - \frac{1}{6}R_{A3} {X_1}^3\right) \quad , \tag{A.79}$$

$$Y_{23}(X_2) = \frac{1}{EI}\left(-\frac{1}{6}R_{A3} {X_2}^3 + \frac{3}{2}F_3 {L_1}^2 X_2 - F_3 L L_1 X_2 - \frac{5}{6}F_3 {L_1}^3 + \frac{1}{2}F_3 L {L_1}^2\right) \quad , \tag{A.80}$$

$$Y_{14}(X_1) = \frac{1}{EI}\left(\frac{1}{6}F_4 {X_1}^3 - \frac{1}{2}F_4 L {X_1}^2 + \frac{1}{2}F_4 L_1 {X_1}^2 - \frac{1}{6}R_{A4} {X_1}^3\right) \quad , \tag{A.81}$$

and

$$Y_{24}(X_2) = \frac{1}{EI}\left(-\frac{1}{6}R_{A4} {X_2}^3 + \frac{3}{2}F_4 {L_1}^2 X_2 - F_4 L L_1 X_2 - \frac{5}{6}F_4 {L_1}^3 + \frac{1}{2}F_4 L {L_1}^2\right) \quad . \tag{A.82}$$

Deformations of the cantilever, based on from Eqs A.75 to A.82, as functions of position along the microswitch are shown in Fig. A.26.

Friction force at the contacts of the microswitch was also studied. To find trends in friction force behavior, the following range of friction coefficients from Beer and Johnston (1999) was used:

$$\mu = 0.15, 0.155 \ldots 0.6 \quad . \tag{A.83}$$

In order to find the slip forces, slope (i.e. angle) of the cantilever at the point of contact, Fig. A.27, was determined for all four forces considered. The slope was found by evaluating Eq. A.64 at $X_2 = L$ for each of the four forces found in Eqs A.67 to A.70. The resulting equations are

$$M_{21}(L) = \Theta_1 = -\frac{1}{EI}\left(\frac{1}{2}R_{A1} {X_2}^2 + \frac{3}{2}F_1 {L_1}^2 - F_1 L L_1\right) \quad , \tag{A.84}$$

$$M_{22}(L) = \Theta_2 = -\frac{1}{EI}\left(\frac{1}{2}R_{A2}X_2{}^2 + \frac{3}{2}F_2L_1{}^2 - F_2LL_1\right) \quad , \tag{A.85}$$

$$M_{23}(L) = \Theta_3 = -\frac{1}{EI}\left(\frac{1}{2}R_{A3}X_2{}^2 + \frac{3}{2}F_3L_1{}^2 - F_3LL_1\right) \quad , \tag{A.86}$$

and

$$M_{24}(L) = \Theta_4 = -\frac{1}{EI}\left(\frac{1}{2}R_{A4}X_2{}^2 + \frac{3}{2}F_4L_1{}^2 - F_4LL_1\right) \quad . \tag{A.87}$$

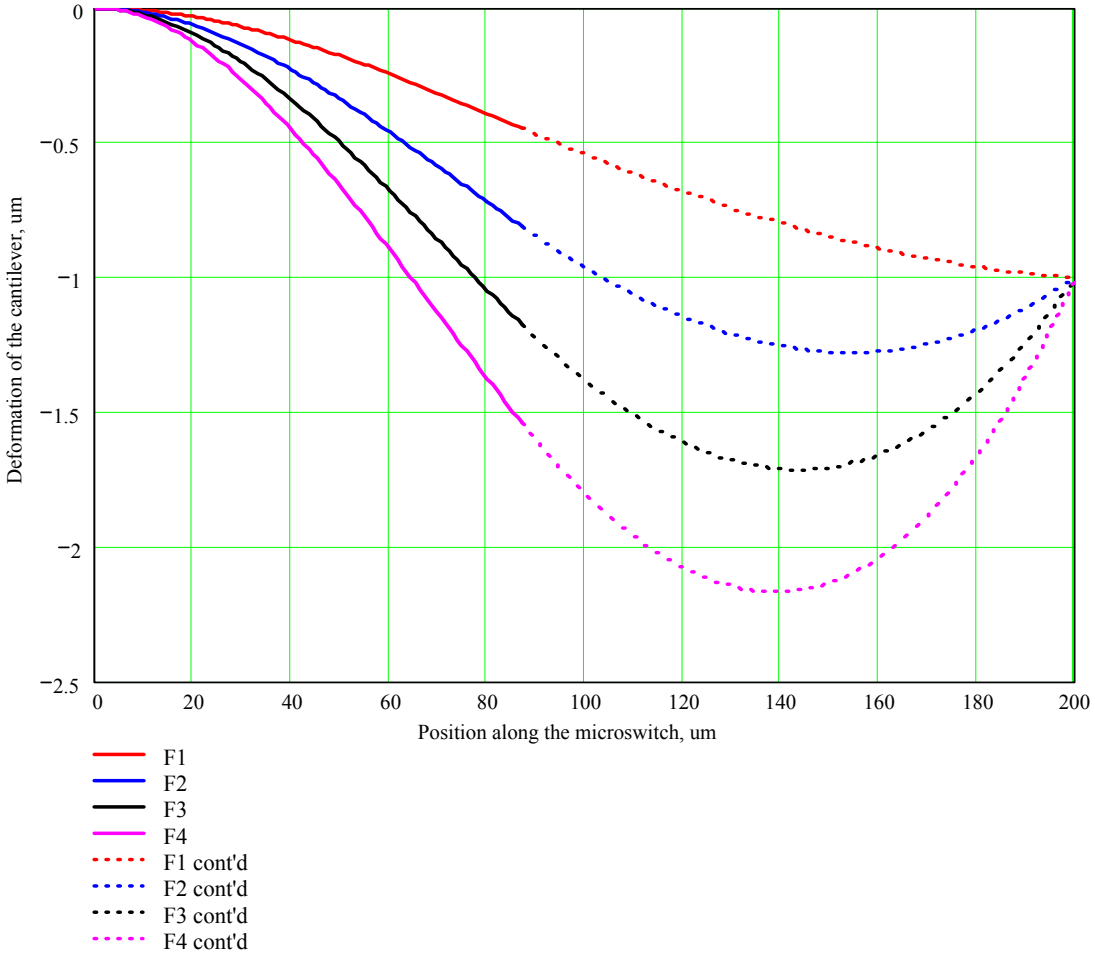

Fig. A.26. Deformations of the cantilever as functions of position along the microswitch, after contact is made by closing the gap d_g = 1μm, for different magnitudes of the actuation force.

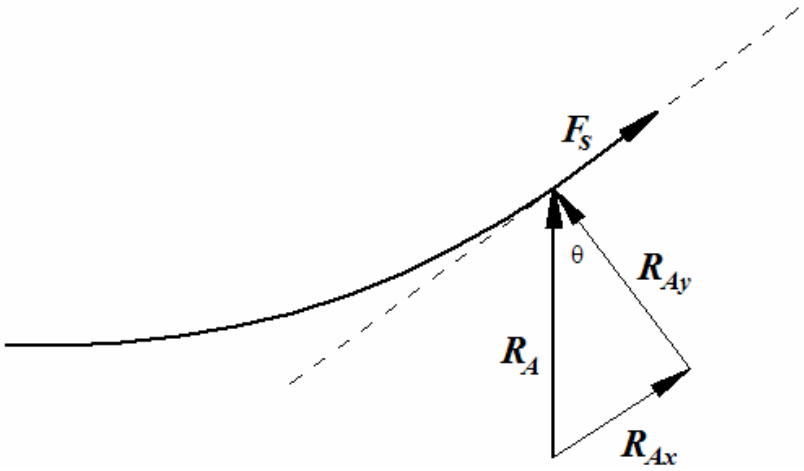

Fig. A.27. Slip force at the end of the cantilever.

The slip forces at the simply supported end of the cantilever can be found using the friction force equations. The friction force equation is written as

$$F_S = \mu F_n \quad , \tag{A.88}$$

where μ is the coefficient of friction and F_n is the normal force, perpendicular to F_S. The slip forces at the contact end of the microswitch for the four forces considered are

$$F_{S1}(\mu) = \mu R_{A1} \cos(\Theta_1) \quad , \tag{A.89}$$

$$F_{S2}(\mu) = \mu R_{A2} \cos(\Theta_2) \quad , \tag{A.90}$$

$$F_{S3}(\mu) = \mu R_{A3} \cos(\Theta_3) \quad , \tag{A.91}$$

and

$$F_{S4}(\mu) = \mu R_{A4} \cos(\Theta_4) \quad . \tag{A.92}$$

The slip forces as functions of coefficient of friction along the microswitch are shown in Fig. A.28.

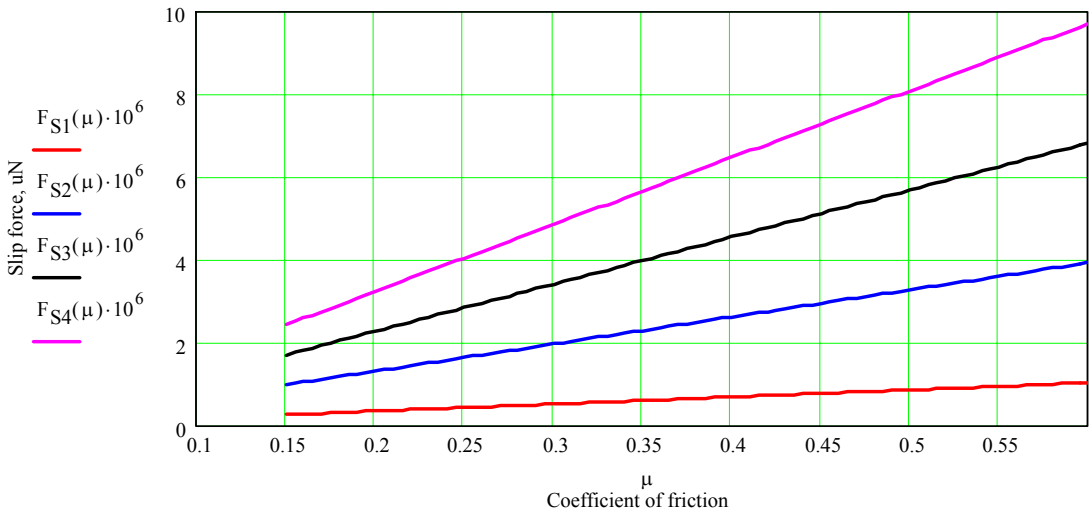

Fig. A.28. Slip forces as functions of coefficient of friction for F1, F2, F3, and F4.

Additional analysis, based on Section 3.1.1, was performed. The equation for electrostatic force

$$F = -\frac{1}{2}\frac{\varepsilon_o \varepsilon_r L_e b_e V^2}{{d_e}^2} \tag{A.93}$$

can be solved for the actuation voltage necessary to produce the electrostatic force needed to close the gap d_g, i.e.,

$$V = \sqrt{2\frac{F{d_e}^2}{\varepsilon_o \varepsilon_r L_e b_e}} \quad , \tag{A.94}$$

or

$$V = 57.229 \text{ V} \quad . \tag{A.95}$$

The spring constant can be calculated as

$$k = \frac{1}{2}\frac{\varepsilon_o \varepsilon_r L_e b_e V^2}{d_g {d_e}^2} \quad , \tag{A.96}$$

or

$$k = 6.441 \frac{\mathrm{N}}{\mathrm{m}} \quad . \tag{A.97}$$

Following the procedure described in Section 3.1.1, the fundamental natural frequency of the cantilever, considered in this thesis, can be determined based on its dynamic mass. The dynamic mass of the cantilever can be found to be

$$m = \frac{33}{140} \rho b h L \quad , \tag{A.98}$$

or

$$m = 5.492 \times 10^{-9} \quad \mathrm{g} \quad . \tag{A.99}$$

The natural frequency of the cantilever can be determined as

$$f_o = \frac{1}{2\pi} \sqrt{\frac{k}{m}} \quad , \tag{A.100}$$

or

$$f_o \times 10^{-6} = 0.172 \ \mathrm{MHz} \quad . \tag{A.101}$$

The results obtained using Eqs A.93 to A.103 agree with the information obtained during background research for this thesis. The voltage value obtained from Eq. A.95 is in the RF MEMS switch operational voltage ranges (Yao and Chang, 1995; Brown, 1998). Similarly, the natural frequency of the cantilever satisfies one of the requirements for a good microswitch design (Li, et al., 1999; Zou, et al., 2000).

APPENDIX B. CALCULATIONS OF TEMPERATURE

Equations used in calculating thermal behavior of the microswitch are based on the following parameters:

current:	$I = 300\times10^{-3}$	$\delta I = 0.5\times10^{-3}$ A	
ambient temperature:	$T_\infty = 298$	$\delta T_\infty = 2$	K
contact resistance:	$R = 1$	$\delta R = 0.1$	Ω
Lorenz number for gold:	$L_r = 2.4\times10^{-8}$	$\delta L_r = 0.05\times10^{-8}$	
TAS temperature:	$T_{TAS} = 989.8$	K .	

The voltage-temperature relation in metallic constrictions can be used to calculate the maximum operating temperature of the microswitch. In order to find this temperature voltage was calculated according to Ohm's law, i.e.,

$$V = IR \quad , \tag{B.1}$$

$$V = 0.3\,\mathrm{V} \quad . \tag{B.2}$$

The voltage-temperature relation in metallic constrictions, based on experimental observations, is written as (Reid and Starman, 2003)

$$T_w{}^2 - T_\infty{}^2 = \frac{V^2}{4L_r} \quad . \tag{B.3}$$

When Eq. B.3 is evaluated for T_w, which represents the maximum operating temperature of the microswitch, we obtain

$$T_w = \sqrt{\frac{V^2}{4L_r} + T_\infty{}^2} \quad , \tag{B.4}$$

$$T_w = 1.013\times10^3\,\mathrm{K} \quad . \tag{B.5}$$

The maximum temperature of the microswitch was calculated to be 1013°K, while the results obtained from TAS, Section 4.2.2, showed a maximum temperature of the microswitch as 716°C or 989°K. In order to find out if the temperature obtained from the voltage temperature relation in metallic constrictions is in acceptable correlation with the TAS results, an uncertainty analysis had to be performed.

The maximum temperature of the microswitch obtained from the voltage-temperature relation depends on three individual parameters: voltage, Lorenz number, and ambient temperature, i.e., $T_w(V, L_r, T_\infty)$. However voltage itself depends on the electrical current and the resistance, i.e., $V = V(I, R)$. The uncertainty equation for voltage can be then written as

$$\delta V = \left[\left(\frac{\partial V}{\partial I} \delta I \right)^2 + \left(\frac{\partial V}{\partial R} \delta R \right)^2 \right]^{\frac{1}{2}} \quad , \tag{B.6}$$

where the partial derivatives are

$$\frac{\partial V}{\partial I} = R \tag{B.7}$$

and

$$\frac{\partial V}{\partial R} = I \quad . \tag{B.8}$$

Substituting Eqs B.7 and B.8 into Eq. B.6, we obtain

$$\delta V = \left[(R \cdot \delta I)^2 + (I \cdot \delta R)^2 \right]^{\frac{1}{2}} \quad . \tag{B.9}$$

General uncertainty equation for the temperature, based on its phenomenological equation, is

$$\delta T_w = \left[\left(\frac{\partial T_w}{\partial V} \delta V \right)^2 + \left(\frac{\partial T_w}{\partial L_r} \delta L_r \right)^2 + \left(\frac{\partial T_w}{\partial T_\infty} \delta T_\infty \right)^2 \right]^{\frac{1}{2}} \quad , \tag{B.10}$$

where the partial derivatives are

$$\frac{\partial T_w}{\partial V} = \frac{1}{4} \frac{V}{L_r} \left(\frac{V^2}{4L_r} + T_\infty \right)^{-\frac{1}{2}} \quad , \tag{B.11}$$

$$\frac{\partial T_w}{\partial L_r} = -\frac{1}{8} \frac{V^2}{{L_r}^2} \left(\frac{V^2}{4L_r} + {T_\infty}^2 \right)^{-\frac{1}{2}} \quad , \tag{B.12}$$

and

$$\frac{\partial T_w}{\partial T_\infty} = T_\infty \left(\frac{V^2}{4L_r} + {T_\infty}^2 \right)^{-\frac{1}{2}} \quad . \tag{B.13}$$

Substitution of Eqs. B.11 and B.13 into Eq. B.10, yields overall uncertainty in T_w

$$\delta Tw = \left\{ \left[\frac{1}{4} \frac{V}{L_r} \left(\frac{V^2}{4L_r} + {T_\infty}^2 \right)^{-\frac{1}{2}} \delta V \right]^2 + \left[-\frac{1}{8} \frac{V^2}{{L_r}^2} \left(\frac{V^2}{4L_r} + {T_\infty}^2 \right)^{-\frac{1}{2}} \delta L_r \right]^2 + \left[T_\infty \left(\frac{V^2}{4L_r} + {T_\infty}^2 \right)^{-\frac{1}{2}} \delta T_\infty \right]^2 \right\}^{\frac{1}{2}} \tag{B.14}$$

or

$$\delta T_w = 99.056 \, \mathrm{K} \quad . \tag{B.15}$$

To calculate percent overall uncertainty the following equation is used

$$\%\delta T_w = \frac{\delta T_w}{T_w} 100 \quad , \tag{B.16}$$

resulting in

$$\%\delta T_w = 9.189\ \% \quad , \tag{B.17}$$

In order to find out which parameter has the greatest effect on the overall uncertainty in the maximum operating temperature of the microswitch percent contributions of the individual components were calculated according to the following equations:

$$\%\delta T_w \delta V = \frac{\left[\frac{1}{4}\frac{V}{L_r}\left(\frac{V^2}{4L_r} + {T_\infty}^2\right)^{-\frac{1}{2}}\delta V\right]^2}{(\delta T_w)^2} 100 \quad , \tag{B.18}$$

$$\%\delta T_w \delta V = 98.923\ \% \quad , \tag{B.19}$$

$$\%\delta T_w \delta L_r = \frac{\left[-\frac{1}{8}\frac{V^2}{{L_r}^2}\left(\frac{V^2}{4L_r} + {T_\infty}^2\right)^{-\frac{1}{2}}\delta L_r\right]^2}{(\delta T_w)^2} 100 \quad , \tag{B.20}$$

$$\%\delta T_w \delta L_r = 1.073\ \% \quad , \tag{B.21}$$

$$\%\delta T_w \delta T_\infty = \frac{\left[T_\infty\left(\frac{V^2}{4L_r} + {T_\infty}^2\right)^{-\frac{1}{2}}\delta T_\infty\right]^2}{(\delta T_w)^2} 100 \quad , \tag{B.22}$$

and

$$\%\delta T_w \delta T_\infty = 3.997 \times 10^{-3}\ \% \quad . \tag{B.23}$$

In order to check if the calculations of the individual percent contributions are correct, the results of Eqs B.18 to B.23 were summed to verify that they add to 100%

$$\%\delta T_w \delta V + \%\delta T_w \delta L_r + \%\delta T_w \delta T_\infty = 100 \quad . \tag{B.24}$$

Voltage was calculated to be the greatest contributor to the overall uncertainty in the maximum operating temperature of the microswitch. Since voltage is a parameter that depends on the individual uncertainties of electrical current and contact resistance, further analysis was performed. The percent contribution to the overall uncertainty in voltage was calculated using the following equations:

$$\%\delta V \delta I = \frac{(R\delta I)^2}{(\delta V)^2} 100 \quad , \tag{B.25}$$

resulting in

$$\%\delta V \delta I = 0.028\ \% \quad , \tag{B.26}$$

and

$$\%\delta V \delta R = \frac{(I\delta R)^2}{(\delta V)^2} 100 \quad , \tag{B.27}$$

resulting in

$$\%\delta V \delta R = 99.972\ \% \quad . \tag{B.28}$$

The greatest contributor to the overall uncertainty in voltage is the uncertainty in contact resistance. The value of the uncertainty in contact resistance used in this analysis is equal to 10% of the nominal value of contact resistance. In order to decrease the uncertainty value in the contact resistance more sophisticated fabrication processes should be used.

In order to find the percent difference between the maximum TAS temperature and the temperature of the microswitch based on the voltage-temperature relation, the following equation was utilized:

$$\%T_{Diff} = \left(\frac{T_{TAS} - T_w}{T_{TAS}} \right) \cdot 100 \quad , \tag{B.29}$$

$$\%T_{Diff} = 2.351\,\% \qquad . \tag{B.30}$$

Based on the results shown in Eqs B.1 to B.30, we conclude that the temperature obtained by using the voltage-temperature relation in metallic constrictions correlates well with the TAS results, since they agree to within the uncertainty limits.

APPENDIX C. UNCERTAINTY ANALYSIS

An uncertainty analysis had to be perfumed in order to find out how good are the results defining deformations of the cantilever. The uncertainty analysis was done for deformations of section-1 and section-2 of the cantilever, which are expressed, based on the derivations presented in Appendix A, as follows:

$$Y_1(X_1) = \frac{1}{EI}\left(\frac{1}{6}FX_1^{\,3} - \frac{1}{2}FLX_1^{\,2} + \frac{1}{2}FL_1X_1^{\,2} - \frac{1}{6}R_AX_1^{\,3}\right) \tag{C.1}$$

and

$$Y_2(X_2) = \frac{1}{EI}\left(-\frac{1}{6}R_AX_2^{\,3} + \frac{3}{2}FL_1^{\,2}X_2 - FLL_1X_2 - \frac{5}{6}FL_1^{\,3} + \frac{1}{2}FLL_1^{\,2}\right) \quad , \tag{C.2}$$

where

$$L_1 = L_o + \frac{1}{2}L_e \tag{C.3}$$

and

$$R_A = F\left(12\frac{L_1^{\,2}}{L^2} - 6\frac{L_1}{L} - 5\frac{L_1^{\,3}}{L^3}\right) + \frac{EI}{L^3}6\times10^{-6} \quad . \tag{C.4}$$

In order to calculate the overall uncertainty of the deformations for both sections of the cantilever, the individual uncertainties of L_1 and R_A had to be calculated, because L_1 is a function of L_o and L_e, and R_A is a function of L, L_1, E, and I. The moment of inertia is also dependent on the width, b, and thickness, h, of the cantilever. The uncertainty in L_1 can be written as

$$\delta L_1 = \left[\left(\frac{\partial L_1}{\partial L_o}\delta L_o\right)^2 + \left(\frac{\partial L_1}{\partial L_e}\delta L_e\right)^2\right]^{\frac{1}{2}} \quad . \tag{C.5}$$

When partial derivatives

$$\frac{\partial L_1}{\partial L_o} = 1 \tag{C.6}$$

and

$$\frac{\partial L_1}{\partial L_e} = \frac{1}{2} \tag{C.7}$$

are substituted into Eq. C.5 we obtain

$$\delta L_1 = \left[\left(\delta L_o\right)^2 + \left(\frac{1}{2} \delta L_e \right)^2 \right]^{\frac{1}{2}} \quad . \tag{C.8}$$

The moment of inertia equation for the cantilever considered in this thesis can be written as

$$I = \frac{1}{12} b h^3 \tag{C.9}$$

and the uncertainty in I can be written as

$$\delta I = \left[\left(\frac{\partial I}{\partial b} \delta b \right)^2 + \left(\frac{\partial I}{\partial h} \delta h \right)^2 \right]^{\frac{1}{2}} \quad . \tag{C.10}$$

When the partial derivatives

$$\frac{\partial I}{\partial b} = \frac{1}{12} h^3 \tag{C.11}$$

and

$$\frac{\partial I}{\partial h} = \frac{1}{4} b\, h^2 \tag{C.12}$$

are substituted into Eq. C.10 we obtain

$$\delta I = \left[\left(\frac{1}{12} h^3 \delta b \right)^2 + \left(\frac{1}{4} b\, h^2 \delta h \right)^2 \right]^{\frac{1}{2}} \quad . \tag{C.13}$$

Having calculated the uncertainty in the moment of inertia, the uncertainty in R_A can be found using equation

$$\delta R_A = \left[\left(\frac{\partial R_A}{\partial L_1} \delta L_1 \right)^2 + \left(\frac{\partial R_A}{\partial L} \delta L \right)^2 + \left(\frac{\partial R_A}{\partial E} \delta E \right)^2 + \left(\frac{\partial R_A}{\partial I} \delta I \right)^2 \right]^{\frac{1}{2}} \quad . \tag{C.14}$$

Force was omitted from the uncertainty calculations because it was an assumed value, therefore it had uncertainty of magnitude zero. When the partial derivatives

$$\frac{\partial R}{\partial L_1} = 24F \frac{L_1}{L^2} - 6F \frac{1}{L} - 15F \frac{{L_1}^2}{L^3} \quad , \tag{C.15}$$

$$\frac{\partial R}{\partial L} = -24F \frac{{L_1}^2}{L^3} + 6F \frac{L_1}{L^2} + 15F \frac{{L_1}^3}{L^4} - \frac{EI}{L^4} 18 \times 10^{-6} \quad , \tag{C.16}$$

$$\frac{\partial R}{\partial E} = 6 \times 10^{-6} \frac{I}{L^3} \quad , \tag{C.17}$$

and

$$\frac{\partial R}{\partial E} = 6 \times 10^{-6} \frac{E}{L^3} \quad , \tag{C.18}$$

are substituted into Eq. C.14 we obtain

$$\delta R_A = \left\{ \left[\left(24F\frac{L_1}{L^2} - 6F\frac{1}{L} - 15F\frac{{L_1}^2}{L^3} \right)\delta L_1 \right]^2 + \right.$$
$$\left[\left(-24F\frac{{L_1}^2}{L^3} + 6F\frac{L_1}{L^2} + 15F\frac{{L_1}^3}{L^4} - \frac{EI}{L^4}18\times10^{-6} \right)\delta L \right]^2 + \quad . \tag{C.19}$$
$$\left. \left(6\times10^{-6}\frac{I}{L^3}\delta E \right)^2 + \left(6\times10^{-6}\frac{E}{L^3}\delta I \right)^2 \right\}^{\frac{1}{2}}$$

Finally, the uncertainty of the deformations of section-1 can be calculated with the following equation

$$\delta Y_1 = \left[\left(\frac{\partial Y_1}{\partial E}\delta E \right)^2 + \left(\frac{\partial Y_1}{\partial I}\delta I \right)^2 + \left(\frac{\partial Y_1}{\partial R_A}\delta R_A \right)^2 + \left(\frac{\partial Y_1}{\partial X_1}\delta X_1 \right)^2 + \right.$$
$$\left. \left(\frac{\partial Y_1}{\partial L_1}\delta L_1 \right)^2 + \left(\frac{\partial Y_1}{\partial L}\delta L \right)^2 \right]^{\frac{1}{2}} \quad . \tag{C.20}$$

When the partial derivatives

$$\frac{\partial Y_1}{\partial E} = -\frac{1}{E^2 I}\left(\frac{1}{6}F{X_1}^3 - \frac{1}{2}FL{X_1}^2 + \frac{1}{2}FL_1{X_1}^2 - \frac{1}{6}R_A{X_1}^3 \right) \quad , \tag{C.21}$$

$$\frac{\partial Y_1}{\partial I} = -\frac{1}{EI^2}\left(\frac{1}{6}F{X_1}^3 - \frac{1}{2}FL{X_1}^2 + \frac{1}{2}FL_1{X_1}^2 - \frac{1}{6}R_A{X_1}^3 \right) \quad , \tag{C.22}$$

$$\frac{\partial Y_1}{\partial R_A} = \frac{1}{EI}\left(-\frac{1}{6}{X_1}^3 \right) \quad , \tag{C.23}$$

$$\frac{\partial Y_1}{\partial X_A} = \frac{1}{EI}\left(\frac{1}{2}F{X_1}^2 - FLX_1 + FL_1X_1 - \frac{1}{2}R_A{X_1}^2 \right) \quad , \tag{C.24}$$

$$\frac{\partial Y_1}{\partial L_1} = \frac{1}{EI}\left(\frac{1}{2}F{X_1}^2 \right) \quad , \tag{C.25}$$

and

$$\frac{\partial Y_1}{\partial L} = \frac{1}{EI}\left(-\frac{1}{2}FX_1{}^2\right) \tag{C.26}$$

are substituted into Eq. C.20, it becomes

$$\begin{aligned}\delta Y_1 = \Bigg\{ & \left[-\frac{1}{E^2 I}\left(\frac{1}{6}FX_1{}^3 - \frac{1}{2}FLX_1{}^2 + \frac{1}{2}FL_1X_1{}^2 - \frac{1}{6}R_AX_1{}^3\right)\delta E\right]^2 + \\ & \left[-\frac{1}{EI^2}\left(\frac{1}{6}FX_1{}^3 - \frac{1}{2}FLX_1{}^2 + \frac{1}{2}FL_1X_1{}^2 - \frac{1}{6}R_AX_1{}^3\right)\delta I\right]^2 + \\ & \left[\frac{1}{EI}\left(-\frac{1}{6}X_1{}^3\right)\delta R_A\right]^2 + \\ & \left[\frac{1}{EI}\left(\frac{1}{2}FX_1{}^2 - FLX_1 + FL_1X_1 - \frac{1}{2}R_AX_1{}^2\right)\delta X_1\right]^2 + \\ & \left[\frac{1}{EI}\left(\frac{1}{2}FX_1{}^2\right)\delta L_1\right]^2 + \left[\frac{1}{EI}\left(-\frac{1}{2}FX_1{}^2\right)\delta L\right]^2\Bigg\}^{\frac{1}{2}}\end{aligned} \tag{C.27}$$

Similarly, the uncertainty in deformations of section-2 can be found using equation

$$\begin{aligned}\delta Y_2 = \Bigg[& \left(\frac{\partial Y_2}{\partial E}\delta E\right)^2 + \left(\frac{\partial Y_2}{\partial I}\delta I\right)^2 + \left(\frac{\partial Y_2}{\partial R_A}\delta R_A\right)^2 + \left(\frac{\partial Y_2}{\partial X_2}\delta X_2\right)^2 + \\ & \left(\frac{\partial Y_2}{\partial L_1}\delta L_1\right)^2 + \left(\frac{\partial Y_2}{\partial L}\delta L\right)^2\Bigg]^{\frac{1}{2}}\end{aligned} \tag{C.28}$$

As the partial derivatives

$$\frac{\partial Y_2}{\partial E} = -\frac{1}{E^2 I}\left(-\frac{1}{6}R_AX_2{}^3 + \frac{3}{2}FL_1{}^2X_2 - F\,LL_1X_2 - \frac{5}{6}FL_1{}^3 + \frac{1}{2}F\,L\,L_1{}^2\right) \quad , \tag{C.29}$$

$$\frac{\partial Y_2}{\partial I} = -\frac{1}{EI^2}\left(-\frac{1}{6}R_AX_2{}^3 + \frac{3}{2}FL_1{}^2X_2 - F\,LL_1X_2 - \frac{5}{6}FL_1{}^3 + \frac{1}{2}F\,L\,L_1{}^2\right) \quad , \tag{C.30}$$

$$\frac{\partial Y_2}{\partial R_A} = \frac{1}{EI}\left(-\frac{1}{6}X_2{}^3\right) \quad , \tag{C.31}$$

$$\frac{\partial Y_2}{\partial X_2} = \frac{1}{EI}\left(-\frac{1}{2} R_A {X_2}^2 + \frac{3}{2} F {L_1}^2 - F\, L L_1 \right) \quad , \tag{C.32}$$

$$\frac{\partial Y_2}{\partial L_1} = \frac{1}{EI}\left(3 F L_1 X_2 - F\, L X_2 - \frac{5}{2} F {L_1}^2 + F\, L\, L_1 \right) \quad , \tag{C.33}$$

and

$$\frac{\partial Y_2}{\partial L} = \frac{1}{EI}\left(-F\, L_1 X_2 + \frac{1}{2} F\ {L_1}^2 \right) \quad , \tag{C.34}$$

are substituted into Eq. C.28 we obtain

$$\begin{aligned} \delta Y_2 = \Bigg\{ & \left[-\frac{1}{E^2 I}\left(-\frac{1}{6} R_A {X_2}^3 + \frac{3}{2} F {L_1}^2 X_2 - F\, L L_1 X_2 - \frac{5}{6} F {L_1}^3 + \frac{1}{2} F\, L\, {L_1}^2 \right) \delta E \right]^2 + \\ & \left[-\frac{1}{EI^2}\left(-\frac{1}{6} R_A {X_2}^3 + \frac{3}{2} F {L_1}^2 X_2 - F\, L L_1 X_2 - \frac{5}{6} F {L_1}^3 + \frac{1}{2} F\, L\, {L_1}^2 \right) \delta I \right]^2 + \\ & \left[\frac{1}{EI}\left(-\frac{1}{6} {X_2}^3 \right) \delta R_A \right]^2 + \left[\frac{1}{EI}\left(-\frac{1}{2} R_A {X_2}^2 + \frac{3}{2} F {L_1}^2 - F\, L L_1 \right) \delta X_2 \right]^2 + \\ & \left[\frac{1}{EI}\left(3 F L_1 X_2 - F\, L X_2 - \frac{5}{2} F {L_1}^2 + F\, L\, L_1 \right) \delta L_1 \right]^2 + \\ & \left[\frac{1}{EI}\left(-F\, L_1 X_2 + \frac{1}{2} F\ {L_1}^2 \right) \delta L \right]^2 \Bigg\}^{\frac{1}{2}} \end{aligned} \quad . \tag{C.35}$$

Knowing the values of the dimensions of the cantilever, material properties, forces, and the uncertainties in all of these, the overall uncertainty can be found. The values used in this analysis are

$b = 20$	μm	$\delta b = 0.5$	μm
$h = 2.5$	μm	$\delta h = 0.125$	μm
$L = 200$	μm	$\delta L = 2$	μm
$L_o = 12$	μm	$\delta L_o = 2$	μm

$L_e = 150$ μm $\delta L_e = 2$ μm

$E = 160$ GPa $\delta E = 5$ GPa

$$L_1 = L_o + \frac{1}{2} L_e$$

$X_1 = 0, 1.13 \times 10^{-6} \ldots L - L_1$ μm $\delta X_1 = 0.25$ μm

$X_2 = L - L_1, 1.139 \times 10^{-4} \ldots L$ μm $\delta X_2 = 0.25$ μm

$F = 6.4412 \times 10^{-6}$ N

The overall uncertainty in the deformations of section-1 as a function of position along the microswitch is shown in Fig. C.1, while the percentage overall uncertainty in the deformations of section-1 as a function of the position along the microswitch computed using equation

$$\%\delta Y_1(X_1) = \left| \frac{\delta Y_1(X_1)}{Y_1(X_1)} \right| \cdot 100 \quad , \tag{C.36}$$

is shown in Fig. C.2.

The percent overall uncertainty in deformations of section-1 of the cantilever at $X_1 = L_1$ is over 15%. This value is not satisfactory for application purposes, thus the individual percent contributions to the overall uncertainty in deformations of section-1 of the cantilever were calculated according to equations

$$\%\delta Y_1 \delta E(X_1) = \frac{\left[-\frac{1}{E^2 I} \left(\frac{1}{6} F X_1^3 - \frac{1}{2} F L X_1^2 + \frac{1}{2} F L_1 X_1^2 - \frac{1}{6} R_A X_1^3 \right) \delta E \right]^2}{\left[\delta Y_1(X_1) \right]^2} 100 \quad , \tag{C.37}$$

$$\%\delta Y_1 \delta I(X_1) = \frac{\left[-\frac{1}{EI}\left(\frac{1}{6}FX_1{}^3 - \frac{1}{2}FLX_1{}^2 + \frac{1}{2}FL_1X_1{}^2 - \frac{1}{6}R_AX_1{}^3\right)\delta I\right]^2}{[\delta Y_1(X_1)]^2}100 \ , \quad \text{(C.38)}$$

$$\%\delta Y_1 \delta R_A(X_1) = \frac{\left[\frac{1}{EI}\left(-\frac{1}{6}X_1{}^3\right)\delta R_A\right]^2}{[\delta Y_1(X_1)]^2}100 \ , \quad \text{(C.39)}$$

$$\%\delta Y_1 \delta X_1(X_1) = \frac{\left[\frac{1}{EI}\left(\frac{1}{2}FX_1{}^2 - FLX_1 + FL_1X_1 - \frac{1}{2}R_AX_1{}^2\right)\delta X_1\right]^2}{[\delta Y_1(X_1)]^2} \ , \quad \text{(C.40)}$$

$$\%\delta Y_1 \delta L_1(X_1) = \frac{\left[\frac{1}{EI}\left(\frac{1}{2}FX_1{}^2\right)\delta L_1\right]^2}{[\delta Y_1(X_1)]^2}100 \ , \quad \text{(C.41)}$$

and

$$\%\delta Y_1 \delta L(X_1) = \frac{\left[\frac{1}{EI}\left(-\frac{1}{2}FX_1{}^2\right)\delta L\right]}{[\delta Y_1(X_1)]^2}100 \ . \quad \text{(C.42)}$$

In order to make sure that percentages determined using Eqs C.37 to C.42 are correct, they were added to give a combined value of all individual contributions equal to 100%, i.e.,

$$\begin{aligned}&\%\delta Y_1 \delta E\left(10\times10^{-6}\right) + \%\delta Y_1 \delta I\left(10\times10^{-6}\right) + \%\delta Y_1 \delta R_A\left(10\times10^{-6}\right) + \\ &\%\delta Y_1 \delta X_1\left(10\times10^{-6}\right) + \%\delta Y_1 \delta L_1\left(10\times10^{-6}\right) + \%\delta Y_1 \delta L\left(10\times10^{-6}\right) = 100\end{aligned} \ . \quad \text{(C.43)}$$

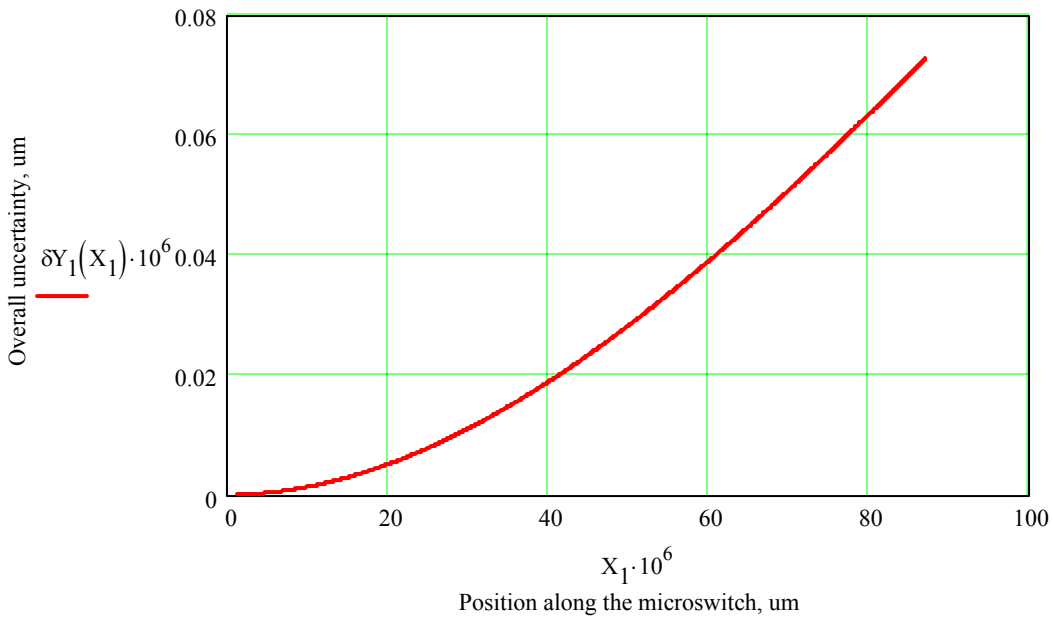

Fig. C.1. Overall uncertainty in deformations of section-1 of the cantilever as a function of position along the microswitch.

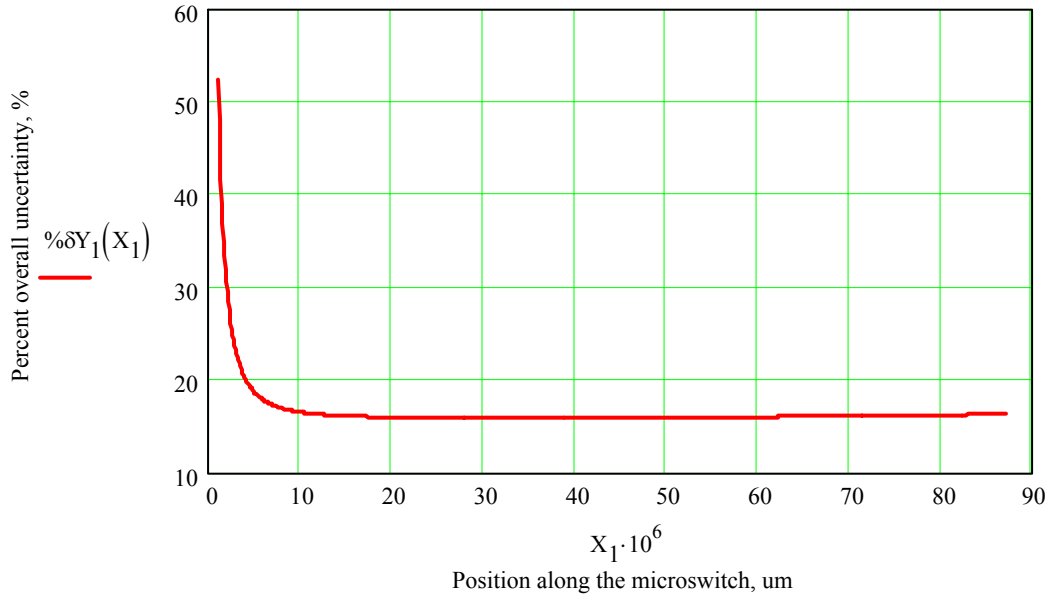

Fig. C.2. Percent overall uncertainty in deformations of section-1 of the cantilever as a function of position along the microswitch.

The percent contributions to overall uncertainty in deformations of section-1 of the cantilever as a function of position along the cantilever are shown in Figs C.3 and C.4.

For section-1 the greatest contributor to overall percent uncertainty in deformations at the end of the section is the uncertainty in the moment of inertia. What remains now is determination whether thickness or width contributes more. The individual contributions to the uncertainties in the moment of inertia were found using equations

$$\%\delta I\delta b = -\frac{\left(\frac{1}{12}h^3\delta b\right)^2}{(\delta I)^2}100 \quad , \tag{C.44}$$

$$\%\delta I\delta b = 2.703\ \% \quad , \tag{C.45}$$

$$\%\delta I\delta h = -\frac{\left(\frac{1}{4}bh^2\delta h\right)^2}{(\delta I)^2}100 \quad , \tag{C.46}$$

and

$$\%\delta I\delta h = 97.297\ \% \quad . \tag{C.47}$$

The results shown in Eqs C.44 to C.47 show that overall uncertainty is most affected by the uncertainty in thickness. In order to reduce the overall uncertainty in deformations, the uncertainty in thickness should be lowered. It can be controlled by more sophisticated fabrication processes.

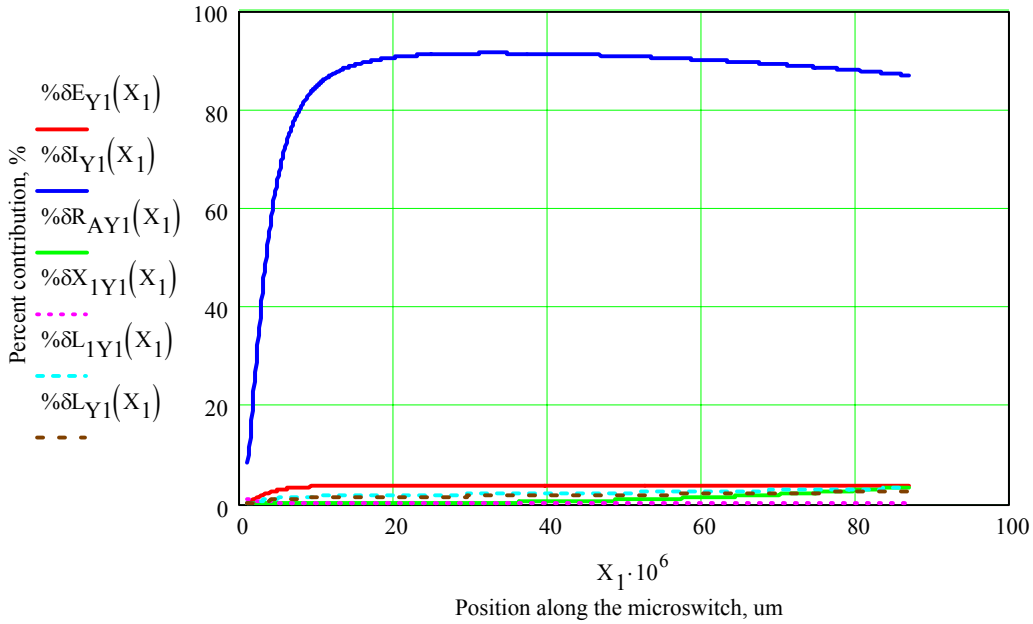

Fig. C.3. Percent contributions of individual uncertainties to overall uncertainty in deformations of section-1 of the cantilever as a function of position along the microswitch, lin-lin scale.

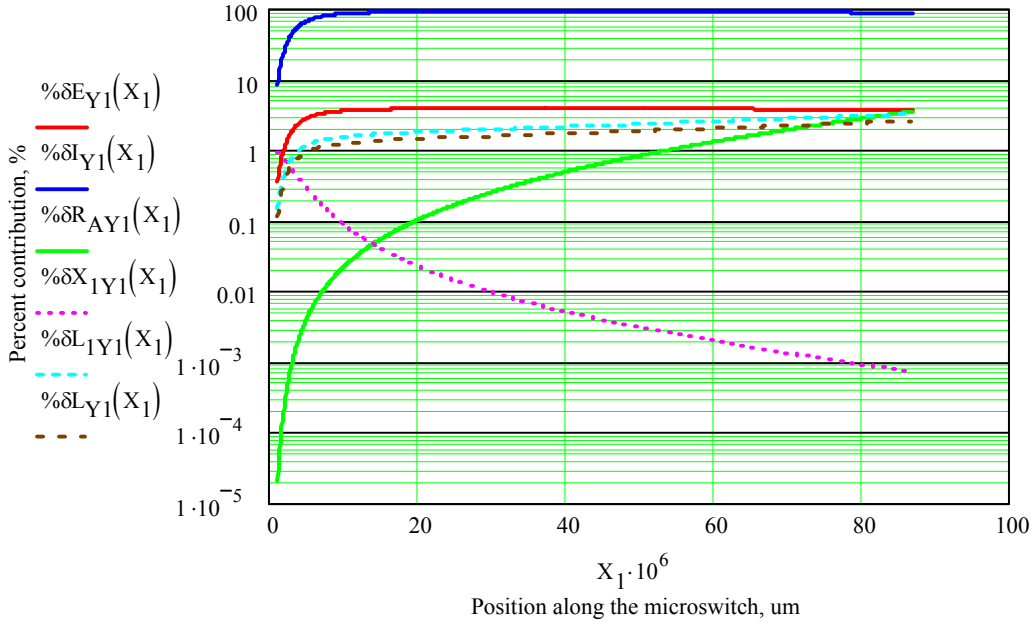

Fig. C.4. Percent contributions of individual uncertainties to overall uncertainty in deformations of section-1 of the cantilever as a function of position along the microswitch, lin-log scale.

The uncertainty in the deformations of section-2 as a function of position along the microswitch is shown in Fig. C.5, while percentage uncertainty in the deformations of section-2 as a function of the position along the microswitch using equation

$$\%Y_2(X_1) = \left|\frac{\delta Y_2(X_2)}{Y_2(X_2)}\right| \cdot 100 \quad , \tag{C.48}$$

is shown in Fig. C.6.

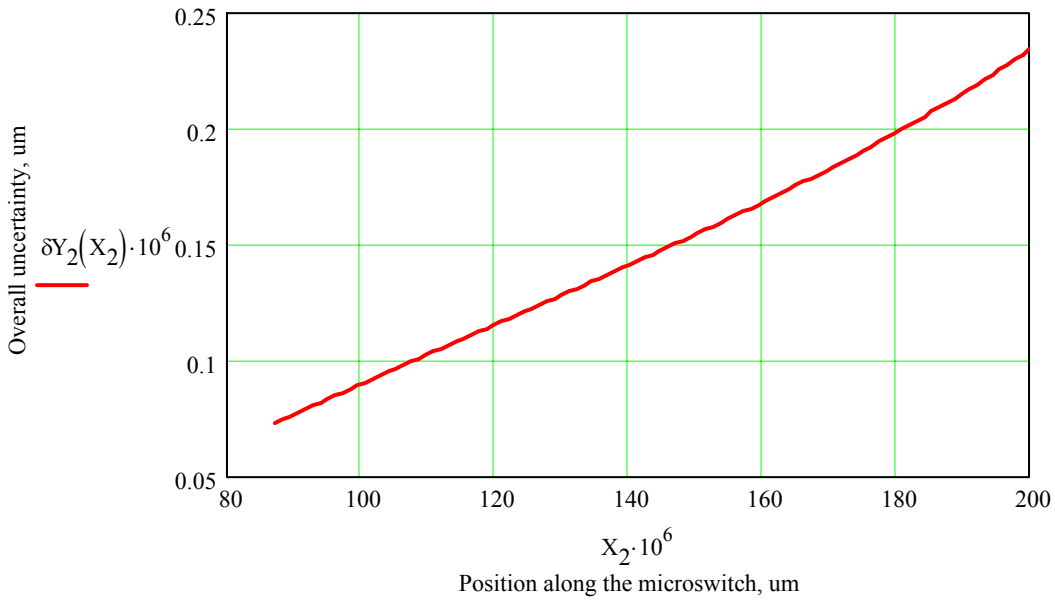

Fig. C.5. Overall uncertainty in deformations of section-2 of the cantilever as a function of position along the microswitch.

In order to find out which individual uncertainty had the greatest effect on the overall uncertainty in deformations of the section-2 of the cantilever, the individual contributions to the overall uncertainty were calculated according to equations

$$\%\delta Y_2\delta E(X_2)=\frac{\left\{\left[-\frac{1}{E^2I}\left(-\frac{1}{6}R_A{X_2}^3+\frac{3}{2}F{L_1}^2X_2-F\,LL_1X_2\right)\delta E\right]^2\right.}{\left[\delta Y_2(X_2)\right]^2}100+$$
$$\frac{\left[-\frac{1}{E^2I}\left(-\frac{5}{6}F{L_1}^3+\frac{1}{2}FL{L_1}^2\right)\delta E\right]^2}{\left[\delta Y_2(X_2)\right]^2}100 \quad , \text{(C.49)}$$

$$\%\delta Y_2\delta I(X_2)=\frac{\left[-\frac{1}{EI^2}\left(-\frac{1}{6}R_A{X_2}^3+\frac{3}{2}F{L_1}^2X_2-F\,LL_1X_2\right)\delta I\right]^2}{\left[\delta Y_2(X_2)\right]^2}100+$$
$$\frac{\left[-\frac{1}{E^2I}\left(-\frac{5}{6}F{L_1}^3+\frac{1}{2}FL{L_1}^2\right)\delta E\right]^2}{\left[\delta Y_2(X_2)\right]^2}100 \quad , \text{(C.50)}$$

$$\%\delta Y_2\delta R_A(X_2)=\frac{\left[\frac{1}{EI}\left(-\frac{1}{2}R_A{X_2}^2+\frac{3}{2}F{L_1}^2-F\,LL_1\right)\delta X_2\right]^2}{\left[\delta Y_2(X_2)\right]^2}100 \quad , \qquad \text{(C.51)}$$

$$\%\delta Y_2\delta X_2(X_2)=\frac{\left[\frac{1}{EI}\left(-\frac{1}{2}R_A{X_2}^2+\frac{3}{2}F{L_1}^2-F\,LL_1\right)\delta X_2\right]^2}{\left[\delta Y_2(X_2)\right]^2}100 \quad , \qquad \text{(C.52)}$$

$$\%\delta Y_2\delta L_1(X_2)=\frac{\left[\frac{1}{EI}\left(3FL_1X_2-F\,LX_2-\frac{5}{2}F{L_1}^2+F\,L\,L_1\right)\delta L_1\right]^2}{\left[\delta Y_2(X_2)\right]^2}100 \quad , \qquad \text{(C.53)}$$

and

$$\%\delta Y_2\delta L(X_2)=\frac{\left[\frac{1}{EI}\left(-F\,L_1X_2+\frac{1}{2}F\;{L_1}^2\right)\delta L\right]^2}{\left[\delta Y_2(X_2)\right]^2}100 \quad . \qquad \text{(C.54)}$$

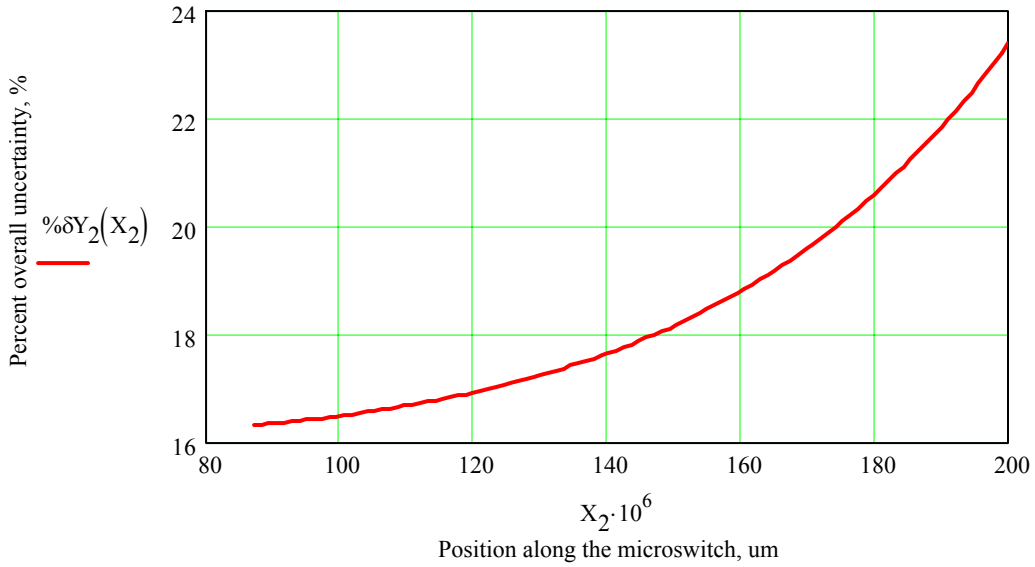

Fig. C.6. Percent overall uncertainty in deformations of section-2 of the cantilever as a function of position along the microswitch.

In order to make sure that percentages determined using Eqs C.49 to C.54 are correct, they are added to give a combined value of all individual contributions equal to 100%, i.e.,

$$\%\delta Y_2 \delta E\left(10\times10^{-6}\right)+\%\delta Y_2 \delta I\left(10\times10^{-6}\right)+\%\delta Y_2 \delta R_A\left(10\times10^{-6}\right)+ \\ \%\delta Y_2 \delta X_2\left(10\times10^{-6}\right)+\%\delta Y_2 \delta L_1\left(10\times10^{-6}\right)+\%\delta Y_2 \delta L\left(10\times10^{-6}\right)=100 \quad . \quad \text{(C.55)}$$

The percent contributions to overall uncertainty in deformations of section-2 of the cantilever as a function of position along the microswitch are shown in Figs C.7 and C.8.

For section-2 the greatest contributor to overall percent uncertainty in the maximum deformation is the uncertainty in the reaction force at the simply supported end of the cantilever. What remains now is determination whether L_1, L, E or I contributes

more. The individual contributions to the uncertainties in the reaction force were found using equations

$$\%\delta R_A \delta L_1 = \frac{\left[\left(24F\frac{L_1}{L^2} - 6F\frac{1}{L} - 15F\frac{{L_1}^2}{L^3}\right)\delta L_1\right]^2}{(\delta R_A)^2} 100 \quad , \tag{C.56}$$

$$\%\delta R_A \delta L_1 = 4.966\% \quad , \tag{C.57}$$

$$\%\delta R_A \delta L = \frac{\left[\left(-24F\frac{{L_1}^2}{L^3} + 6F\frac{L_1}{L^2} + 15F\frac{{L_1}^3}{L^4} - \frac{EI}{L^4}18\times10^{-6}\right)\delta L\right]^2}{(\delta R_A)^2} 100 \quad , \tag{C.58}$$

$$\%\delta R_A \delta L = 7.174\ \% \quad , \tag{C.59}$$

$$\%\delta R_A \delta E = \frac{\left[\left(6\times10^{-6}\frac{I}{L^3}\right)\delta E\right]^2}{(\delta R_A)^2} 100 \quad , \tag{C.60}$$

$$\%\delta R_A \delta E = 3.560\ \% \quad , \tag{C.61}$$

$$\%\delta R_A \delta I = \frac{\left[\left(6\times10^{-6}\frac{E}{L^3}\right)\delta I\right]^2}{(\delta R_A)^2} 100 \quad , \tag{C.62}$$

$$\%\delta R_A \delta I = 84.300\ \% \quad . \tag{C.63}$$

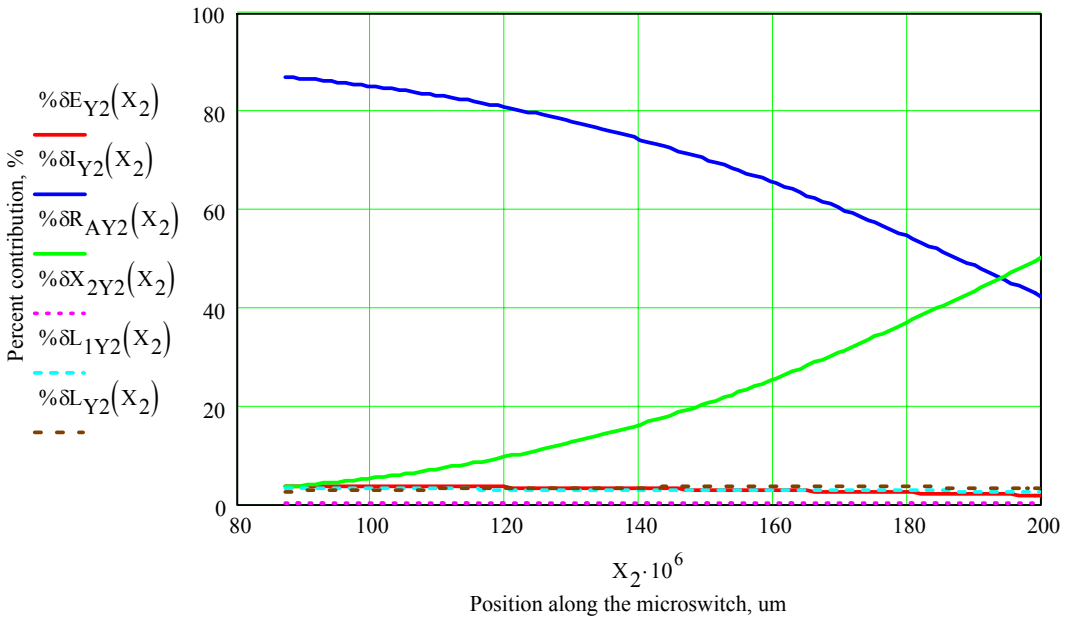

Fig. C.7. Percent contributions of individual uncertainties to overall uncertainty in deformations of section-2 of the cantilever as a function of position along the microswitch, lin-lin scale.

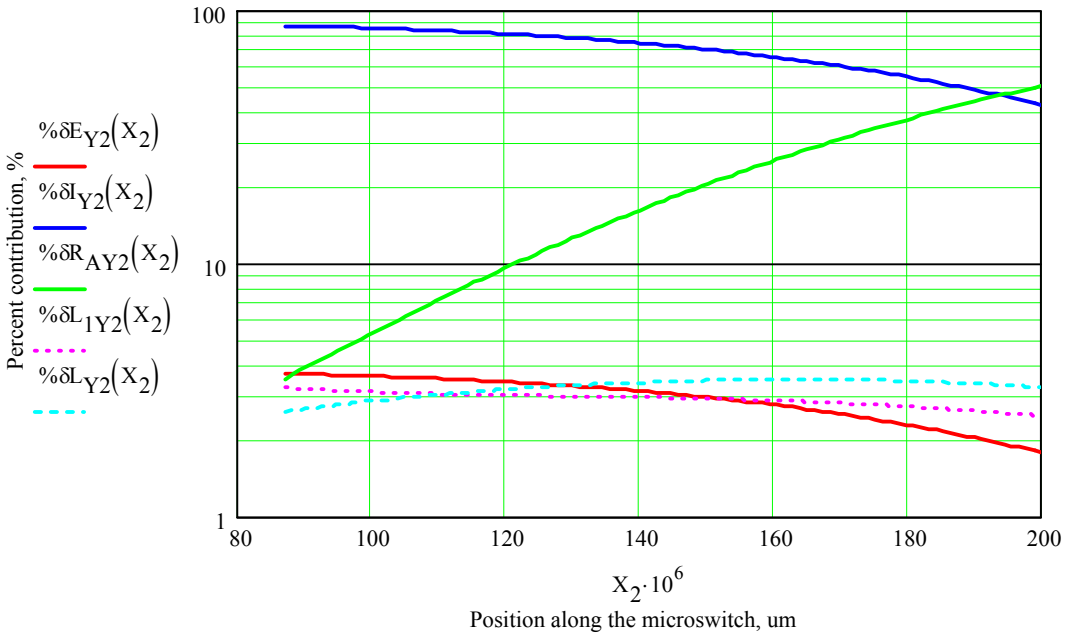

Fig. C.8. Percent contributions of individual uncertainties to overall uncertainty in deformations of section-2 of the cantilever as a function of position along the microswitch, lin-log scale

The results in Eqs C.56 to C.63 show that overall uncertainty in the reaction force is most affected by the uncertainty in thickness. As the uncertainty in thickness is reduced to one percent of its nominal value (0.025 μm) the overall uncertainty in the maximum deformation of the cantilever reduces from over 23% to nearly 11%. Even though the overall uncertainty in maximum deformation of the cantilever was cut in half, the uncertainty in thickness remains the greatest contributor to the overall uncertainty in the reaction force. The reduced value for the uncertainty in thickness is demanding and expensive to obtain when using currently available MEMS manufacturing processes. Although it can be further reduced because of advances in fabrication, it may be costly.

APPENDIX D. ANALYSIS OF RF CIRCUIT

Calculations involved in the analysis of the RF circuit, which the microswitch is included in, are based on the following set of parameters

shorting bar length:	$L_s = 26$	μm
shorting bar width:	$b_s = 6$	μm
shorting bar thickness:	$h_s = 1$	μm
contact gap distance:	$d_g = 1$	μm
contact overlap area:	$A_c = 36$	μm^2
air dielectric constant:	$\varepsilon_o = 8.85\ 10^{-6}$	$\frac{F}{\mu m}$
relative permittivity:	$\varepsilon_r = 1$	
operating frequency range:	$\omega = 0,\ 2\pi\frac{50\times10^9}{N} \ldots\ 2\pi\cdot 50\times10^9$	$\frac{rad}{sec}$

where N is equal to 100 and denotes a number of increments in the set range.

Operational frequency was assumed as a range of values from 0 GHz to 50 GHz. In order to analyze the circuit impedance of the RF circuit had to be calculated while the microswitch was in the open and closed positions. The impedance of an open microswitch in a series RF circuit configuration, shown in Fig. D.1, is calculated as

$$Z_{open} = \frac{2}{j\omega C_{imp}} + j\omega L_{imp} \quad , \tag{D.1}$$

where

$$C_{imp} = \frac{\varepsilon_o \varepsilon_r A_C}{d_g} \quad , \tag{D.2}$$

$$C_{imp} \times 10^{18} = 318.6 \text{ aF} \quad . \tag{D.3}$$

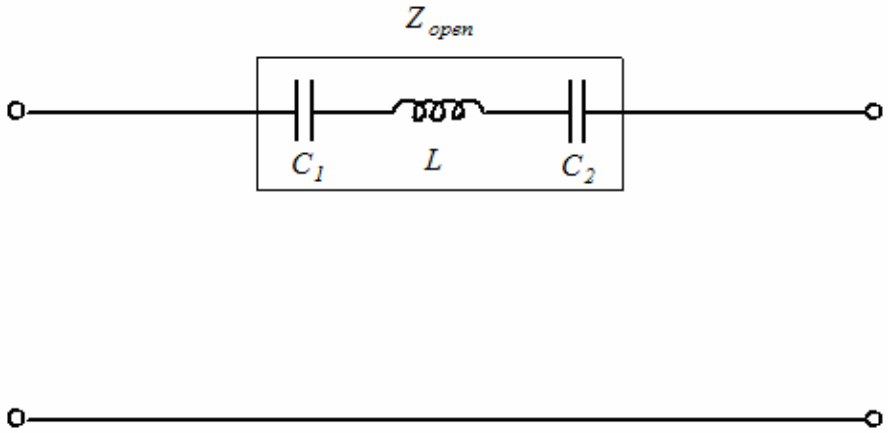

Fig. D.1. Circuit of the RF MEMS switch in open position.

A ratio of the thickness to width of the shorting bar was found as

$$w = \frac{h_s}{b_s} = 0.167 \quad . \tag{D.4}$$

Using the ratio defined in Eq. D.4, ln (w) value from Table 2.1 was found to be

$$\ln(w) = 0.00239 \quad . \tag{D.5}$$

The value given by Eq. D.5 is value is required to calculate inductance of the shorting bar using equation

$$L_{imp} = 0.2\ L_S \left[\ln\left(\frac{2L_S}{b_S + h_S} \right) + \frac{1}{2} - \ln(w) \right] \cdot 10^{-6} \quad , \tag{D.6}$$

$$L_{imp} \times 10^{12} = 13.015 \text{ pH} \quad . \tag{D.7}$$

Equation D.1 was then expressed as a function of the operational frequency, i.e.,

$$Z_{open}(\omega) = \left| \frac{2}{j\omega C_{imp}} + j\omega L_{imp} \right| \quad . \tag{D.8}$$

Graphical representation of the inductance of an open RF MEMS switch as a function of its operational frequency is given in Fig. D.2.

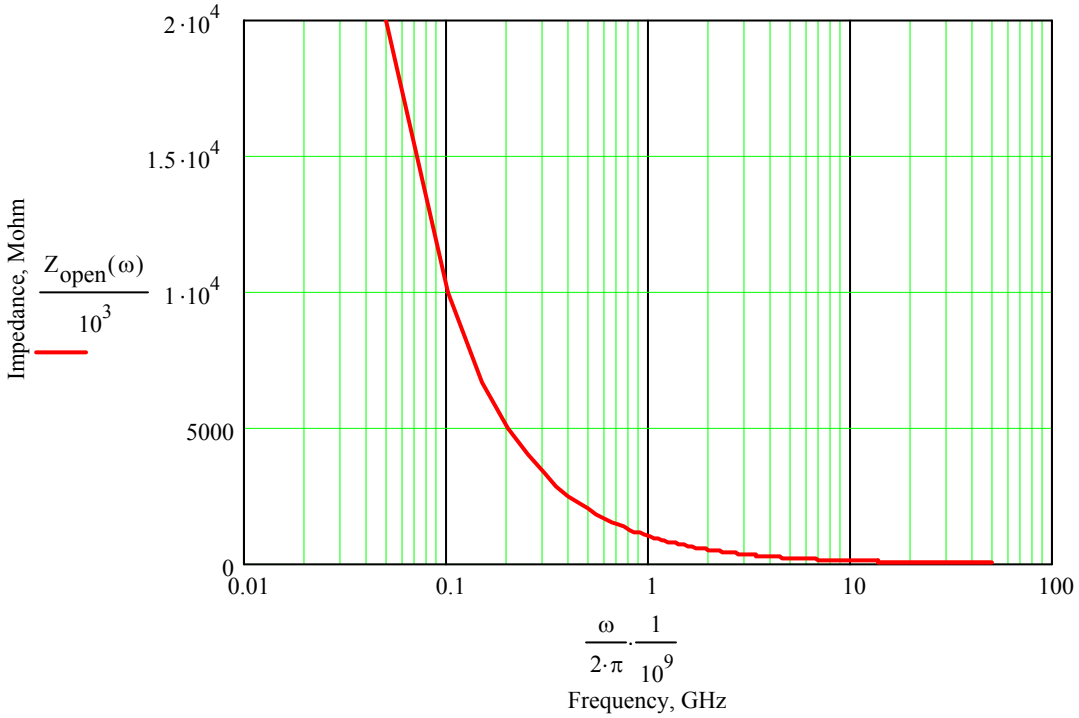

Fig. D.2. Impedance of the open microswitch as a function of its operational frequency.

For further analysis, impedance of a closed microswitch in an RF circuit, shown in Fig. D.3, was computed as

$$Z_{closed} = 2R_{imp} + j\omega L_{imp} \quad , \tag{D.9}$$

where the contact resistance was assumed to be 1 Ω per contact and the inductance of the

shorting bar remained as written in Eq. D.6.

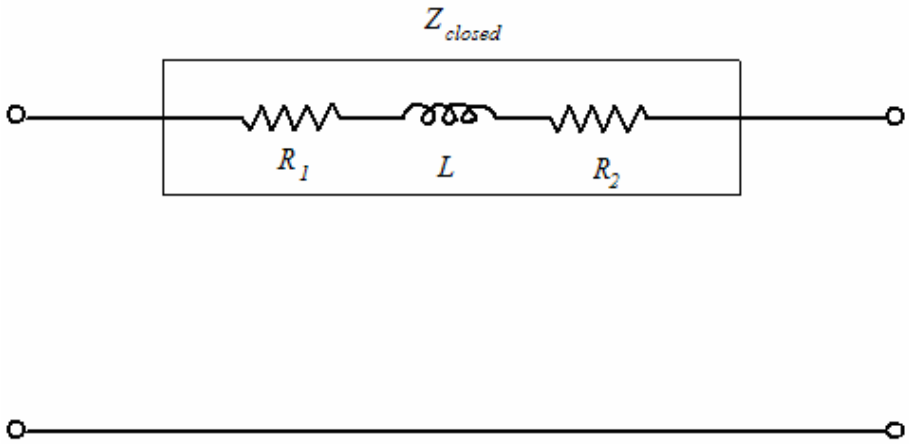

Fig. D.3. Circuit of the RF MEMS switch in closed position.

Equation D.9 was then expressed as a function of the operational frequency, i.e.,

$$Z_{closed}(\omega) = \left|2R_{imp} + j\omega L_{imp}\right| \quad . \tag{D.10}$$

Graphical representation of inductance of a closed RF MEMS switch as a function of its operational frequency is shown in Fig. D.4.

Based on the overall design of the circuit, shown in Fig. D.5, the S_{21} can be found. Based on information obtained from the Air Force MEMS Research Center an assumption is made that the impedance of the transition line on both sides of the microswitch is 50 Ω.

An equation expressing the S_{21} parameter of an open switch as a function of its operational frequency is written as

$$S_{21open}(\omega) = \frac{2Z_o}{2Z_o + Z_{open}(\omega)} \quad . \tag{D.11}$$

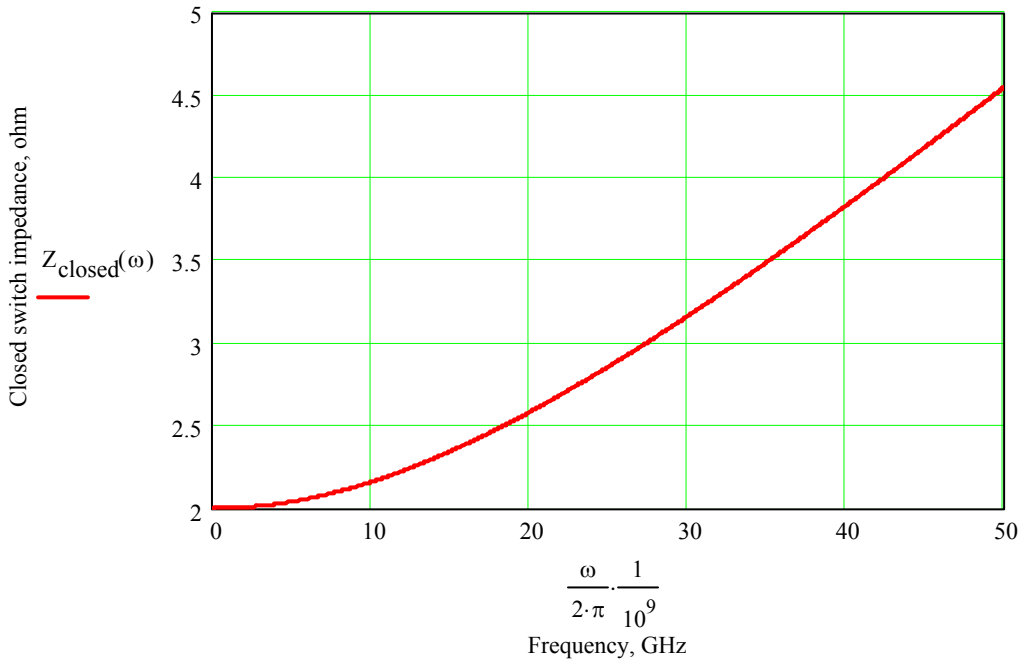

Fig. D.4. Impedance of closed microswitch as a function of its operational frequency.

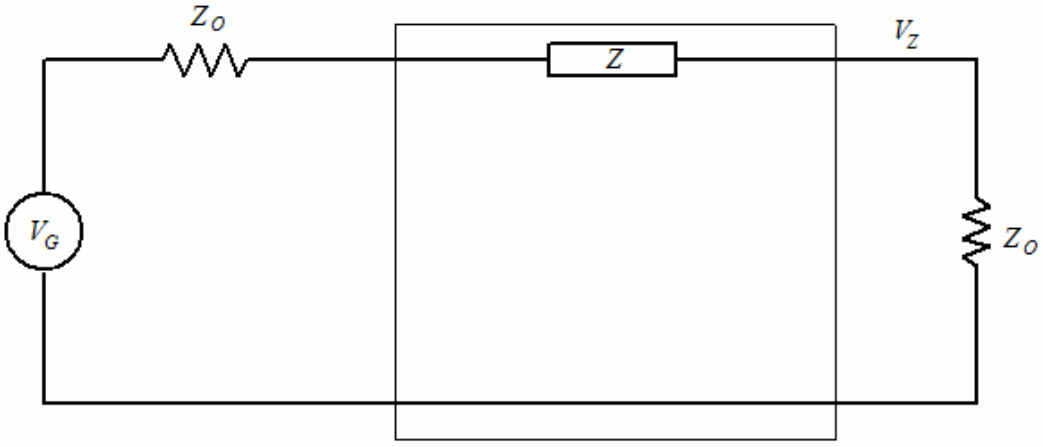

Fig. D.5. Schematic of the RF circuit impedance.

Also, equation expressing the S_{21} parameter of a closed switch as a function of its operational frequency is

$$S_{21closed}(\omega) = \frac{2Z_o}{2Z_o + Z_{closed}(\omega)} \quad . \tag{D.12}$$

The S_{21} parameter of an open switch translates into isolation of the circuit the switch is included in, while the S_{21} parameter of a closed switch translates into insertion loss of that circuit. For a better understanding of the isolation and insertion loss results, the S_{21} parameters are expressed in decibels.

The isolation as a function of the operational frequency expressed in decibels can be written as

$$S_{21OPEN}(\omega) = 20\log[S_{21_{open}}(\omega)] \quad , \tag{D.13}$$

while the insertion loss as a function of the operational frequency, expressed in decibels, is

$$S_{21CLOSED}(\omega) = 20\log[\, S_{21closed}(\omega)] \quad . \tag{D.14}$$

The isolation and insertion loss in decibels, as a functions of frequency, are shown in Figs D.6 and D.7, respectively.

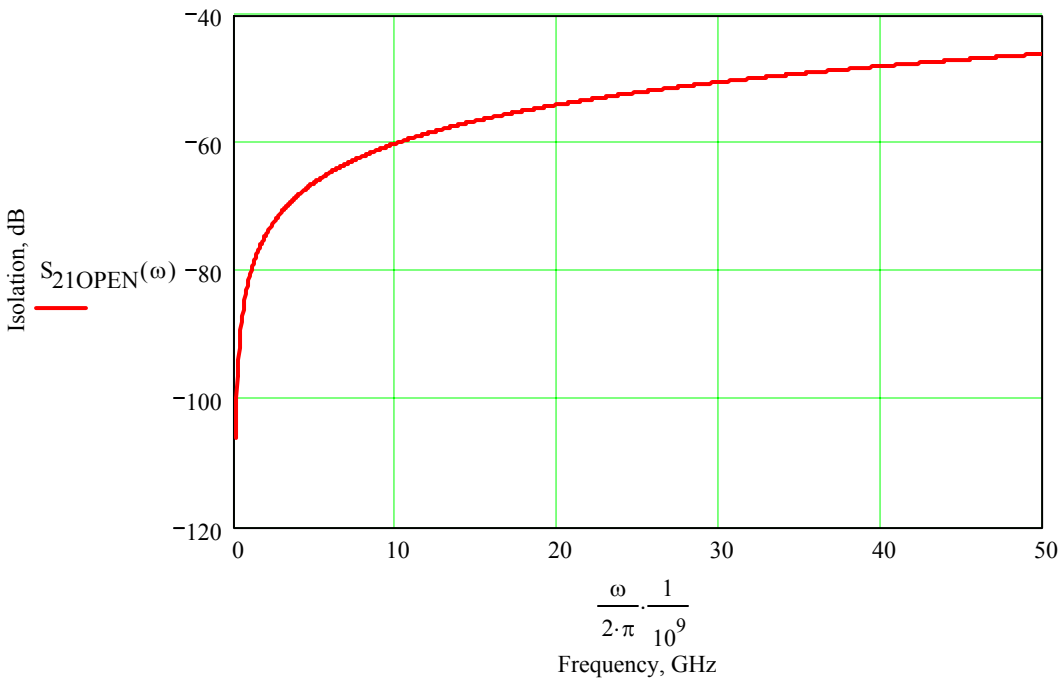

Fig. D.6. Microswitch isolation in decibels as a function of frequency.

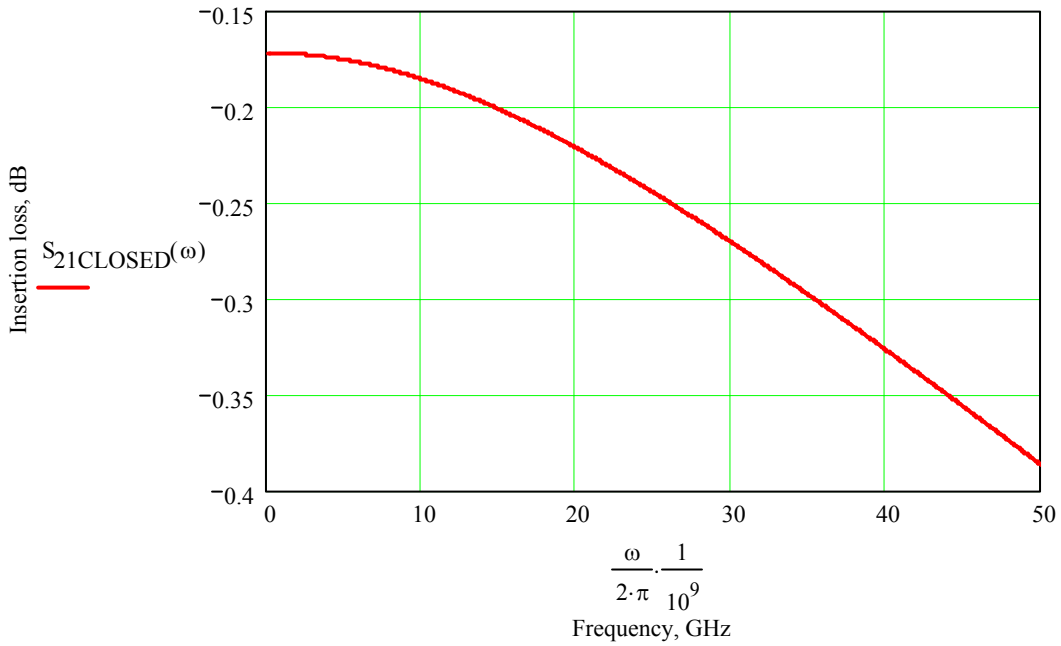

Fig. D.7. Microswitch insertion loss in decibels as a function of frequency.